



저작자표시-비영리-변경금지 2.0 대한민국

이용자는 아래의 조건을 따르는 경우에 한하여 자유롭게

- 이 저작물을 복제, 배포, 전송, 전시, 공연 및 방송할 수 있습니다.

다음과 같은 조건을 따라야 합니다:



저작자표시. 귀하는 원저작자를 표시하여야 합니다.



비영리. 귀하는 이 저작물을 영리 목적으로 이용할 수 없습니다.



변경금지. 귀하는 이 저작물을 개작, 변형 또는 가공할 수 없습니다.

- 귀하는, 이 저작물의 재이용이나 배포의 경우, 이 저작물에 적용된 이용허락조건을 명확하게 나타내어야 합니다.
- 저작권자로부터 별도의 허가를 받으면 이러한 조건들은 적용되지 않습니다.

저작권법에 따른 이용자의 권리는 위의 내용에 의하여 영향을 받지 않습니다.

이것은 [이용허락규약\(Legal Code\)](#)을 이해하기 쉽게 요약한 것입니다.

[Disclaimer](#)

Ph.D. DISSERTATION

**Resistive Switching Memory Devices
based on 2D and Quasi-2D Halide
Perovskites**

By

Hyojung Kim

December 2020

**DEPARTMENT OF MATERIALS SCIENCE AND
ENGINEERING**

COLLEGE OF ENGINEERING

SEOUL NATIONAL UNIVERSITY

Resistive Switching Memory devices based on 2D and Quasi-2D Halide Perovskites

Advisor: Prof. Ho Won Jang

by

Hyojung Kim

A thesis submitted to the Graduate Faculty of Seoul National University
in partial fulfillment of the requirements
for the Degree of Doctor of Philosophy
Department of Materials Science and Engineering

December 2020

Approved

by

Chairman of Advisory Committee: Jin Young Kim

Vice-Advisory Committee: Ho Won Jang

Advisory Committee: Jeong-Yun Sun

Advisory Committee: Soo Young Kim

Advisory Committee: Jung Kyu Kim

Handwritten signatures of the advisory committee members: Jin Young Kim, Ho Won Jang, Jeong-Yun Sun, Soo Young Kim, and Jung Kyu Kim.

Abstract

The ReRAM device is being spotlighted as a next-generation alternative to conventional memory devices. Although extensive studies on switching materials have been reported, ReRAM devices based on halide perovskites have not been reported much because they have only recently emerged as viable materials. Metal oxide-based resistive switching memories show disadvantages such as low mechanical flexibility, high-temperature process, and hard bonding between metal and oxide. Thus, the active materials for resistive switching memory are needed to investigate.

Currently, many groups have started to research halide-perovskite-based ReRAM devices owing to their potential. Halide perovskites based resistive random-access memory (ReRAM) can be a new data storage device because of their high ON/OFF ratio, low operating voltage, and excellent mechanical properties.

In the thesis, the characterization of electrical properties of halide perovskites and the operating mechanism of resistive switching memories are described in detail in two parts. Moreover, three research topics are introduced for enhancement resistive switching performance, such as high ON/OFF ratios, long-endurance, and long retention time enhancement are described in detail.

In the first chapter, the backgrounds of halide perovskites are introduced.

In general, halide perovskites are a family of compounds with the chemical formula ABX_3 , where a monovalent A^+ cation, a divalent B^{2+} cation, and the 1^- charge of the X halide anion are positioned in a unit cell corresponding to a corner-sharing octahedral network. In terms of geometric structures, to satisfy the ideal cubic halide perovskite unit, the tolerance factor (t) developed by Goldschmidt has to be met first, $0.85 < t < 1.11$. The t is described by $(r_A + r_X) / \sqrt{2}(r_B + r_X)$, where r_A , r_B , and r_X are the ionic radius of A, B, or X atoms, respectively. When the BX_6 octahedron tilts, that leads to a lower-symmetry tetragonal or orthorhombic crystal structure.

In terms of electronic properties, halide perovskites have tunable blends and colors are unique properties, which allow them to work in a broad visible spectral range, which can be extended to near-infrared. Also, the carrier diffusion length of $MAPbI_3$ is a few hundred nm, and it can be extended up to 1 μm using a mixed halide, according to transient photoluminescence measurements. Thus, there are extensive applications of halide perovskites owing to their exceptional attributes in different areas, such as light-emitting diodes, lasers, X-ray detectors, memory devices, and more.

Still, several key challenges of halide perovskites are highlighted, such as toxicity of lead or instability.; these challenges need to be addressed to realize the commercial potential of these unique materials fully.

In the second chapter, the operating mechanism within ReRAM devices are explained.

Generally, ReRAM is a metal-insulator-metal stack, which is a two-terminal device. Following the electroforming process, when the opposite threshold voltage is applied, the low resistance state is switched to the high-resistance state at the particular voltage (RESET process). Then, the "SET process," which refers to the switching from an HRS to an LRS, occurs at opposite bias. In the resistive switching operation, the SET changes to the RESET process indicate an "ON" state, and the opposite behavior indicates an "OFF" state.

The switching mechanism can be classified as a filamentary-type and interface-type depending on the conducting path. The difference between filamentary and interface resistive switching depends on the area. In the filamentary switching, the current conduction is narrowly confined to a narrow part of the device area. In contrast, in interface switching, the resistance change occurs by field-induced modification over the entire electrode area.

Here, as the structure of composition, halide perovskites based ReRAM devices are classified; 1) organic-inorganic hybrid, 2) all inorganic, 3) layered structure, and 4) lead-free and new composition halide-perovskite-based ReRAMs in this part.

In the third chapter, quasi-2D halide perovskites $(\text{PEA})_2\text{Cs}_3\text{Pb}_4\text{I}_{13}$ based memory device is introduced.

Three-dimensional (3D) halide perovskites are the most investigated materials for resistive switching memory devices. However, 3D-based memory devices display comparable ON/OFF ratios to oxide or chalcogenide ReRAM devices. Additionally, the perovskite materials are susceptible to exposure to air. Herein, we compare the resistive switching characteristics of ReRAM devices based on a quasi-two-dimensional (2D) halide perovskite, $(\text{PEA})_2\text{Cs}_3\text{Pb}_4\text{I}_{13}$, to those based on 3D CsPbI_3 . Astonishingly, the ON/OFF ratio of the $(\text{PEA})_2\text{Cs}_3\text{Pb}_4\text{I}_{13}$ -based memory devices (10^9) was three orders higher than that of the CsPbI_3 device, which is attributed to a decrease in the high resistance state (HRS) current of the former. This device also retained a high ON/OFF current ratio for two weeks under ambient conditions, whereas the CsPbI_3 device degraded rapidly and showed unreliable memory properties after five days. These results strongly suggest that quasi-2D halide perovskites have potential in resistive switching memory based on their desirable ON/OFF ratio and long-term stability.

In the fourth chapter, 2D/3D perovskite heterojunction films are introduced to be applied to resistive switching memory devices.

Halide perovskites have garnered significant attention for resistive switching memory devices due to their low cost, low operation voltage, and excellent mechanical properties. However, the halide perovskite-based memory devices face several challenges due to short endurance and stability. Thus, 2D/3D perovskite heterojunction films are introduced, and their resistive switching behavior was

investigated. The 2D/3D perovskite resistive switching devices exhibited excellent performance with an endurance of 2700 cycles, a high ON/OFF ratio of 10^6 , and an operating speed of 640 μs . The calculated thermally-assisted ion-hopping activation energy and the results of the time-of-flight secondary ion mass spectroscopy demonstrated that the 2D perovskite layer could efficiently prevent the Ag ion migration into the 3D perovskite film.

Moreover, due to its high thermal conductivity, 2D perovskite can control the Ag conductive filament rupture. Thus, the 2D perovskite layer enhances endurance by controlling both Ag migration and filament rupture. Hence, this study provides an alternate strategy for improving the endurance of halide perovskite-based resistive switching memory devices.

In the fifth chapter, TPBI on the MAPbBr_3 switching layer is introduced.

To improve the device's reliability, TPBI was inserted on the MAPbBr_3 switching layer as an electron transfer material for the first time. In the MAPbBr_3 perovskite switching layer, the formation and rupture of Ag filaments occur via reduction-oxidation reaction. The TPBI plays a role in filaments control during the SET and RESET process. Therefore, the MAPbBr_3 device with TPBI applied was functional for 300 endurance cycles under continuous voltage pulses, maintained ON/OFF ratios above 10^7 , whereas only 90 endurance cycles were seen in the original MAPbBr_3 device without TPBI. These results strongly suggest that electron transfer

materials have potential in halide perovskite memory devices based on their desirable reliability and stability.

Although formal research on halide-perovskite-based ReRAM devices has only just started, it will be a highly influential device with tremendous advances in the future market and serve as a stepping stone for developing a resistive switching memory field. The thesis will encourage researchers to investigate halide-perovskite-based ReRAM devices with useful insights, overcome its challenges, and give a direction to offer promising opportunities.

Keywords: Halide perovskites, Resistive switching memory devices, Solution process, 3D halide perovskites, quasi-2D halide perovskites, 3D/2D heterojunction, Resistive switching mechanism, TPBI

Student Number: 2017-36719

Hyojung Kim

Table of Contents

Abstract	i
Table of Contents	vii
List of Tables	ix
List of Figures	x
Chapter 1	1
Halide Perovskite Materials: Crystal structures, Electrical properties and Synthesis	1
1. 1. Introduction	2
1. 2. Crystal structures and properties	5
1. 3. Synthesis	20
1. 4. Challenges	25
1. 5. Conclusions	27
1. 6. Reference	28
Chapter 2	34
The Operational Mechanisms of Resistive Switching Memories based Halide perovskites	34
2. 1. Introduction	35
2. 2. Principles of ReRAM devices	37
2. 3. Switching memory device based on halide perovskites	44
2. 4. Conclusion	57
2. 5. Reference	58
Chapter 3	65
Resistive Switching Devices based on Quasi-2D Halide Perovskites for High ON/OFF Ratios	65
3. 1. Introduction	66
3. 2. Experimental Section	69

3. 3. Results and Discussion	71
3. 4. Conclusion	94
3. 5. Reference	95
Chapter 4	103
Tailored 2D/3D Halide Perovskite Heterointerface for Substantially Enhanced Endurance	103
4. 1. Introduction	104
4. 2. Experimental Section	107
4. 3. Results and Discussion	109
4. 4. Conclusion	133
4. 5. Reference	134
Chapter 5	142
MAPbBr₃ Halide Perovskite based Resistive Switching Devices using Electron Transport Layer for Long Endurance Cycles and Retention Times	142
5. 1. Introduction	143
5.2. Experimental section	146
5. 3. Results and Discussion	148
5. 4. Conclusion	167
5. 5. Reference	168
Chapter 6	176
Summary	176
List of Publications	182
List of Patents	186
List of Presentations	187
List of Awards	189
Abstract (in Korean)	190

List of Tables

Table 3. 1. Comparison of various halide perovskites -based ReRAM devices.	79
Table 4. 1. Physical input parameters used for the COMSOL simulation.....	132

List of Figures

Figure 1. 1. Perovskite devices beyond photovoltaics: LEDs, lasers, memories, transistors, X-ray detectors, Li-ion batteries, piezoelectric energy generators, and gas sensors. Reproduced with permission. Copyright 2015, American Association for the Advancement of Science,⁸ 2017, John Wiley and Sons,⁶⁰ 2015, Nature Publishing Group,^{9,10} 2011, Elsevier,⁴⁸ 2016, John Wiley and Sons,¹¹ 2012, Nature Publishing Group,³³ 2015, Royal Society of Chemistry.³⁴4

Figure 1. 2. General perovskite structure. (a) Crystal structure of ABX_3 halide perovskite, where A cations are denoted by pink spheres, B cations are denoted by green spheres, and X (halide) anions are denoted by purple spheres. (b) An alternative view of the ABX_3 halide perovskite structure. The crystal structure is equivalent with the Figure on the left. (c) An extended network of ABX_3 halide perovskite linked by corner-shared octahedrons.....5

Figure 1. 3. (a) 2352 tolerance factors can be calculated, of which 742 lie in the $0.8 < \text{tolerance factor} < 1$ range. (b) Tolerance factors of Pb iodides and Mn formates plotted against cation size. The light blue area indicates the range of the perovskite structure expected. (c) Tolerance factors of lead and tin halide perovskites. Reproduced under the Creative Commons Attribution 4.0 International License and reproduced with permission copyright 2014, 2015 and 2016 Royal Society of Chemistry.^{5,12,13}6

Figure 1. 4. Layered structure of crystalline perovskites with increasing dimensionality (n) from the left to right ($n = 1$ for 2D and $n = \infty$ for 3D, where $n = 1, 2, 3, \dots, \infty$).....8

Figure 1. 5. (a) Absorption spectra of $MAPb_{1-x}Sn_xI_3$ perovskites. (b) Energy band diagram of widely tunable halide perovskite materials. Reproduced with permission. Copyright 2016, ACS publications.⁶.....13

Figure 1. 6. (a) One-step and two-step spin-coating procedures for solution process. (b) Thermal evaporation system for sensitively controlling the pressure in a vacuum chamber. Reproduced with permission. Copyright 2015, Elsevier⁴ and 2016, Royal Society of Chemistry.⁵21

Figure 2. 1. (a) The operating mechanism of the resistive switching behaviour; electroforming process, filament formation, and rupture in switching layer. (b) The filamentary-type switching mechanism and (c) interface-type switching mechanism.38

Figure 2. 2. (a) The organic-inorganic halide perovskite structure (a unit cell of MAPbI₃). (b) The five initial *I–V* sweeps of a Ag/MAPbI₃/Pt cell. Reproduced with permission.⁴⁷ Copyright 2016, John Wiley and Sons.47

Figure 2. 3. (a) The five initial series voltage sweeps of a Ag/PMMA/CsPbI₃/Pt device. The phase transition from cubic phase (perovskite) (b) to the orthorhombic phase (non-perovskite) (c). Reproduced with permission.⁵⁵ Copyright 2017, John Wiley and Sons. (d) Schematic drawings of the CsPbBr₃ QD-based ReRAM device fabrication process via all-solution process. (e) Endurance results under light illumination and dark condition. Reproduced with permission.⁵⁶ Copyright 2018, John Wiley and Sons49

Figure 2. 4. (a) The comparison of the crystal structure of 2D (BA₂PbI₄) and 3D MAPbI₃. *I–V* characteristics of BA₂PbI₄ (b), BA₂MAPb₂I₇ (c), BA₂MA₂Pb₃I₁₀, (d) and MAPbI₃ (e). Reproduced with permission.⁵⁷ Copyright 2017, Royal society of Chemistry52

Figure 2. 5. (a) Schematic drawings of the (CH₃NH₃)₃Bi₂I₉ based ReRAM device. The inset shows the (CH₃NH₃)₃Bi₂I₉ halide perovskite structure in a unit cell. (b) The *I–V* sweeps of Au/MABI/ITO device. Reproduced with permission.⁶⁰ Copyright 2018, Royal society of Chemistry54

Figure 3. 1. Schematic illustration of resistive memory device structure and resistive switching materials, CsPbI₃ and (PEA)₂Cs₃Pb₄I₁₃72

Figure 3. 2. Properties of halide perovskite films. (a, b) Top-view SEM images of the CsPbI₃ (a) and (PEA)₂Cs₃Pb₄I₁₃ (b) perovskite film. (c, d) AFM images of the CsPbI₃ (c) (RMS = 15.0 nm) and the (PEA)₂Cs₃Pb₄I₁₃ (d) perovskite film (RMS = 15.0 nm). The tips move 5 μm through the red and blue line to measure the roughness. (e) X-ray diffraction pattern of CsPbI₃ and (PEA)₂Cs₃Pb₄I₁₃ thin films on glass substrate74

Figure 3. 3. Typical current–voltage curves of Ag/CsPbI₃/Pt (a) and Ag/(PEA)₂Cs₃Pb₄I₁₃/Pt (b) devices. Temperature-dependent OFF currents of Ag/CsPbI₃/Pt (c) and Ag/(PEA)₂Cs₃Pb₄I₁₃/Pt (d) devices; Arrhenius equation was used to deduce *E_a*. (e) Comparison of the ON/OFF ratio with various halide perovskites-based ReRAM devices including the CsPbI₃ and ((PEA)₂Cs₃Pb₄I₁₃ based cells.....76

Figure 3. 4. Resistive switching performance of (PEA)₂Cs₃Pb₄I₁₃-based memory device. (a) Series *I–V* characteristics of the Ag/(PEA)₂Cs₃Pb₄I₁₃/Pt cells. (b, c) Statistically analyzed forming (b), SET, and RESET (c) voltage distributions of 50 different Ag/(PEA)₂Cs₃Pb₄I₁₃/Pt cells. (d) High- and low-resistance states of 50 different Ag/(PEA)₂Cs₃Pb₄I₁₃/Pt cells. (e) Endurance

characteristics for (PEA) ₂ Cs ₃ Pb ₄ I ₁₃ memory device. (f) Retention property of the ON and OFF states	82
Figure 3. 5. Current transport mechanisms underlying resistive switching behavior. (a) Double-logarithmic scale of I - V curve of the Ag/(PEA) ₂ Cs ₃ Pb ₄ I ₁₃ /Pt device. (b) Proportional relation of current density to voltage ($I \propto V$) for LRS. (c) Relation of current to square root of voltage ($\ln I \propto V^{1/2}$) for HRS	85
Figure 3. 6. Comparison of linear replotted I - V curves for HRS of CsPbI ₃ and (PEA) ₂ Cs ₃ Pb ₄ I ₁₃ devices. (b) Schematic diagram of Schottky barrier heights for CsPbI ₃ and (PEA) ₂ Cs ₃ Pb ₄ I ₁₃	88
Figure 3. 7. (a) Temperature-dependence of HRS before SET process. (b, c, d) Tendency of forming (b), SET (c), and RESET (d) voltages under DC voltage sweep with increasing temperature.....	90
Figure 3. 8. Stability tests from I - V measurements of Ag/CsPbI ₃ /Pt (a) and Ag/(PEA) ₂ Cs ₃ Pb ₄ I ₁₃ /Pt (b) devices	92
Figure 4. 1. (a) GIXRD patterns of the 2D/3D perovskite film at X-ray incident angles of 0.3°, 2°, 5°, and 8° (the filled triangles and squares denote the diffraction peaks corresponding to the 2D and 3D perovskite, respectively). The morphologies of the 3D perovskite and 2D/3D perovskite film; plane view scanning electron microscopy (SEM) images of: (b) 3D perovskite and (c) 2D/3D perovskite film. Cross-sectional SEM images of: (d) 3D perovskite and (e) 2D/3D perovskite film. Comparison of the crystalline structure of: (f) 3D perovskite and (g) 2D/3D perovskite film	109
Figure 4. 2. XRD patterns of the 2D/3D perovskite films fabricated using different concentrations of PEAI solution	110
Figure 4. 3. Plane view scanning electron microscopy (SEM) images of: (a) pristine 3D perovskite, (b) 10 mg PEAI, (c) 20 mg PEAI, and (d) 30 mg PEAI.	111
Figure 4. 4. (a) Typical current-voltage (I - V) characteristics of halide perovskite-based resistive switching devices. (2D/3D- PEAI 20 mg) (b) Resistive switching behavior measured with the DC pulses. Pulse duration is fixed at 640 μ s	113
Figure 4. 5. (a) Typical current-voltage (I - V) characteristics of halide perovskite-based resistive switching devices. (a) PEAI 10 mg (b) PEAI 30 mg	114
Figure 4. 6. Typical I - V characteristics of 2D halide perovskite-based resistive switching devices.	115
Figure 4. 7. Average of set and reset voltage. (a) 3D perovskite and (b) 2D/3D perovskite	117

Figure 4. 8. *I–V* characteristics exhibiting the potential for multilevel switching (a) *I–V* characteristics of 3D perovskite and (b) *I–V* characteristics of 2D/3D perovskite (compliance current = 10^{-3} , 10^{-4} , 10^{-5} , and 10^{-6} A).118

Figure 4. 9. Resistive switching behavior measured with the DC pulses. Pulse duration is fixed at 640 μ s. (a) PEAI 10 mg (b) PEAI 30 mg120

Figure 4. 10. 2D perovskite based resistive switching behavior measured with the DC pulses. Pulse duration is fixed at 640 μ s.121

Figure 4. 11. Retention characteristics of the halide perovskite-based resistive switching devices: (a) 3D perovskite and (b) 2D/3D perovskite. 122

Figure 4. 12. Long-term stability of the halide perovskite-based resistive switching devices: (a,b) $\text{PbI}_2/\text{MAPbI}_3$ peak ratio of halide perovskite -based resistive switching devices. (c,d) Reset voltage deviation of halide perovskite-based resistive switching devices. (e,f) Set voltage deviation of halide perovskite-based resistive switching devices. (a,c,e) 3D perovskite and (b,d,f) 2D/3D perovskite.....123

Figure 4. 13. XRD patterns of the halide perovskite-based resistive switching devices as a function of time: (a) 3D perovskite and (b) 2D/3D perovskite124

Figure 4. 14. *I–V* characteristics of halide perovskite-based resistive switching devices for long-term stability: (a) 0 days 3D perovskite, (b) 0 days 2D/3D perovskite, (c) 7 days 3D perovskite, (d) 7 days 2D/3D perovskite, (e) 14 days 3D perovskite, (f) 14 days 2D/3D perovskite, (g) 21 days 3D perovskite, (h) 21 days 2D/3D perovskite, (i) 28 days 3D perovskite, and (j) 28 days 2D/3D perovskite.125

Figure 4. 15. Conduction mechanism of halide perovskite -based resistive switching devices: (a,b) Logarithmic *I–V* characteristics of: (a) 3D perovskite and (b) 2D/3D perovskite films. (c) Thermally-assisted ion-hopping (*TAH*) activation energy is calculated at various temperatures128

Figure 4. 16. (a,c) Schematic of halide perovskite -based resistive switching devices with: (a) 3D perovskite (c) 2D/3D perovskite. (b,d) ToF-SIMS 3D image results for halide perovskite-based resistive switching devices under different endurance cycles. Each 3D image is $50 \times 50 \times 0.5 \mu\text{m}$. (b) 3D perovskite (d) 2D/3D perovskite.129

Figure 4. 17. (a) Thermal conductivity of 3D perovskite and 2D perovskite films. (b) COMSOL simulation result for the 2D/3D perovskite film.131

Figure 5. 1. Schematic illustration of the resistive memory device structure and resistive switching materials MAPbBr_3 (a). Synthesis processes of MAPbBr_3 by chloroform (b) and MAPbBr_3 by TPBI dissolved in chloroform (c).....148

Figure 5. 2. Planar-view SEM images of the MAPbBr ₃ :CF (a) and MAPbBr ₃ :TPBI(b). Cross-sectional SEM images of the MAPbBr ₃ :CF (c) and MAPbBr ₃ :TPBI(d).	150
Figure 5. 3. Grain size distribution of MAPbBr ₃ :CF (a) and MAPbBr ₃ :TPBI (b) films.....	151
Figure 5. 4. XRD pattern in the 2θ range of 10-60° of MAPbBr ₃ :CF (a) and MAPbBr ₃ :TPBI (b) films.	152
Figure 5. 5. XPS spectra to exhibit core level peaks of the elemental compositions (a) and their normalized data (b).....	153
Figure 5. 6. TOF-SIMS measurement of the MAPbBr ₃ :CF (a) and MAPbBr ₃ :TPBI (b) film. (c) Comparison of the TPBI distribution profiles in MAPbBr ₃ :CF and MAPbBr ₃ :TPBI film.....	155
Figure 5. 7. Typical current-voltage sweeps of the Ag/MAPbBr ₃ /Pt (MAPbBr ₃ :CF) (a) and Ag/TPBI/MAPbBr ₃ /Pt (MAPbBr ₃ :TPBI) (b) devices. Endurance characteristics of the Ag/MAPbBr ₃ /Pt (MAPbBr ₃ :CF) (c) and Ag/TPBI/MAPbBr ₃ /Pt (MAPbBr ₃ :TPBI) (d) devices	159
Figure 5. 8. ON and OFF mechanisms for the Ag conducting filaments behavior of the Ag/MAPbBr ₃ /Pt (MAPbBr ₃ :CF) (a) and Ag/TPBI/MAPbBr ₃ /Pt (MAPbBr ₃ :TPBI) (b) devices.	161
Figure 5. 9. (a) Electroforming behavior of Ag/TPBI/MAPbBr ₃ /Pt devices. (b) Forming voltage distribution of Ag/TPBI/MAPbBr ₃ /Pt devices. (c) SET and RESET voltage distributions of Ag/TPBI/MAPbBr ₃ /Pt devices. (d) HRS and LRS values for 50 Ag/TPBI/MAPbBr ₃ /Pt devices. (e) Multilevel resistive switching behavior Ag/TPBI/MAPbBr ₃ /Pt device.....	162
Figure 5. 10. (a) Typical <i>I</i> – <i>V</i> curves were plotted by double-logarithmic scales (<i>ln I</i> vs. <i>ln V</i>). Ohmic conduction in the LRS verified by the linear fitting of the proportional relation of current to the voltage. (c) HRS region replotted with <i>ln I</i> ∝ <i>V</i> ^{1/2} to verify whether Schottky emission.	164

Chapter 1

Halide Perovskite Materials: Crystal structures, Electrical properties and Synthesis

1. 1. Introduction

For the past few decades, there has been much interest in alternative energy sources due to increasing awareness on environmental and economic issues. As a result, renewable energy devices, particularly photovoltaic devices, have been studied as prospective energy sources. The archetypical semiconductor is made of crystalline film and possesses efficient charge collection and long-range charge transport, which allows Si-based solar cells to obtain a verified record efficiency of 22.1%.¹ Also, promising photovoltaic devices are being investigated, such as dye-sensitized solar cells and organic photovoltaics; in this context, halide perovskites have attracted huge interest in the photovoltaic field as advanced materials.²⁻⁴

“Perovskite”, named after the Russian mineralogist L.A. Perovski, was discovered in the Ural Mountains of Russia in 1839. Since then, halide perovskite materials have attracted technological and scientific interest due to their great optical and electronic properties with the advantages of low cost fabrication and solution processability.⁵

The term “perovskite” is used when the crystal structure referred to has the general formula ABX_3 . In this structure, A and B are cations, where A is larger than B, and X represents the anion. There are fixed positions for each of A, B, and X, and the ABX_3 perovskite shows a 3D structure corresponding to a corner-sharing octahedral network. Specifically, B cations are surrounded by X anions to form BX_6 . Alternatively, from the viewpoint of the center position B in the tridimensional cubic lattice, A cations are located at the eight corners.^{1,5} With this unit formula of ABX_3 ,

halide perovskites composed of trihalides have been used extensively for photovoltaics as rapid active materials, owing to their useful electrical properties, such as the extraordinarily long diffusion length of electrons, superior charge carrier mobility, wide range of absorption, and high absorption coefficient.⁶ Looking beyond photovoltaics, their exceptional electrical properties render halide perovskite materials competitive for next-generation devices, including light-emitting diodes (LEDs), resistive switching memories, X-ray detectors, lithium-ion batteries, and more, as shown in Figure 1. 1. It is predicted that halide perovskites would be the focus of research for many applications in the near future.

Here, the latest progress in halide perovskites is discussed through intensive theoretical and experimental studies.⁷ The optical and electrical characteristics of halide perovskite materials are analyzed. Also, the concerns and recently discovered issues with halide perovskites are addressed.

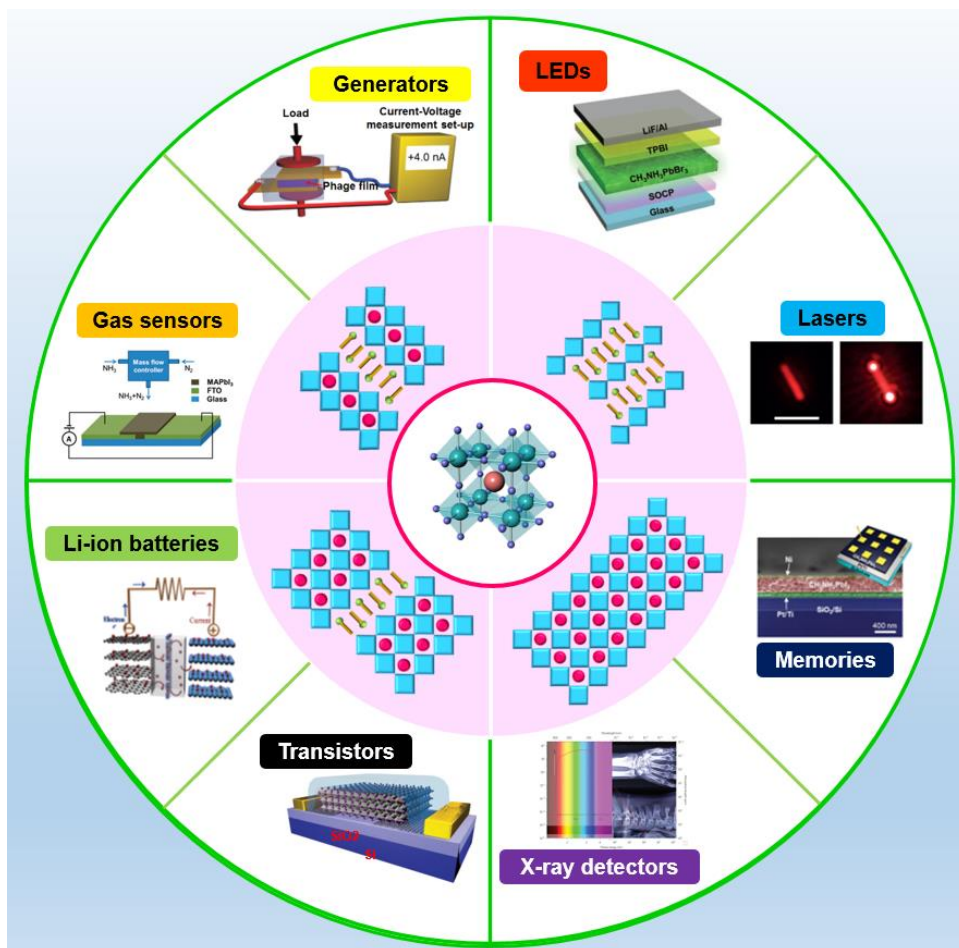


Figure 1. 1. Perovskite devices beyond photovoltaics: LEDs, lasers, memories, transistors, X-ray detectors, Li-ion batteries, piezoelectric energy generators, and gas sensors. Reproduced with permission. Copyright 2015, American Association for the Advancement of Science,⁸ 2017, John Wiley and Sons,⁶⁰ 2015, Nature Publishing Group,^{9,10} 2011, Elsevier,⁴⁸ 2016, John Wiley and Sons,¹¹ 2012, Nature Publishing Group,³³ 2015, Royal Society of Chemistry.³⁴

1. 2. Crystal structures and properties

1. 2. 1. Nanostructure controls

3D perovskites, 2D layered perovskites, and quasi-2D perovskites

As shown in Figure 1. 2, ABX_3 perovskites exhibit 3D structures and that the radii of the A and B cations and X anions dictate their positioning in the unit cell.¹²

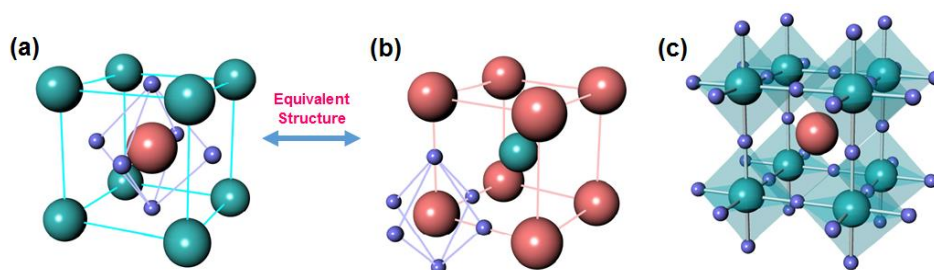


Figure 1. 2. General perovskite structure. (a) Crystal structure of ABX_3 halide perovskite, where A cations are denoted by pink spheres, B cations are denoted by green spheres, and X (halide) anions are denoted by purple spheres. (b) An alternative view of the ABX_3 halide perovskite structure. The crystal structure is equivalent with the Figure on the left. (c) An extended network of ABX_3 halide perovskite linked by corner-shared octahedrons.

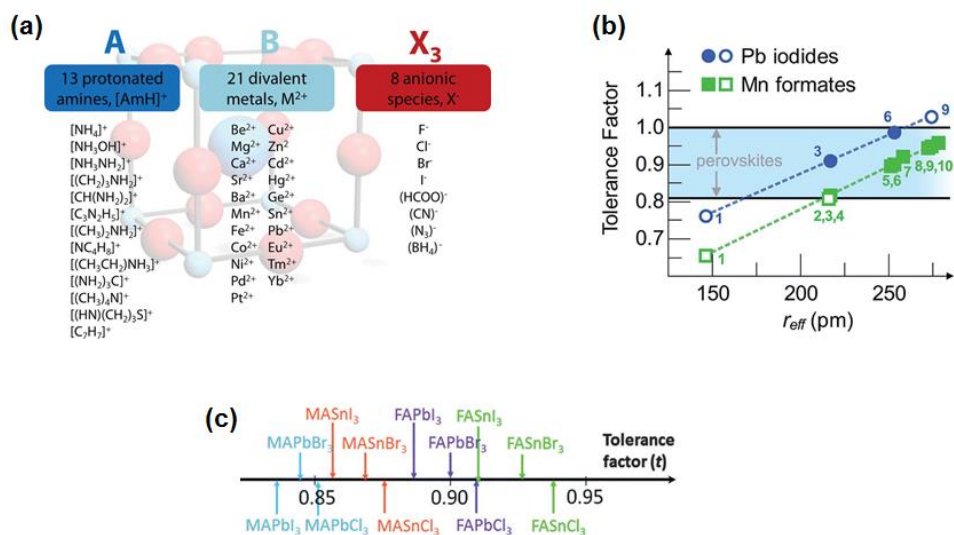


Figure 1.3. (a) 2352 tolerance factors can be calculated, of which 742 lie in the $0.8 < \text{tolerance factor} < 1$ range. (b) Tolerance factors of Pb iodides and Mn formates plotted against cation size. The light blue area indicates the range of the perovskite structure expected. (c) Tolerance factors of lead and tin halide perovskites. Reproduced under the Creative Commons Attribution 4.0 International License and reproduced with permission copyright 2014, 2015 and 2016 Royal Society of Chemistry.^{5,12,13}

In Figure 1. 3 (a), the cations and anions that can be located at A, B, and X sites are listed, but the 742 types can only exist in the tolerance range factor of 0.8 to 1.¹³ For perfectly fitted 3D perovskites, the Goldschmidt tolerance factor and the octahedral factor can be used to estimate their geometric structures.¹² Here, the tolerance factor (t) is defined as $(r_A+r_X)/\sqrt{2}(r_B+r_X)$ and the octahedral factor is defined as r_B/r_X , where r is the ionic radius of A, B, or X in the perovskite.¹³ Figure 1. 3 (b) depicts the tolerance factors of Pb iodides and Mn formates; they are plotted according to the effective radius of A cations and the open symbols indicate a non-perovskite structure.¹³ In Figure 1. 3 (c), the tolerance factors of lead and tin halide perovskites are displayed.^{5,12} Based on the tolerance factor, the t value must be in the range of 0.8 to 1.0 to yield cubic perovskites. Smaller (<0.8) and larger (>1) tolerance factor values yield orthorhombic and hexagonal non-cubic perovskite structures, respectively.^{12,14,15} In addition, the cubic perovskite structure mandates that $0.44 < \text{octahedral factor} < 0.90$.¹⁶

In organic-inorganic halide perovskites (OHPs), to form layered structures with the general formula of ABX_3 , $(RNH_3)_2A_{n-1}B_nX_{3n+1}$ is employed to determine the dimensionalities of the perovskite structure.¹⁷ When $n = 1$, the thinnest and purest 2D layered-perovskite is formed, whereas a 3D bonded perovskite crystal, which are the typically available perovskites, can be expected if n value is ∞ . In the case of intermediate dimensionalities, called quasi-2D layered structures, which lie between 2D and 3D, the n values are defined integers. A schematic of 2D, 3D, and quasi-2D perovskites is presented in Figure 1. 4, according to n values.¹⁸

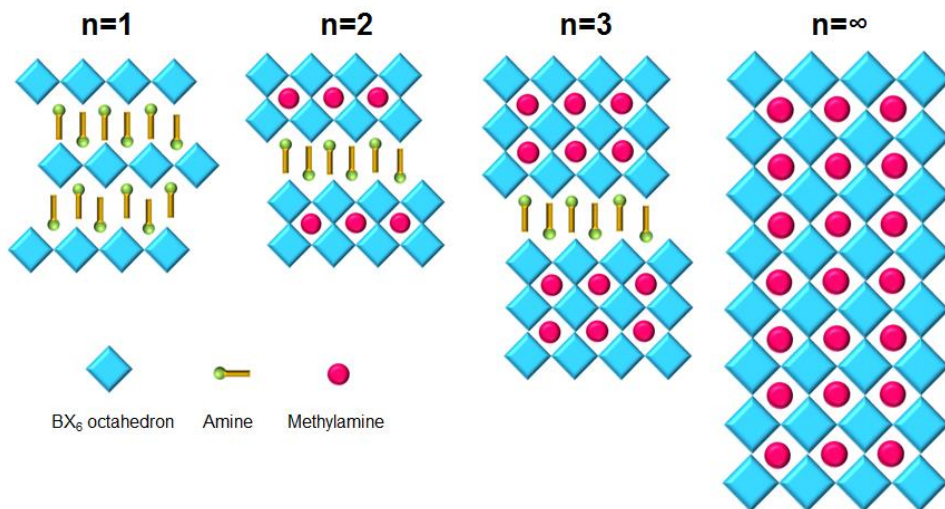


Figure 1. 4. Layered structure of crystalline perovskites with increasing dimensionality (n) from the left to right ($n = 1$ for 2D and $n = \infty$ for 3D, where $n = 1, 2, 3, \dots, \infty$).

The n values point out the number of inorganic cation layers between the two layers of the large A-organic chains.^{19,20} When compared with 3D perovskites of the general formula ABX_3 ($A = Cs^+$, $CH_3NH_3^+$, and $CH(NH_2)_2^+$; $B = Pb^{2+}$ and Sn^{2+} ; $X = Cl^-$, Br^- , and Γ^-), 2D perovskites usually have a general formula of A_2BX_4 ($A = CH_3(CH_2)_nNH_3^+$ and $C_6H_5(CH_2)_nNH_3^+$; $B = Pb^{2+}$ and Sn^{2+} ; $X = Cl^-$, Br^- , and Γ^-).

2D layered perovskite originates from 3D structures when unfit cations are incorporated in the original structures. It leads to a broken cubic symmetry in the structure and the original structures of 3D perovskites are divided into novel $\langle 110 \rangle$ or $\langle 011 \rangle$ -oriented perovskite structures, which can hold larger cations. This means that 3D perovskites are able to accommodate only small cations owing to space limitations, while 2D layered perovskite structures can hold larger A ions, as they have an ionic radius greater than 2.6 \AA .¹ In 2D perovskites with layered structures, the layers interact with each other by weak van der Waals forces and are stacked alternately.¹⁹ In particular, an electronic multi quantum-well is formed in these 2D layered perovskite structures with a strong quantum confinement effect, because a large energy difference exists between the band gap in the inorganic layer and the HOMO-LUMO (Highest Occupied Molecular Orbital-Lowest Unoccupied Molecular Orbital) level in the organic layer. The inorganic layers play a role in the “wells” while the organic molecules act as the “barriers.” As a result, the strong quantum confinement and high compositional flexibility make the 2D layered perovskite a promising material for light-emitting and photovoltaic applications.^{19,21} In these layered structures, analogous compounds called quasi-2D perovskites can be obtained. Generally, quasi-2D

perovskites are formed according to the $(\text{RNH}_3)_2\text{A}_{n-1}\text{B}_n\text{X}_{3n+1}$ formula ($\text{A} = \text{CH}_3\text{NH}_3^+$; $\text{B} = \text{Pb}^{2+}$ and Sn^{2+} ; $\text{X} = \text{Cl}^-$, Br^- , and I^-). In these materials, by tuning the number “n” corresponding to inorganic monolayer sheets, multilayered inorganic sheets are stacked well between organic ammonium layers.

To compare with 3D, 2D, and quasi-2D perovskite structures, 3D halide perovskites, such as $\text{CH}_3\text{NH}_3\text{PbI}_3$ (MAPbI_3) and $\text{CH}_3\text{NH}_3\text{SnI}_3$, are well known for their remarkable properties such as long diffusion lengths, small exciton binding energies, and high extinction coefficients. Despite their outstanding properties, 3D perovskites are unstable due to their highly ionic characteristics. This is because their 3D structure is sensitive to moisture and oxygen, which causes the perovskite crystal structure to decompose. Thus, overcoming the instability of 3D halide perovskites is of significant research interest.

In contrast to 3D halide perovskites, 2D halide perovskites are well known to be more resistant to humidity. 2D perovskites possess unique characteristics in terms of their electrical and optical properties, owing to quantum confinement effects. Particularly, 2D perovskites exhibit superior moisture stability because of the presence of hydrophobic alkylamines in their layered structures.^{22,23} Although 2D materials are stable under high humidity conditions, they are unsuitable light absorbers due to their higher band gaps, poor carrier mobilities, and low absorption coefficients.

Recently, to overcome the drawbacks faced by 2D and 3D halide perovskites, mixed dimensional perovskites called quasi-2D perovskites have been developed; they

combine the excellent air stability of 2D perovskites with the enhanced electronic properties of 3D perovskites. These materials are developed by tuning the average number of layers “n” dimensionally between 2D and 3D perovskites. Therefore, quasi-2D perovskites can be promising materials for photonic applications in the future.^{24,25}

Nanostructured perovskites

Generally, 3D single crystals of halide perovskite bulk thin films have been used in various applications. In some cases, 0D, 1D, and 2D nanostructures of halide perovskites are used owing to their morphologically distinct features.^{1,26,27} Here, each type of halide perovskite nanostructure examples is briefly introduced to understand the effects on morphological properties of the halide perovskites.

For examples of 0D halide perovskites, there are nanoparticles and quantum dots. From Schmidt *et al.*, highly crystalline 6 nm-sized $\text{CH}_3\text{NH}_3\text{PbBr}_3$ (MAPbBr₃) nanoparticles were prepared.²⁸ The nanoparticles were dispersed in various organic solvents due to the medium-sized chain of ammonium bromide. These nanoparticles were stable as solids in concentrated solutions for three months. Also, Rogach’s group demonstrated the size-tunability of MAPbBr₃ perovskite quantum dots.²⁷ The emission peak range was 475-520 nm and it showed outstandingly high quantum yields from 74% up to 93%.

For examples of 1D halide perovskites, there are nanowires, nanorods, etc.^{29–33} By Zhang *et al.*, single-crystalline CsPbBr₃ and CsPbI₃ nanowires were obtained with uniform growth direction.³¹ Also, MAPbI₃ nanowires with the mean diameter of 100 nm were successfully grown by Park's group.³² The MAPbI₃ nanowires were used for perovskite solar cell to enhance hole migration from perovskite to hole transfer layer.

As for 2D halide perovskites, there are nanosheets, nano platelets or nanoflakes.^{29,30} Yang's group investigated atomically thin nanosheets with large size and well-defined square shape.¹⁹ The halide perovskite nanosheet was synthesized with (C₄H₉NH₃)₂PbBr₄ 2D perovskites which possesses a molecular level of 2D structure. The edge length of the square sheets ranged from 1 to 10 nm and the average was 4.2 nm.¹⁹

Lastly, single crystals of halide perovskite can be expressed as 3D halide perovskite in terms of the morphological 3D in nanoscale. The 3D single crystals of bulk thin film have been applied the most in various devices.

1. 2. 2. Electronic properties

Absorption and band gap

Tunable blends and colors are unique properties of halide perovskites, which allow them to work in a wide visible spectral range, which can be extended to near infrared.

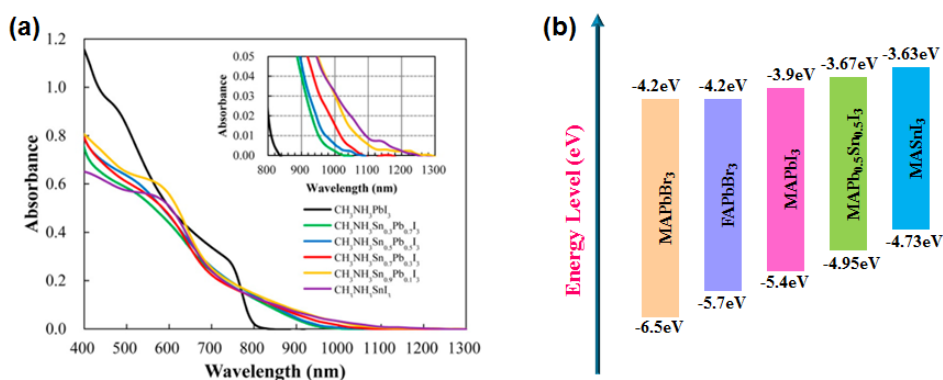


Figure 1. 5. (a) Absorption spectra of $\text{MAPb}_{1-x}\text{Sn}_x\text{I}_3$ perovskites. (b) Energy band diagram of widely tunable halide perovskite materials. Reproduced with permission.

Copyright 2016, ACS publications.⁶

Figure 1. 5 shows the absorption spectra of $\text{MAPb}_{1-x}\text{Sn}_x\text{I}_3$ perovskites and the energy band diagram of widely tunable halide perovskite materials. Theoretically, using the Tauc equation, $[F(R)hv]^n = A(hv - E_g)$, the optical band gap energy (E_g) of halide perovskites can be determined. Here hv is the incident photon energy, A is an empirical constant depending on transition probability, and n is related to the optical absorption process. Specifically, n equals to $1/2$ for an indirect band gap, while its value is 2 for direct band gap.

The electronic levels of halide perovskites are composed of a valence band maximum (VBM) and a conduction band minimum (CBM). Specifically, VBM is related to the antibonding hybrid state influenced by the B-s and X-p orbitals and CBM is determined by the B-p and X-p orbitals, which result in a non-bonding hybrid state.⁴ Previously, in 2004, Park and Chang demonstrated the electronic properties of $\text{CH}_3\text{NH}_3\text{PbX}_3$ and CsPbX_3 with respect to the valence and conduction bands; they showed that the electronic states were primarily affected by the BX_6 octahedral structure, while A-site cations slightly affected the electronic properties.³⁹ The band structures are only slightly influenced when CH_3NH_3 organic cations are replaced by Cs inorganic cations. However, the substitution of halide can dominantly change the electronic states, leading to valence band transition.^{4,39}

Generally, the band gap of halide perovskites can be adjusted in the range of 1.1 eV to 3.0 eV depending on the constituents of the halide sites.^{4,34} Band gaps of 3.11 eV, 2.3 eV, and 1.55 eV could be obtained by using Cl^- , Br^- , and I^- , respectively, in

$\text{CH}_3\text{NH}_3\text{PbX}_3$.¹ Moreover, the band gap can be tuned by partial incorporation of halide constituents. For example, the E_g value of MAPbI_3 is 1.57 eV whereas that of MAPbI_2Br is 1.78 eV.^{35,36}

The changes in the band gap occurred mainly due to the hybridization of orbitals, which takes place when the 4p orbitals of Br overlapped with the 5p orbitals of I and 6s orbitals of Pb. Additionally, the incorporation of Br affects the rise of the valence-band edge, which in turn affects the energy band gap. At vacuum level, the valence-band edges of MAPbI_3 and MAPbI_2Br are estimated to be -5.43 eV and -5.40 eV, respectively. Moreover, the conduction-band edge of MAPbI_2Br (-3.62 eV) is considerably higher than that of MAPbI_3 (-3.86 eV).³⁶

Cation substitution exchange is generally employed to tune the color of emission. By substituting Pb with Sn or by using Sn and Pb blends, the band gap can be radically decreased.⁴ For example, when x in $\text{CH}_3\text{NH}_3\text{Sn}_x\text{Pb}_{1-x}\text{I}_3$ is increased, the band gap gradually reduces. The E_g of $\text{CH}_3\text{NH}_3\text{SnI}_3$ is 1.1eV, whereas its value is 1.31 eV for $\text{CH}_3\text{NH}_3\text{Sn}_{0.3}\text{Pb}_{0.7}\text{I}_3$. At vacuum level, the valence-band edges of $\text{CH}_3\text{NH}_3\text{Sn}_{0.3}\text{Pb}_{0.7}\text{I}_3$ and $\text{CH}_3\text{NH}_3\text{SnI}_3$ are estimated to be -5.12 eV and -4.73 eV, respectively. Meanwhile, the conduction-band edges $\text{CH}_3\text{NH}_3\text{Sn}_{0.3}\text{Pb}_{0.7}\text{I}_3$ and $\text{CH}_3\text{NH}_3\text{SnI}_3$ are -3.81 eV and -3.63 eV, respectively. This indicates that the band gap of Sn/Pb-based halide perovskites can be effectively reduced using a large valence band shift. Based on the band gap tuning, the absorption spectrum edges shift. In the case of $\text{CH}_3\text{NH}_3\text{Sn}_x\text{Pb}_{1-x}\text{I}_3$, the absorption edge shifts from 1000 nm to

1300 nm as x increases from 0.3 to 1.0. This implies that the optical absorbance of halide perovskites can be extended to the near infrared region by tuning their band gaps. Such exotic optical properties render halide perovskites very promising materials for optical devices.^{1,4}

Carrier diffusion lengths

The electron-hole diffusion length (L_D) is determined by $L_D = (k_B T \mu \tau / e)^{1/2}$, where, k_B is the Boltzmann constant, T is the temperature, e is the elementary charge, μ is the carrier mobility, and τ is the carrier lifetime.^{1,37} The carrier diffusion length of MAPbI_3 is generally 100 nm, and it can be extended up to 1 μm using a mixed halide, $\text{CH}_3\text{NH}_3\text{PbI}_{3-x}\text{Cl}_x$, according to transient photo-luminescence measurements.^{4,38} The carrier diffusion length is generally affected by defects or a large density of charge traps, which are substantial in number at the grain boundaries or surfaces of MAPbI_3 polycrystalline films.

The diffusion lengths in MAPbI_3 single crystals are much longer than those in polycrystalline thin films. Previously, carrier diffusion lengths of about 1 μm could be achieved in MAPbI_3 polycrystalline films by solvent annealing. However, using a solution-growth method at low temperatures, long diffusion lengths of about 175 μm could be obtained for MAPbI_3 single crystals. A small charge trap density of single crystals with high carrier mobilities induces longer carrier diffusion lengths.

4,38

Ion migration

In terms of hysteresis, which is related to ion migration, in the current-voltage (I - V) characteristics, halide perovskites have attracted much attention recently. Ion migration is an important factor contributing to the switchable photovoltaic effect, current-voltage hysteresis, and reversible conversion between PbI_2 and MAPbI_3 , which is driven by the electric field in halide perovskite materials and the devices. Ions such as I^- , Pb^{2+} , and MA^+ migrate through the MAPbI_3 films under the action of an electric field. Further, H^+ generation by material decomposition or contamination can take place along with ion migration. Ion migration is generally faster in crystals in which the available interstitial sites are bigger and jumping distance is smaller. In MAPbI_3 , I^- ions, which are located at the edges of the PbI_6^{4-} octahedron, migrate along the I^- - I^- edge and the I^- ions are nearer to the I^- vacancy, compared with MA^+ and Pb^{2+} ions. The ion migration behavior is characterized by the activation energy, which is sensitive to crystal structure, ion jumping distance, and ionic radius. The activation energies for the migration of different ions in MAPbI_3 were calculated to be 0.58 eV (I^-), 2.31 eV (Pb^{2+}), and 0.84 eV (MA^+). These values indicate that I^- ions are highly mobile in MAPbI_3 .^{39,40}

Charge carrier mobility and recombination rates

As mentioned earlier, a long carrier lifetime, high carrier mobility, and low recombination rate are needed to obtain long carrier diffusion lengths for good

device performance. The long charge carrier diffusion lengths of $\text{CH}_3\text{NH}_3\text{PbI}_3$ were demonstrated in terms of the charge mobility using transient terahertz (THz) spectroscopy. The charge carrier mobility was calculated to be $8.0 \text{ cm}^2 \text{ V}^{-1} \text{ s}^{-1}$.⁵⁶ Savenije *et al.* measured the carrier mobility and recombination of MAPbI_3 by combining photo-luminescence experiments and microwave photo-conductance; they also explored the temperature dependence of these parameters.⁴¹ As the temperature decreased, the carrier mobility increased and it was found to be $6.2 \text{ cm}^2 \text{ V}^{-1} \text{ s}^{-1}$ in the tetragonal crystal phase at 300 K, inducing an exciton binding energy of 32 meV. The carrier mobility decreased substantially depending on phase transition from the tetragonal phase to the orthorhombic phase. The orthorhombic phase of $\text{CH}_3\text{NH}_3\text{PbI}_3$ perovskite changed to the tetragonal phase at 161.4 K and the tetragonal phase converted into the cubic phase at 330 K.^{41,42}

To analyze the relationship between carrier mobility and rotation rate with temperature, some formulae have been developed, as described in this section. Electron mobility (μ) is described as $D/k_B T$ according to the Einstein relation, where k_B is the Boltzmann constant, D is the diffusion coefficient, and T is the temperature. In addition, the rotation rate (γ) is proportional to $\exp(-E_a/k_B T)$, where E_a is the activation energy of rotation and the diffusion coefficient is proportional to the rotation rate ($D \propto \gamma$). Therefore, electron mobility can be described as $\mu \propto \exp(-E_a/k_B T)/k_B T$. In this equation, the activation energy (E_a) is limited to a range of 10 meV to 100 meV empirically because activation energy values are unestablished.⁴²

Effective mass

Generally, carrier mobility partially depends on the effective masses of holes and electrons. In comparison with the carrier effective mass in GaAs (0.066 m_0 for electrons in the conduction band and 0.5 m_0 for holes in the valence band), the effective masses of MAPbBr₃ are 0.15 m_0 and 0.25 m_0 corresponding to electrons in the conduction band and holes in the valence band, respectively. It is well known that the hole effective mass in the valence band is relatively smaller than that of electrons in the conduction band. The hole and electron effective masses in inorganic halide perovskites are comparatively smaller than those of organic halide perovskites because the lattice constant of organic cations is larger than that of inorganic cations. For example, the hole and electron effective masses of MAPbI₃ are 0.17 m_0 and 0.33 m_0 , while they are 0.14 m_0 and 0.22 m_0 in CsPbI₃.^{1,43}

1. 3. Synthesis

There has been a plethora of work on the synthesis of halide perovskites, which can be justly considered as some of the most advanced materials; research on the synthesis of halide perovskites has been focused on controlling the synthesis parameters to obtain high-quality halide perovskite films. Because the morphological features and quality of the halide perovskite films decide the device performance, the synthesis process plays a very important role. In this section, two types of synthesis processes are described, solution-chemistry methods and vapor-phase deposition methods.^{5,44}

1. 3. 1. Solution-chemistry techniques

The good solubility of halide perovskites plays a key role in solution-chemistry methods, which include low-cost and facile processes, such as spin coating, screen printing, spray coating, and dip coating. Various one-step and two-step solution techniques for the formation of halide perovskite films have been presented.⁴⁴ In Figure 1. 6 (a), the one-step and two-step methods are compared.^{4,45}

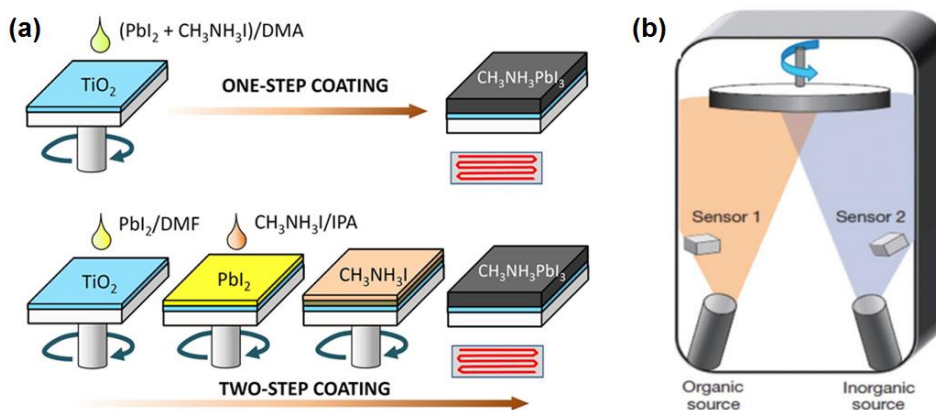


Figure 1. 6. (a) One-step and two-step spin-coating procedures for solution process. (b) Thermal evaporation system for sensitively controlling the pressure in a vacuum chamber. Reproduced with permission. Copyright 2015, Elsevier⁴ and 2016, Royal Society of Chemistry.⁵

One-step method

In the one-step method, the crystallization of films is a key factor for achieving high-quality halide perovskite films; usually, crystallization occurs during the spin-coating or annealing processes. Sometimes, a phenomenon called film shrinkage, which stems from solvent evaporation and crystallization, hinders the halide perovskite films from being formed uniformly. To overcome this issue, retarded crystallization and rapid crystallization strategies are suggested. Retarded crystallization ensures that a smooth precursor film of halide perovskite is achieved; it is then crystallized slowly by controlling the solvent composition.^{46–49} In contrast to the retarded crystallization strategy (slow film-formation process), rapid crystallization employs short annealing periods. As a result, uniform and dense halide perovskite layers are formed on the substrate surface with low surface roughness.^{50–53}

Two-step method

To obtain MAPbI₃ films using a typical two-step process, a solid PbI₂ precursor film is reacted with a MAI solution as a heterogeneous phase. The precursor of PbI₂ can be fabricated in the form of compact films via solution or vapor deposition and the PbI₂ layer structure can be easily intercalated with ammonium, methylamine, or pyridine. The PbI₂ film substantially affects the morphology of the halide perovskite film and MAI diffusion into the PbI₂ lattice dictates the reaction rate; these are the

two key factors dictating perovskite film deposition in two-step processes. Consequently, the diffusion of MAI into the PbI_2 lattice and volume expansion have become major issues.⁵⁴⁻⁵⁶ During the formation of halide perovskite films, some detrimental phenomena, such as film shrinkage, volume expansion, or peeling-off occur. To prevent these, several strategies and techniques to fabricate films of better quality have been suggested.^{57,58}

1. 3. 2. Vapor-phase deposition

Vapor-phase deposition is considered an important process to fabricate halide perovskite films even though multicomponent materials are difficult to be deposited, the synthesis process is very slow, and the process needs complex equipment. Vapor deposition, also called as vacuum deposition, is considerably useful in controlling the thickness of the deposited layer and the deposition rate can be easily monitored. Moreover, patterning techniques can be easily handled by vacuum deposition.^{34,44}

The starting source has to be heated at a high temperature to evaporate and the temperature of the substrate has to be lower than the freezing point of the evaporated materials. Atoms or molecules from the starting source material are thermally released from the bottom of the vacuum chamber and are coated on the substrates. Furthermore, the source vapors have to interact with the substrate alone without any interaction with other residual gas atoms.^{5,40} In the evaporation system shown in Figure 1. 6 (b), the key point is that organic-inorganic halide perovskite compounds

should be evaporated with fast heating for single source deposition. When the metal sheet is heated by high current, the temperature sharply increases. Consequently, the source on the metal holder is ablated and is subsequently deposited on the substrate. In dual-source deposition, both organic and inorganic materials are used and these two separate sources are simultaneously evaporated upwards. The main point is that at high temperature, the inorganic source is rapidly evaporated, whereas the organic source should be protected from thermal decomposition.^{44,59}

1. 4. Challenges

Halide perovskite materials are rapidly emerging as next-generation materials for applications in various fields such as medical diagnostics, energy storage, LEDs, etc. The unique features of these materials confer them several advantages in energy applications and can also extend their application in new areas. Most often, the solution process is used to fabricate flexible halide perovskite films. As flexible electronics are currently a hot topic, flexible halide perovskites films are being considered for fabricating such devices. In addition, the ABX_3 unit cell structure of halide perovskites constituting of various substituents at each site allows the development of different kinds of halide perovskites. Due to these reasons, halide perovskites have achieved great popularity; however, several issues still need to be addressed.

The first challenge is the toxicity of lead. Reports on replacing lead with environmentally friendly elements are few in number because it is difficult to find non-toxic materials which can efficiently replace Pb. It seems that the properties of non-toxic Sn are comparatively similar to those of Pb, and it is expected to enhance the performance of perovskite-based devices more efficiently.⁴

Secondly, the stability of halide perovskites needs to be resolved. Halide perovskites are vulnerable to humidity; however, some techniques are available to ensure the stability of the material in the presence of moisture, such as the inclusion of passivating polymer films on the active layers or the encapsulation of halide

perovskite devices. The instability of halide perovskites is attributed to several factors. The degradation of halide perovskite devices is affected by polarization under an electric field, photo degradation upon exposure to radiation, poor environmental stability, and decomposition under thermal treatment.³⁴

The third issue is the density of defects, which is associated with trap-assisted recombination. The reason for trap-related defects is still an open research question. Nevertheless, it is clear that the density of defects induces charge carrier recombination, leading to a poor device performance. Moreover, vapor-phase deposition methods (vacuum deposition) such as ALD (atomic layer deposition) or CVD (chemical vapor deposition) need to be further developed. Generally, solution techniques, such as spin-coating, are used to synthesize halide perovskites because they are more feasible than vapor-phase deposition methods. However, to accurately control the thickness, the synthesis of halide perovskites needs to be accomplished in the vapor phase. Lastly, the formation of halide perovskite films of large surface areas is to be made feasible.

These challenges are to be addressed in the future in order to facilitate large-scale commercial production of halide perovskite devices.

1. 5. Conclusions

Halide perovskites have experienced rapid advancements for application in different areas over the past few years and their unique properties have attracted both industrial interest and academic curiosity. Here, we described halide perovskite structure formation with respect to 3D perovskites, 2D layered perovskites, and quasi-2D perovskites, including the fabrication processes and described several key optical and electrical properties, such as tunable optical bandgap, carrier diffusion length, and ion migration. Available literature on halide perovskite devices was reviewed and we presented an overall view on the methods employed to enhance the performance of halide perovskite-based devices. And several key challenges faced by halide perovskites are highlighted; these challenges need to be addressed to fully realize the commercial potential of these unique materials. We strongly believe that progress in halide perovskite materials would pave the way for advancements in information, energy, medical, and environmental technologies.

1. 6. Reference

- 1 S. A. Veldhuis, P. P. Boix, N. Yantara, M. Li, T. C. Sum, N. Mathews and S. G. Mhaisalkar, *Adv. Mater.*, 2016, **28**, 6804–6834.
- 2 H. Kim, G. Veerappan and J. H. Park, *Electrochim. Acta*, 2014, **137**, 164–168.
- 3 H. Kim, G. Veerappan, D. H. Wang and J. H. Park, *Electrochim. Acta*, 2016, **187**, 218–223.
- 4 Q. Chen, N. De Marco, Y. (Michael) Yang, T.-B. Song, C.-C. Chen, H. Zhao, Z. Hong, H. Zhou and Y. Yang, *Nano Today*, 2015, **10**, 355–396.
- 5 Y. Zhao and K. Zhu, *Chem. Soc. Rev.*, 2016, **45**, 655–689.
- 6 A. R. B. M. Yusoff and M. K. Nazeeruddin, *J. Phys. Chem. Lett.*, 2016, **7**, 851–866.
- 7 H. Huang, L. Polavarapu, J. A. Sichert, A. S. Sussha, A. S. Urban and A. L. Rogach, *NPG Asia Mater.*, 2016, **8**, e328–e328.
- 8 H. Cho, S.-H. Jeong, M.-H. Park, Y.-H. Kim, C. Wolf, C.-L. Lee, J. H. Heo, A. Sadhanala, N. Myoung, S. Yoo, S. H. Im, R. H. Friend and T.-W. Lee, *Science (80-.)*, 2015, **350**, 1222–1225.
- 9 H. Zhu, Y. Fu, F. Meng, X. Wu, Z. Gong, Q. Ding, M. V. Gustafsson, M. T. Trinh, S. Jin and X.-Y. Zhu, *Nat. Mater.*, 2015, **14**, 636–642.

- 10 S. Yakunin, M. Sytnyk, D. Kriegner, S. Shrestha, M. Richter, G. J. Matt, H. Azimi, C. J. Brabec, J. Stangl, M. V. Kovalenko and W. Heiss, *Nat. Photonics*, 2015, **9**, 444–449.
- 11 J. Choi, S. Park, J. Lee, K. Hong, D.-H. Kim, C. W. Moon, G. Do Park, J. Suh, J. Hwang, S. Y. Kim, H. S. Jung, N.-G. Park, S. Han, K. T. Nam and H. W. Jang, *Adv. Mater.*, 2016, **28**, 6562–6567.
- 12 G. Kieslich, S. Sun and A. K. Cheetham, *Chem. Sci.*, 2014, **5**, 4712–4715.
- 13 G. Kieslich, S. Sun and A. K. Cheetham, *Chem. Sci.*, 2015, **6**, 3430–3433.
- 14 D. B. Mitzi, *J. Chem. Soc. Dalton Trans.*, 2001, 1–12.
- 15 Z. Li, M. Yang, J.-S. Park, S.-H. Wei, J. J. Berry and K. Zhu, *Chem. Mater.*, 2016, **28**, 284–292.
- 16 M. A. Green, A. Ho-Baillie and H. J. Snaith, *Nat. Photonics*, 2014, **8**, 506–514.
- 17 A. Vassilakopoulou, D. Papadatos, I. Zakouras and I. Koutselas, *J. Alloys Compd.*, 2017, **692**, 589–598.
- 18 A. Vassilakopoulou, D. Papadatos and I. Koutselas, *Appl. Surf. Sci.*, 2017, **400**, 434–439.
- 19 L. Dou, A. B. Wong, Y. Yu, M. Lai, N. Kornienko, S. W. Eaton, A. Fu, C. G. Bischak, J. Ma, T. Ding, N. S. Ginsberg, L.-W. Wang, A. P. Alivisatos and P. Yang, *Science (80-.)*, 2015, **349**, 1518–1521.
- 20 Z. Cheng and J. Lin, *CrystEngComm*, 2010, **12**, 2646.

- 21 K. Gauthron, J. Lauret, L. Doyennette, G. Lanty, A. Al Choueiry, S. J. Zhang, L. Largeau, O. Mauguin, J. Bloch and E. Deleporte, 2010, **18**, 5912–5919.
- 22 R. Hamaguchi, M. Yoshizawa-Fujita, T. Miyasaka, H. Kunugita, K. Ema, Y. Takeoka and M. Rikukawa, *Chem. Commun.*, 2017, **53**, 4366–4369.
- 23 M.-H. Jung, *Electrochim. Acta*, 2017, **240**, 98–107.
- 24 L. N. Quan, M. Yuan, R. Comin, O. Voznyy, D. H. Kim and E. H. Sargent, *SPIE Newsroom*, , DOI:10.1117/2.1201608.006639.
- 25 Z. Yuan, Y. Shu, Y. Xin and B. Ma, *Chem. Commun.*, 2016, **52**, 3887–3890.
- 26 T. Udayabhaskararao, M. Kazes, L. Houben, H. Lin and D. Oron, *Chem. Mater.*, 2017, **29**, 1302–1308.
- 27 H. Huang, A. S. Susha, S. V. Kershaw, T. F. Hung and A. L. Rogach, *Adv. Sci.*, 2015, **2**, 1500194.
- 28 L. C. Schmidt, A. Pertegás, S. Gonzalez-carrero, O. Malinkiewicz, S. Agouram, G. M. Espallargas, H. J. Bolink, R. E. Galian, J. Pérez-prieto and S. González-carrero, *J. Am. Chem. Soc.*, 2014, **136**, 850–853.
- 29 S.-T. Ha, R. Su, J. Xing, Q. Zhang and Q. Xiong, *Chem. Sci.*, 2017, **8**, 2522–2536.
- 30 O. Vybornyi, S. Yakunin and M. V. Kovalenko, *Nanoscale*, 2016, **8**, 6278–6283.

- 31 D. Zhang, S. W. Eaton, Y. Yu, L. Dou and P. Yang, *J. Am. Chem. Soc.*, 2015, **137**, 9230–9233.
- 32 J.-H. Im, J. Luo, M. Franckevičius, N. Pellet, P. Gao, T. Moehl, S. M. Zakeeruddin, M. K. Nazeeruddin, M. Grätzel and N.-G. Park, *Nano Lett.*, 2015, **15**, 2120–2126.
- 33 B. Y. Lee, J. Zhang, C. Zueger, W.-J. Chung, S. Y. Yoo, E. Wang, J. Meyer, R. Ramesh, S.-W. Lee, *Nature Nanotechnology* **2012**, *7*, 351.
- 34 C. Bao, J. Yang, W. Zhu, X. Zhou, H. Gao, F. Li, G. Fu, T. Yu, Z. Zou, *Chem. Commun.* **2015**, *51*, 15426.
- 35 H.-S. Kim, C.-R. Lee, J.-H. Im, K.-B. Lee, T. Moehl, A. Marchioro, S.-J. Moon, R. Humphry-Baker, J.-H. Yum, J. E. Moser, M. Grätzel and N.-G. Park, *Sci. Rep.*, 2012, **2**, 591.
- 36 J. Qiu, Y. Qiu, K. Yan, M. Zhong, C. Mu, H. Yan and S. Yang, *Nanoscale*, 2013, **5**, 3245.
- 37 B. Y. Lee, J. Zhang, C. Zueger, W.-J. Chung, S. Y. Yoo, E. Wang, J. Meyer, R. Ramesh and S.-W. Lee, *Nat. Nanotechnol.*, 2012, **7**, 351–356.
- 38 C. Bao, J. Yang, W. Zhu, X. Zhou, H. Gao, F. Li, G. Fu, T. Yu and Z. Zou, *Chem. Commun.*, 2015, **51**, 15426–15429.
- 39 Y. Yuan and J. Huang, *Acc. Chem. Res.*, 2016, **49**, 286–293.
- 40 C. Eames, J. M. Frost, P. R. F. Barnes, B. C. O’Regan, A. Walsh and M. S. Islam, *Nat. Commun.*, 2015, **6**, 7497.

- 41 T. J. Savenije, C. S. Ponseca, L. Kunneman, M. Abdellah, K. Zheng, Y. Tian, Q. Zhu, S. E. Canton, I. G. Scheblykin, T. Pullerits, A. Yartsev and V. Sundström, *J. Phys. Chem. Lett.*, 2014, **5**, 2189–2194.
- 42 J. Ma and L.-W. Wang, *Nano Lett.*, 2017, **17**, 3646–3654.
- 43 Y. H. Chang, C. H. Park and K. Matsuishi, *J. Korean Phys. Soc.*, 2004, **44**, 889–893.
- 44 M. Petrović, V. Chellappan and S. Ramakrishna, *Sol. Energy*, 2015, **122**, 678–699.
- 45 J.-H. Im, H.-S. Kim and N.-G. Park, *APL Mater.*, 2014, **2**, 081510.
- 46 J.-H. Im, C.-R. Lee, J.-W. Lee, S.-W. Park and N.-G. Park, *Nanoscale*, 2011, **3**, 4088.
- 47 Y. Wu, A. Islam, X. Yang, C. Qin, J. Liu, K. Zhang, W. Peng and L. Han, *Energy Environ. Sci.*, 2014, **7**, 2934–2938.
- 48 M.-K. Song, S. Park, F. M. Alamgir, J. Cho, M. Liu, *Materials Science and Engineering* **2011**, 72, 203.
- 49 G. E. Eperon, V. M. Burlakov, P. Docampo, A. Goriely and H. J. Snaith, *Adv. Funct. Mater.*, 2014, **24**, 151–157.
- 50 N. J. Jeon, J. H. Noh, Y. C. Kim, W. S. Yang, S. Ryu and S. Il Seok, *Nat. Mater.*, 2014, **13**, 897–903.

- 51 M. Xiao, F. Huang, W. Huang, Y. Dkhissi, Y. Zhu, J. Etheridge, A. Gray-Weale, U. Bach, Y.-B. Cheng and L. Spiccia, *Angew. Chemie*, 2014, **126**, 10056–10061.
- 52 M.-K. Song, S. Park, F. M. Alamgir, J. Cho and M. Liu, *Mater. Sci. Eng. R Reports*, 2011, **72**, 203–252.
- 53 W. Nie, H. Tsai, R. Asadpour, A. J. Neukirch, G. Gupta, J. J. Crochet, M. Chhowalla, S. Tretiak, M. A. Alam and H. Wang, 2015, **347**, 522–526.
- 54 L. Zheng, Y. Ma, S. Chu, S. Wang, B. Qu, L. Xiao, Z. Chen, Q. Gong, Z. Wu and X. Hou, *Nanoscale*, 2014, **6**, 8171–8176.
- 55 Q. Chen, H. Zhou, Z. Hong, S. Luo, H.-S. Duan, H.-H. Wang, Y. Liu, G. Li and Y. Yang, *J. Am. Chem. Soc.*, 2014, **136**, 622–625.
- 56 Z. Xiao, Q. Dong, C. Bi, Y. Shao, Y. Yuan and J. Huang, *Adv. Mater.*, 2014, **26**, 6503–6509.
- 57 L. Chen, F. Tang, Y. Wang, S. Gao, W. Cao, J. Cai and L. Chen, *Nano Res.*, 2015, **8**, 263–270.
- 58 W. S. Yang, J. H. Noh, N. J. Jeon, Y. C. Kim, S. Ryu, J. Seo and S. Il Seok, *Science (80-.)*, 2015, **348**, 1234–1237.
- 59 D. Li, H.-C. Cheng, Y. Wang, Z. Zhao, G. Wang, H. Wu, Q. He, Y. Huang and X. Duan, *Adv. Mater.*, 2017, **29**, 1601959.
- 60 D. Li, H.-C. Cheng, Y. Wang, Z. Zhao, G. Wang, H. Wu, Q. He, Y. Huang, X. Duan, *Advanced Materials* **2017**, *29*, 1601959.

Chapter 2

The Operational Mechanisms of Resistive Switching Memories based Halide perovskites

2. 1. Introduction

Because photovoltaic devices have been targeted as prospective energy sources over the past several decades,¹⁻⁴ the emergence of halide perovskite solar cells are creating a significant impact throughout the fields of semiconductor research and technology. In general, the term of “halide perovskites” can be described as the crystal structure of the chemical formula ABX_3 .⁵ In terms of light absorbers, the noteworthy advantages of halide perovskites lead to great successes in photovoltaic technologies, thereby achieving power conversion efficiencies of 22.7%.⁶⁻⁸

Following the extensive impacts of halide perovskites as light absorbers, the scientific potential of the material is broadened to other electronic devices beyond photovoltaics, such as resistive-switching memories, artificial synapses, and field-effect transistors. These additional applications are achievable owing to other characteristics of halide perovskites, such as *I-V* hysteresis caused by ion migration. In particular, resistance random access memory (ReRAM) devices have great potential in next-generation memory devices because of their wide selection of switching materials. Switching memories based on oxide materials such as TiO_2 ,⁹ Ta_2O_{5-x} ,¹⁰ $Pr_{0.7}Ca_{0.3}MnO_3$ (PCMO),¹¹ and $BiFeO_3$ ¹² have already been thoroughly investigated.

Also, halide perovskites can be potential candidates as switching materials. Compared to conventional ReRAM devices which spent many years being investigated, halide perovskite-based ReRAMs show incredibly fast investigation

and development. Moreover, a comparable difference exists in the constituent tuning of A, B, and X components in ABX_3 framework. Their constituent tuning can be an influential factor to decide the band gap which leads to different Schottky barrier heights. The effect is important to decide the ON/OFF resistive ratio in memory device.¹³

Additionally, compared to conventional ReRAMs, halide perovskite based ReRAMs show high ON/OFF ratio and the transition to low resistance state (ON state) without electroforming process at low voltages. However, studies on halide-perovskite-based ReRAM devices have not been conducted much; one example of such a device is a resistive switching mechanism. Therefore, a significant amount of research is necessary because the technology may prove to be an important research field in the future.

In this study, we briefly discuss the operating mechanism of ReRAM devices. In addition, ReRAM devices are introduced as classified halide perovskite materials, and finally, we offer current challenges as well as our potential future directions in these areas.

2. 2. Principles of ReRAM devices

As the demand for high-density, high-performance memory devices increases, ReRAM devices have received increased attention as a potential next-generation non-volatile memory device because of their simple structure, fast operating speed, high memory density, low power consumption, and low fabrication cost.¹⁴ Moreover, an advantage of ReRAM is that the device can be investigated with various materials, and halide perovskites are also one of the switching materials. This investigation may serve as a future research topic.

In this section, basic principles of ReRAM devices are explained to provide insight into the studies on previously developed halide perovskite ReRAM.

2. 2. 1. ReRAM device structure and the resistive switching mechanisms

Generally, ReRAM is a metal-insulator-metal (MIM) stack, which is a two-terminal device. The memory elements consist of an upper and lower electrode, and an insulating switching layer between the two electrodes.

When voltage or current is applied across the MIM stack, the electrode, where external bias is applied, is called the top electrode and another electrode, which acts as electrically grounded electrode, is referred to the bottom electrode.¹⁵

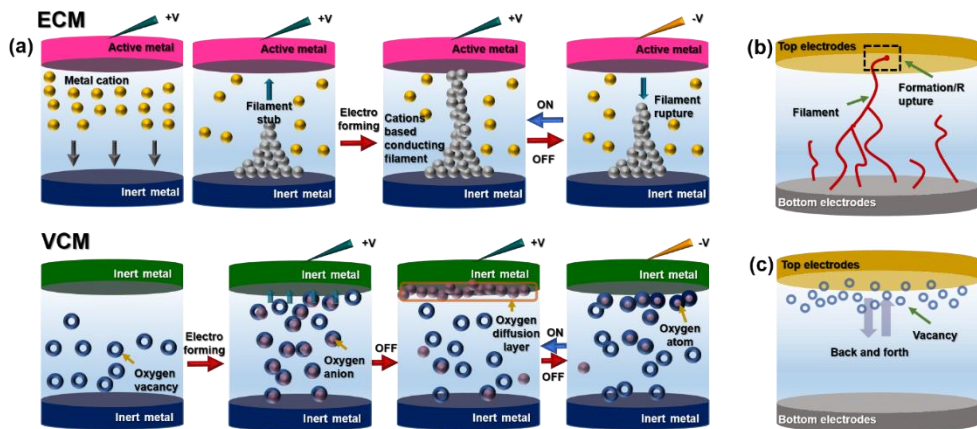


Figure 2. 1. (a) The operating mechanism of the resistive switching behaviour; electroforming process, filament formation, and rupture in switching layer. (b) The filamentary-type switching mechanism and (c) interface-type switching mechanism.

Basically, the device is operated by the reversible soft breakdown of an insulator. This leads to a change in its resistance by simply applying external bias, and Figure 2. 1(a) schematically illustrates electrochemical metallization mechanism (ECM) and valence change mechanism (VCM) of the ReRAM. In this Figure, the ECM is defined as the formation of cation based conducting filaments by an active metal electrode. Meanwhile, VCM is the change in electronic conductivity due to enriched oxygen with the utilization of inert metal electrode.¹⁶⁻²⁰

When a high voltage stress is applied, the high initial resistance state is changed to a low resistance state (LRS), which is called “electroforming.” Forming-free devices, which do not show this process, are required due to the high voltage stress that occurs when the device is initially operated. Following the electroforming process, when the opposite threshold voltage is applied, the LRS is switched to a high-resistance state (HRS) at the particular voltage (reset voltage), which is called “RESET process.” Then, the “SET process,” which refers to the switching from a HRS to a LRS, occurs at the set voltage in a manner opposite to the reset process. In the resistive switching operation, the changes from the SET to RESET process indicates an “ON” state, and the opposite behaviour indicates an “OFF” state. Generally, in order to avoid device damage during the set process, the current is limited through current compliance (CC) by adding a series resistor. These resistive switching behaviours are observed in many insulating oxides as well as halide perovskites.

There are several models for ECM or VCM devices in halide perovskite memory device. Menzel et al. suggested simulation models to explain ECM devices.^{22,23} The device which employed Ag as a top electrode is mostly 1-dimensional model, which means ions from the anode surface are pulled by the electric field and reduced at the cathode to form a filament.¹⁶ Also, Larentis et al. suggested electrical conduction model and thermal model to explain VCM devices.^{24,25} The device which employed Au as a top electrode shows VCM switching mechanism, which is occurred by ion migration including diffusion and drift components. To prove ion-migration flux for halide perovskite ReRAM, electrical conduction model, which is electrical conductivity in the conductive filament, is needed.

2. 2. 2. The filamentary-type and interface-type halide perovskite memory devices

Generally, the switching mechanism can be classified as a filamentary-type and interface-type depending on the type of conducting path.

Figure 1. 2(b) shows filament-type memory devices. From the applied suitable external bias, it shows resistive switching behaviour by the formation and rupture of conducting filaments in the insulating layer, which takes place during the SET and RESET processes, respectively.^{15,21}

The other type is the interface-type memory device, for which resistive switching occurs at the interface between the switching material and metal electrode, as shown in Figure 1. 2(c).¹⁹

Generally, the difference between filamentary and interface resistive switching depends on the area. In the filamentary switching, the current conduction is narrowly confined to a narrow part of the device area.²⁷ The most common metallic bridges, which bring about resistive switching by formation and rupture, are generated by the migration of metal atoms (e.g., Ag and Cu) originating from electrodes crossing the insulating layer.²⁸

In general, halide-perovskite-based ReRAM devices conduct filamentary conducting paths by employing electrochemically active metal electrodes. For example, Yoo et al. reported a resistive switching memory device using a structure of Ag/CH₃NH₃PbCl_xI_{3-x}/fluorine-doped tin oxide (FTO) in 2016.²⁹ The authors explained that Ag conducting filaments played a key role in the formation and rupture of the resistive switching phenomenon.

In contrast, in interface switching, the resistance change occurs by field-induced modification over the entire electrode area.^{28,30} In 2015, Yoo et al. developed memory devices that were fabricated with Au and a CH₃NH₃PbCl_xI_{3-x} on FTO substrates.⁸⁶ The device performed at a low operating voltage of < 1 V, showed reliable endurance of 4100 times, and demonstrated a long retention time of 4104 s while showing typical resistive switching behaviour. In this paper, the authors

suggested trap-controlled space-charge-limited conduction (SCLC), which is related to charge carrier trapping. It means that this device is an interface type because traps are sited at the interface between a perovskite layer and an electrode.

2. 2. 3. Challenging issues of ReRAMs

As mentioned above, ReRAM is a metal-insulator-metal (MIM) stack, which is a two-terminal device. However, the voltage-time dilemma remains a fundamental problem of two-terminal ReRAM devices. This means switching occurs at reasonable voltages in the nanosecond regime, but a small read voltage should not disturb the device state when reading for a long time or frequently in series. To overcome long-lasting read-disturb, switching kinetics should show a non-linearity, spanning over 15 orders of magnitude.³²

To achieve a high non-linearity, the electrochemical and physical processes such as electro-crystallization, ion migration, and threshold switching, that determine switching kinetics of ECM and VCM, have to be confirmed.

In ECM processes, electro-crystallization dominates switching behaviour at low voltages, whereas electron-transfer at middle voltage and ion migration at high voltages limit the switching kinetics. Meanwhile, in VCM processes, ion migration is field-accelerated at low voltage and the process is determined by local temperature increase at high voltages.³² With these understating of electrochemical or physical

processes, ECM and VCM devices can exhibit sufficiently strong non-linearity of switching kinetics to overcome the voltage-time dilemma.

The second issue is referred to as the sneak path problem. Compared to other memory devices, ReRAM device can be fabricated with only 2 access lines, which makes cross-point array structure possible. It is feasible to maximize the integration of memory device by employing cross-point array. Moreover, 3D multi-layered stack is possible for extremely dense data storage.³³

Thus, cross-point array structure of resistive switching memory has been actively investigated. However, one access line is connected with other neighbouring cells in a cross-point array and sneak current occurs from other neighbouring cells. Due to the sneak current, ReRAM has the problem with read failure, which should be solved. To solve this issue, a selector is inserted with a resistive switching material into a cell, preventing the unselected cell from interfering with the sensing current of the selected cell, thus mitigating sneak current.³⁴ After the demands of selector in a cross-point array was suggested, development of various selector materials is needed.

Lastly, the third issue is the ReRAM reliability of the programmed states. This refers to the reduction of resistance stability of the device after programming due to the plasticity behaviour, which finally leads to read errors.^{35,36} The phenomena of program instability under continuous programming conditions also need to be studied.

2. 3. Switching memory device based on halide perovskites

As the research about halide perovskite photovoltaic devices has reached its peak, the hysteresis behaviour in the $I-V$ characterization produced by light or voltage biasing conditions has been studied.

The hysteresis, an undesirable shift in the $I-V$ curve, may come from ferroelectricity, charge trapping, or ion migration.³⁷⁻³⁹ Several types of point defects, for example vacancies (V_{Pb} , V_{MA} , V_I), interstitials (Pb_i , MA_i , I_i), and antisites (Pb_I , I_{Pb}) in $CH_3NH_3PbI_3$ (MAPbI₃) may bring about a range of energy levels, which leads to charge trapping at these energy levels.⁴⁰⁻⁴² In addition, ferroelectric polarization can be stimulated and released by positive and negative poling.^{40,42,43} Thus, halide perovskites can be strongly suggested for a switching material for ReRAM device. Here, we introduce the advanced studies on ReRAM devices based on classified halide perovskite materials.

2. 3. 1. Organic-inorganic hybrid halide perovskite based ReRAMs

Since Yoo et al. first investigated organic-inorganic hybrid halide perovskite ReRAMs based on $CH_3NH_3PbCl_xI_{3-x}$ that show hysteretic $I-V$ characteristics in 2015, the performance of ReRAM devices has been gradually improving.^{28,31} In organic-inorganic hybrid halide perovskite, common organic cations include CH_3NH_3 (MA) and $HC(NH_2)_2$ (FA), while the metal cations are typically Pb (lead) or Sn (tin) and

serve as the inorganic cations. In general, MAPbI₃-based memory devices among halide perovskite ReRAMs have been widely investigated.

In 2016, Lee and co-workers demonstrated a resistive switching mechanism using MAPbI₃ sandwiched between Au and indium tin oxide (ITO) using a simple solution process.⁴⁰ The device achieved a constant ON/OFF ratio as high as 10⁴, a switching endurance of 400 cycles, and low operating voltage of approximately 0.7 V. Based on this performance, the resistive switching behaviour was thought to be I (iodide) vacancy defect because its activation energy (0.58 eV) of formation is the lowest among the MA, Pb, and I defects.⁴⁴ The I defect hopping along neighbouring atoms easily migrates along the corner-sharing BX₆ octahedral edge in the perovskite structure. When the applied voltage increases, the I defect builds filaments from the bottom to the top, then electrons can move by trap-to-trap hopping along the occupied traps during the SET process.

As previously understood, the hysteresis of the *I-V* curve originates from the ionic motion/migration and charge trapping/detrapping at the bulk or interface traps of halide perovskites.⁴⁵ Thus, in 2017, Im and Jo demonstrated that the hysteresis was related to the domain size of halide perovskite film by fabricating an Au/MAPbI₃/ITO structure.⁴⁶ To prove that a small crystal grain size enhances hysteresis, which improves ReRAM switching performance, MAPbI₃ films with different grain sizes were synthesized by an inter-diffusion controlled dripping method using a toluene and iso-propyl alcohol mixture. The grain sizes of the

MAPbI₃ films were controlled in the range from 60–600 nm, and the ON/OFF ratio was slightly increased and saturated as the grain size decreased. When the average grain size was 60 nm, the device exhibited 600 endurance cycles, a data retention time of 10⁴ s, and 0.7 V and -0.61 V set and reset voltages, respectively. To confirm the grain size effect, their trap densities were calculated. This indicated that the surface traps in the grain boundaries might be slightly related to the grain size of the MAPbI₃ films, and they may also affect the switching behaviour in the memory device. However, the author mentioned that it was not clear how the surface traps affect the resistive switching behaviour owing to the slightly changed trap densities, as well as leaky dielectric behaviour caused by changes in grain sizes. It seems likely that further studies on the relations between the status of the film and the switching behaviour of memory device are needed.

As those two studies mentioned above, the organic-inorganic hybrid halide perovskite-based ReRAM devices were assembled using Au as a top electrode and ITO as a bottom electrode; however, Choi. et al. conducted the fabrication of a MAPbI₃ based memory device using an Ag top electrode, which is a highly active metal, and Pt on the SiO₂/Si substrate as the bottom electrode.

Figure 2. 2(a) shows the unit cell of MAPbI₃.⁴⁷ Compared to the device fabricated with an Ni and Au top electrode (which showed a high operating voltage of ±0.4 V), this Ag/MAPbI₃/Pt structured memory device exhibited a much lower operating voltage of ±0.14 V.

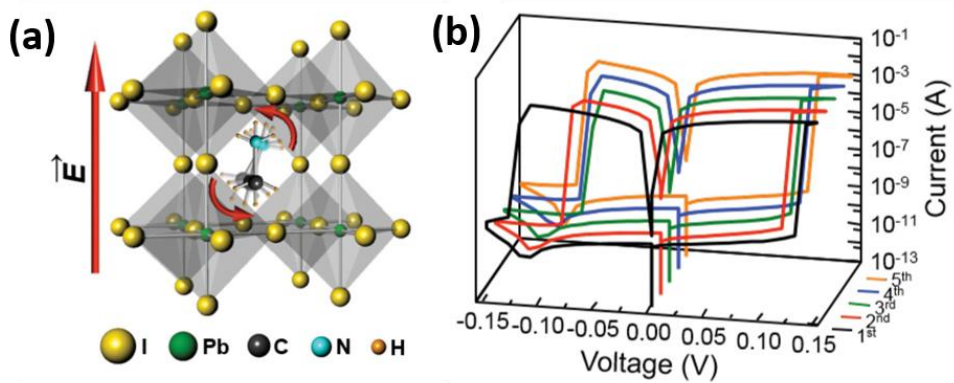


Figure 2. 2. (a) The organic-inorganic halide perovskite structure (a unit cell of MAPbI₃). (b) The five initial *I-V* sweeps of a Ag/MAPbI₃/Pt cell. Reproduced with permission.⁴⁷ Copyright 2016, John Wiley and Sons.

This indicates that the electrochemically active top electrode boosts the resistive switching behaviour. As shown in Figure 2. 2(b),⁴⁷ reliable resistive switching can be seen with no remarkable variation for the five initial voltage sweeps, exhibiting the high ON/OFF of 10^6 . The most important point in this research is that the device presented four level resistance states by setting current CC, which means multilevel data storage. The CC, which regulates the upper limit of the currents in LRS with no change to the operating voltage, can modulate the resistive switching mechanism, and under four different CC (10^{-3} , 10^{-4} , 10^{-5} , and 10^{-6} A) in the SET process, four different ON states were operated. Thus, according to this multilevel resistive switching behaviour, it will be feasible to improve the data storage density of the device.⁴⁸

2. 3. 2. All inorganic halide perovskite based ReRAMs

Unfortunately, the organic-inorganic hybrid halide perovskite materials are vulnerable to ambient conditions owing to their organic groups, and especially poor photo and thermal stability are the main obstacles for storage, fabrication, and operation, which is a bottleneck for potential future applications.⁴⁹⁻⁵²

To solve this issue, the organic cation can be replaced with an inorganic cation. For example, all-inorganic perovskites based on cesium (Cs) cations are known to be thermally stable above 100 °C, maintaining their structural and electrical properties.^{53,54}

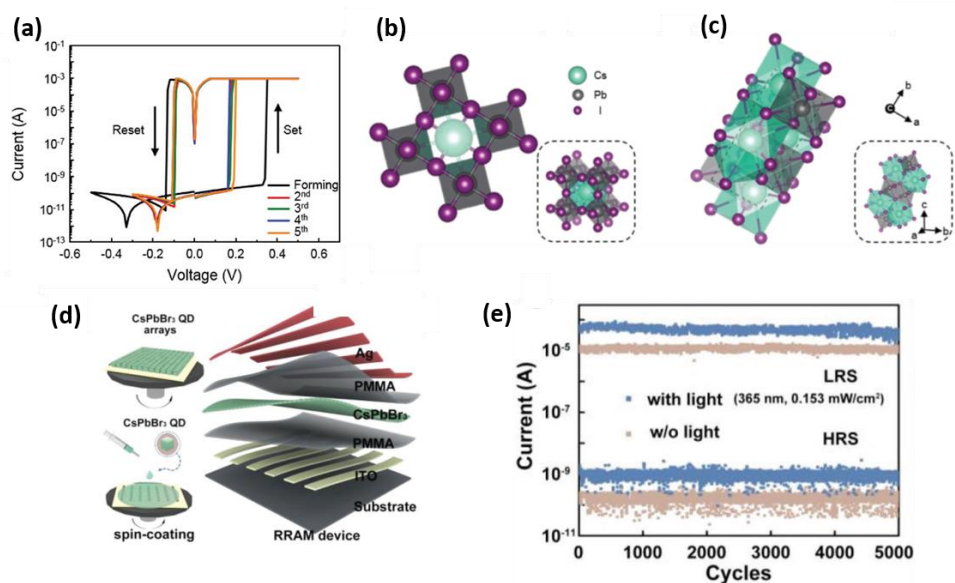


Figure 2. 3. (a) The five initial series voltage sweeps of a Ag/PMMA/CsPbI₃/Pt device. The phase transition from cubic phase (perovskite) (b) to the orthorhombic phase (non-perovskite) (c). Reproduced with permission.⁵⁵ Copyright 2017, John Wiley and Sons. (d) Schematic drawings of the CsPbBr₃ QD-based ReRAM device fabrication process via all-solution process. (e) Endurance results under light illumination and dark condition. Reproduced with permission.⁵⁶ Copyright 2018, John Wiley and Sons.

Han et al. reported an air-stable CsPbI₃-perovskite-film-based device with an Ag/polymethylmethacrylate(PMMA)/CsPbI₃/Pt structure that showed a high ON/OFF ratio of 10⁶ (Figure 2. 3(a)), a low operating voltage under 0.2 V, and reproducible resistive switching with ON/OFF ratios over 300 cycles.⁵⁵ In this research, the CsPbI₃ was employed to confirm that the resistive switching behaviour corresponded to the transitioned perovskite phase. This is because CsPbI₃ is the most unstable among the cesium lead halide perovskites.

In Figure 2. 3(b, c), the phase transition from the cubic phase (perovskite) to the orthorhombic phase (non-perovskite) reduces the structural flexibility, which degrades the switching property.⁵⁵ In the cubic phase, a defect easily moves along the 1D-like migration path⁴⁴ in a linearly ordered corner-shared PbI₆ octahedra; whereas, in the orthorhombic phase, the double chain structure of edge-shared PbI₆ octahedra makes defect migration inconvenient. Thus, it can be seen that the stability of halide perovskites, which determines the resistive switching property, are related to perovskite phase transitions.

Very recently, Wang et al. fabricated a photonic ReRAM using Ag (top electrode), ITO (bottom electrode), and CsPbBr₃ quantum dots (QDs) (as shown in Figure 4 (d)), which led to the formation and rupture of the both Br⁻ ion vacancy filaments and silver filaments.⁵⁶ This occurred as a result of light irradiation and an external bias voltage. When a positive bias was applied on the anode, Br⁻ ions migrated and accumulated around the anode, and a Br⁻ ion vacancy filament was formed. This led

to the transition from HRS to LRS. However, Ag was easily ionized into Ag^+ by external bias and Ag^+ migrated toward cathode through the active layer by applied voltage on the anode. Subsequently, Ag^+ eventually transformed to neutral Ag atoms, forming Ag filaments after capturing charge carriers. As a result, by the synergistic switching effect of valence change and electrochemical metallization, a higher ON/OFF ratio was obtained with extremely stable endurance over 5000 times, as depicted in Figure 2. 3 (e).⁵⁶

2. 3. 3. Layered structure halide perovskite based ReRAMs

As previously mentioned, the quasi-2D halide perovskite formed by inserting large organic cations into a 3D perovskite structure can also be a candidate resistive switching material. In 2017, Seo et al. reported ReRAM devices based on $\text{BA}_2\text{MA}_{n-1}\text{Pb}_n\text{I}_{3n+1}$ (BA=butylammonium) by controlling of its dimensionality.⁵⁷ Figure 2. 4(a) depicts the crystal structure of BA_2PbI_4 (2D) and 3D MAPbI_3 (3D). As shown in Figure 2. 4(b-e), as the dimensionality decreased from 3D ($n = \infty$) to 2D ($n = 1$) and the HRS current significantly decreased, which contributed to the improvement of the ON/OFF ratio from 10^2 to 10^7 .

It is considered that the low HRS current is related to a higher Schottky barrier. The high Schottky barrier at the interface between an active layer and an electrode is contributed by enlarged bandgap in the conduction band minimum and the valence band maximum caused by the change in dimensionality from 3D to 2D.

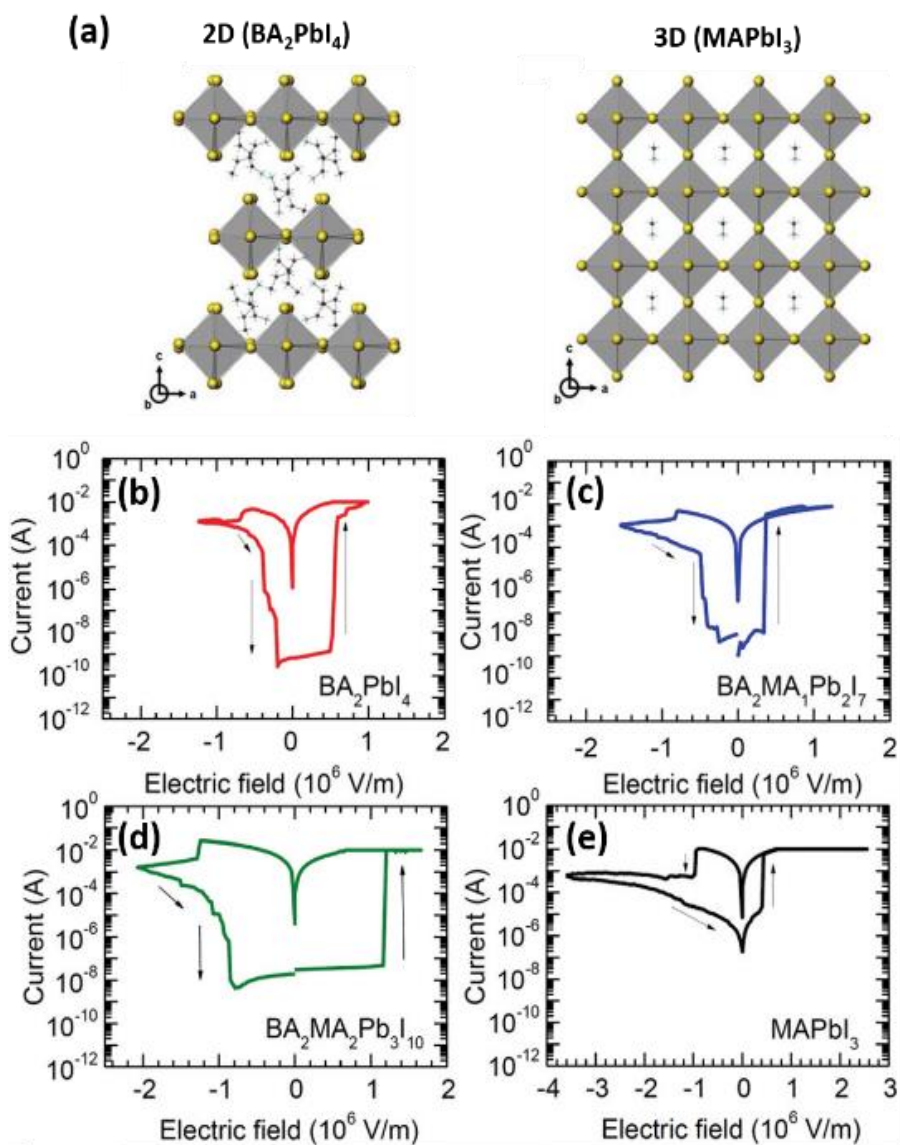


Figure 2. 4. (a) The comparison of the crystal structure of 2D (BA₂PbI₄) and 3D MAPbI₃. I–V characteristics of BA₂PbI₄ (b), BA₂MAPb₂I₇ (c), BA₂MA₂Pb₃I₁₀, (d) and MAPbI₃ (e). Reproduced with permission.⁵⁷ Copyright 2017, Royal society of Chemistry.

The increased barrier height diminishes the injected carrier density from the electrode to perovskite, which hindered the current traveling in the HRS.

In addition, its activation energy (E_a) can be another reason for the OFF current reduction. When the metallic filament is broken, a small current flow is created by thermally excited electrons hopping through shallow trap states.⁵⁹ Namely, E_a is associated with the trap state at the conduction band and the deep trap state. This is related to a high conduction band minimum and large band gap, which indicates increased E_a . Thus, a small OFF current is caused by high Schottky barrier heights and E_a , which results in a high ON/OFF ratio in the resistive switching property. The 2D layered halide perovskites have several unique properties, such as large band gaps for high ON/OFF ratio as previously mentioned, as well as a hydrophobic nature of large spacer cations to prevent water molecules from penetrating into the perovskite lattice. Even so, only a few studies on layered-halide-perovskite-based ReRAMs have been conducted.

2. 3. 4. Lead-free and new composition halide-perovskite-based ReRAMs

Halide-perovskite-based ReRAM devices have been recently emerging as a potential research topic; however, several issues still need to be resolved. In particular, the utilization of Pb must be addressed due to its toxicity. Although Pb is the most suitable for halide perovskites, non-toxic elements have to be applied in B site to achieve an environmentally friendly ReRAM device.

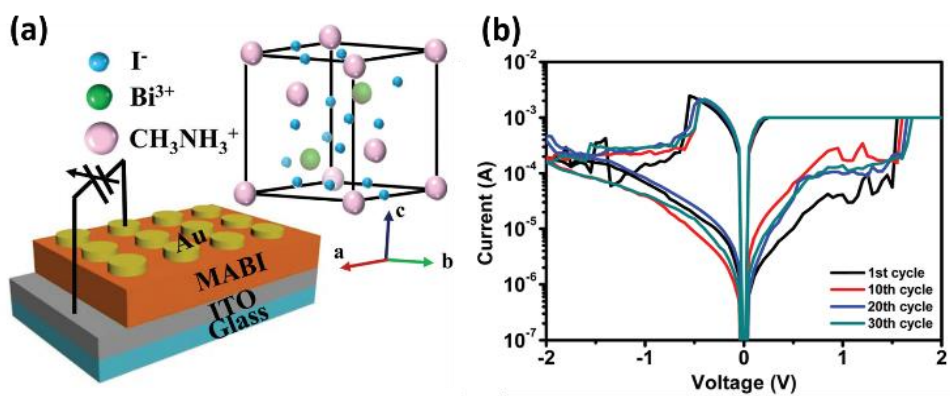


Figure 2. 5. (a) Schematic drawings of the $(\text{CH}_3\text{NH}_3)_3\text{Bi}_2\text{I}_9$ based ReRAM device. The inset shows the $(\text{CH}_3\text{NH}_3)_3\text{Bi}_2\text{I}_9$ halide perovskite structure in a unit cell. (b) The I - V sweeps of Au/MABI/ITO device. Reproduced with permission.⁶⁰ Copyright 2018, Royal society of Chemistry.

As shown in Figure 2. 5(a), Lee's group successfully fabricated lead-free ReRAM using $(\text{CH}_3\text{NH}_3)_3\text{Bi}_2\text{I}_9$, which presented approximately two orders of magnitude of ON/OFF ratio as shown in Figure 2. 5(b), an endurance of 300 cycles, a long data retention of 10^4 s, a switching speed of 100 ns, and multilevel data storage with four data levels.⁶⁰ Here, we suggest two alternatives to replace Pb.

First, a homovalent substitution of group-14 elements can be a possible component. Among them, tin (Sn^{2+}) in group-14 elements can be used for lead-free halide perovskites due to its similar ionic radius, which optically closes to Pb^{61-63} . Also, germanium (Ge^{2+}) in group-14 elements can be used because its optical and transport properties are similar to those of Pb.^{61,64} Secondly, the double perovskite is another proposed candidate to be an alternative of Pb. Its structure is $\text{A}_2\text{B}^+\text{B}^{3+}\text{X}_6$, considered heterovalent substitution, where B^+ site can have Ag, Cu or Au, and B^{3+} can be In, Sb, or Bi.^{65,66}

Finally, the new composition of halide perovskites needs to be investigated for further switching behaviour studies regarding resistive switching materials. There are several candidates for new compositions, such as $(\text{PEA})_2\text{GeI}_4$, which is a layered perovskite with using PEA and germanium,⁶⁷ $\text{Cs}_2[\text{C}(\text{NH}_2)_3]\text{Pb}_2\text{Br}_7$, which is a mixture of Cs and guanidinium,⁶⁸ $(\text{CyBMA})\text{PbBr}_4$, which contains 1,3-bis(methylaminohydrobromide) cyclohexane(CyBMABr) ligand,⁶⁹ and RbPbI_3 , which contains a rubidium cation (Ru^+), compared to slightly smaller than cesium cation.⁷⁰ These types of new compositions of halide perovskites has been rarely

studied; however, their research works are sufficient to allow halide-perovskite-based ReRAM to show the most potential for future memory devices.

2. 4. Conclusion

The ReRAM device is being spotlighted as a next-generation alternative to conventional memory devices. Although vast studies on switching materials have been reported, ReRAM devices based on halide perovskites have not been reported much because they have only recently emerged as viable materials. Currently, many groups have started to research halide-perovskite-based ReRAM devices owing to their potential. In this part, recent advancements in ReRAM devices are not only categorized as classified halide perovskite materials but also introduced with suggestions about new materials that can be applied as a switching layer. With regard to commercialization, there are several challenges and issues that must be resolved, such as the enhancement of resistive switching properties and the stability of the switching materials. In addition, because of the rapidly growing interest in wearable and portable devices, increased flexibility of the device is required to fulfill customer demands.

Although formal research on halide-perovskite-based ReRAM devices has only just started, we undoubtedly believe that it will be a highly influential device with amazing advances in the future market and will serve as a stepping stone for the development of a resistive switching memory field.

In addition, this topical review will encourage researchers to investigate halide-perovskite-based ReRAM devices with useful insights, overcome its challenges, and give a direction to offer promising opportunities.

2. 5. Reference

- 1 S. A. Veldhuis, P. P. Boix, N. Yantara, M. Li, T. C. Sum, N. Mathews and S. G. Mhaisalkar, *Adv. Mater.*, 2016, **28**, 6804–6834.
- 2 H. Kim, G. Veerappan and J. H. Park, *Electrochim. Acta*, 2014, **137**, 164–168.
- 3 H. Kim, G. Veerappan, D. H. Wang and J. H. Park, *Electrochim. Acta*, 2016, **187**, 218–223.
- 4 R. Corkish, D. S. P. Chan and M. A. Green, *J. Appl. Phys.*, 1996, **79**, 195–203.
- 5 M. A. Green, A. Ho-Baillie and H. J. Snaith, *Nat. Photonics*, 2014, **8**, 506–514.
- 6 A. R. B. M. Yusoff and M. K. Nazeeruddin, *J. Phys. Chem. Lett.*, 2016, **7**, 851–866.
- 7 C. C. Stoumpos, C. D. Malliakas and M. G. Kanatzidis, *Inorg. Chem.*, 2013, **52**, 9019–9038.
- 8 J. H. Noh, S. H. Im, J. H. Heo, T. N. Mandal and S. Il Seok, *Nano Lett.*, 2013, **13**, 1764–1769.
- 9 D.-H. Kwon, K. M. Kim, J. H. Jang, J. M. Jeon, M. H. Lee, G. H. Kim, X.-S. Li, G.-S. Park, B. Lee, S. Han, M. Kim and C. S. Hwang, *Nat. Nanotechnol.*, 2010, **5**, 148–153.

- 10 M.-J. Lee, C. B. Lee, D. Lee, S. R. Lee, M. Chang, J. H. Hur, Y.-B. Kim, C.-J. Kim, D. H. Seo, S. Seo, U.-I. Chung, I.-K. Yoo and K. Kim, *Nat. Mater.*, 2011, **10**, 625–630.
- 11 R. Yasuhara, T. Yamamoto, I. Ohkubo, H. Kumigashira and M. Oshima, *Appl. Phys. Lett.*, 2010, **97**, 132111.
- 12 A. Q. Jiang, C. Wang, K. J. Jin, X. B. Liu, J. F. Scott, C. S. Hwang, T. A. Tang, H. Bin Lu and G. Z. Yang, *Adv. Mater.*, 2011, **23**, 1277–1281.
- 13 Y. Ren, V. Milo, Z. Wang, H. Xu, D. Ielmini, X. Zhao and Y. Liu, *Adv. Theory Simulations*, 2018, **1**, 1700035.
- 14 H. Akinaga and H. Shima, *Proc. IEEE*, 2010, **98**, 2237–2251.
- 15 A. Prakash, D. Jana and S. Maikap, *Nanoscale Res. Lett.*, 2013, **8**, 418.
- 16 S. Menzel, *J. Comput. Electron.*, 2017, **16**, 1017–1037.
- 17 C. Baeumer, C. Schmitz, A. Marchewka, D. N. Mueller, R. Valenta, J. Hackl, N. Raab, S. P. Rogers, M. I. Khan, S. Nemsak, M. Shim, S. Menzel, C. M. Schneider, R. Waser and R. Dittmann, *Nat. Commun.*, 2016, **7**, 12398.
- 18 R. Waser and M. Aono, *Nat. Mater.*, 2007, **6**, 833–840.
- 19 R. Waser, R. Dittmann, G. Staikov and K. Szot, *Adv. Mater.*, 2009, **21**, 2632–2663.
- 20 D. Ielmini and R. Waser, *Resistive Switching*, Wiley-VCH Verlag GmbH & Co. KGaA, Weinheim, Germany, 2016.
- 21 A. Sawa, *Mater. Today*, 2008, **11**, 28–36.

- 22 J. R. Jameson, N. Gilbert, F. Koushan, J. Saenz, J. Wang, S. Hollmer and M. N. Kozicki, *Appl. Phys. Lett.*, 2011, **99**, 63506.
- 23 S. Menzel, S. Tappertzhofen, R. Waser and I. Valov, *Phys. Chem. Chem. Phys.*, 2013, **15**, 6945.
- 24 A. Marchewka, B. Roesgen, K. Skaja, H. Du, C.-L. Jia, J. Mayer, V. Rana, R. Waser and S. Menzel, *Adv. Electron. Mater.*, 2016, **2**, 1500233.
- 25 S. Larentis, F. Nardi, S. Balatti, D. C. Gilmer and D. Ielmini, *IEEE Trans. Electron Devices*, 2012, **59**, 2468–2475.
- 26 I. Valov, *ChemElectroChem*, 2014, **1**, 26–36.
- 27 K. M. Kim, D. S. Jeong and C. S. Hwang, *Nanotechnology*, 2011, **22**, 254002.
- 28 Y. Shan, Z. Lyu, X. Guan, A. Younis, G. Yuan, J. Wang, S. Li and T. Wu, *Phys. Chem. Chem. Phys.*, 2018, **20**, 23837–23846.
- 29 E. Yoo, M. Lyu, J.-H. Yun, C. Kang, Y. Choi and L. Wang, *J. Mater. Chem. C*, 2016, **4**, 7824–7830.
- 30 M. Ghoneim and M. Hussain, *Electronics*, 2015, **4**, 424–479.
- 31 E. J. Yoo, M. Lyu, J.-H. Yun, C. J. Kang, Y. J. Choi and L. Wang, *Adv. Mater.*, 2015, **27**, 6170–6175.
- 32 S. Menzel, U. Böttger, M. Wimmer and M. Salinga, *Adv. Funct. Mater.*, 2015, **25**, 6306–6325.
- 33 G. W. Burr, R. S. Shenoy, K. Virwani, P. Narayanan, A. Padilla, B. Kurdi and H. Hwang, *J. Vac. Sci. Technol. B, Nanotechnol. Microelectron. Mater. Process. Meas. Phenom.*, 2014, **32**, 40802.

- 34 B. Hwang and J.-S. Lee, *Adv. Mater.*, 2017, **29**, 1701048.
- 35 A. Fantini, G. Gorine, R. Degraeve, L. Goux, C. Y. Chen, A. Redolfi, S. Clima, A. Cabrini, G. Torelli and M. Jurczak, in *2015 IEEE International Electron Devices Meeting (IEDM)*, IEEE, 2015, vol. 2016–Febru, p. 7.5.1-7.5.4.
- 36 A. Younis, D. Chu and S. Li, *Sci. Rep.*, 2015, **5**, 13599.
- 37 J. Choi, J. S. Han, K. Hong, S. Y. Kim and H. W. Jang, *Adv. Mater.*, 2018, **30**, 1704002.
- 38 W. Tress, N. Marinova, T. Moehl, S. M. Zakeeruddin, M. K. Nazeeruddin and M. Grätzel, *Energy Environ. Sci.*, 2015, **8**, 995–1004.
- 39 Z. Xiao, Y. Yuan, Y. Shao, Q. Wang, Q. Dong, C. Bi, P. Sharma, A. Gruverman and J. Huang, *Nat. Mater.*, 2015, **14**, 193–198.
- 40 C. Gu and J.-S. Lee, *ACS Nano*, 2016, **10**, 5413–5418.
- 41 A. Buin, P. Pietsch, J. Xu, O. Voznyy, A. H. Ip, R. Comin and E. H. Sargent, *Nano Lett.*, 2014, **14**, 6281–6286.
- 42 E. L. Unger, E. T. Hoke, C. D. Bailie, W. H. Nguyen, A. R. Bowring, T. Heumüller, M. G. Christoforo and M. D. McGehee, *Energy Environ. Sci.*, 2014, **7**, 3690–3698.
- 43 H.-S. Kim, S. K. Kim, B. J. Kim, K.-S. Shin, M. K. Gupta, H. S. Jung, S.-W. Kim and N.-G. Park, *J. Phys. Chem. Lett.*, 2015, **6**, 1729–1735.
- 44 C. Eames, J. M. Frost, P. R. F. Barnes, B. C. O’Regan, A. Walsh and M. S. Islam, *Nat. Commun.*, 2015, **6**, 7497.

- 45 D. H. Song, M. H. Jang, M. H. Lee, J. H. Heo, J. K. Park, S.-J. Sung, D.-H. Kim, K.-H. Hong and S. H. Im, *J. Phys. D. Appl. Phys.*, 2016, **49**, 473001.
- 46 J. H. Heo, D. H. Shin, S. H. Moon, M. H. Lee, D. H. Kim, S. H. Oh, W. Jo and S. H. Im, *Sci. Rep.*, 2017, **7**, 16586.
- 47 J. Choi, S. Park, J. Lee, K. Hong, D.-H. Kim, C. W. Moon, G. Do Park, J. Suh, J. Hwang, S. Y. Kim, H. S. Jung, N.-G. Park, S. Han, K. T. Nam and H. W. Jang, *Adv. Mater.*, 2016, **28**, 6562–6567.
- 48 K. M. Kim, S. R. Lee, S. Kim, M. Chang and C. S. Hwang, *Adv. Funct. Mater.*, 2015, **25**, 1527–1534.
- 49 W. Nie, J.-C. Blancon, A. J. Neukirch, K. Appavoo, H. Tsai, M. Chhowalla, M. A. Alam, M. Y. Sfeir, C. Katan, J. Even, S. Tretiak, J. J. Crochet, G. Gupta and A. D. Mohite, *Nat. Commun.*, 2016, **7**, 11574.
- 50 G. Divitini, S. Cacovich, F. Matteocci, L. Cinà, A. Di Carlo and C. Ducati, *Nat. Energy*, 2016, **1**, 15012.
- 51 B. Conings, J. Drijkoningen, N. Gauquelin, A. Babayigit, J. D’Haen, L. D’Olieslaeger, A. Ethirajan, J. Verbeeck, J. Manca, E. Mosconi, F. De Angelis and H.-G. Boyen, *Adv. Energy Mater.*, 2015, **5**, 1500477.
- 52 A. Kojima, K. Teshima, Y. Shirai and T. Miyasaka, *J. Am. Chem. Soc.*, 2009, **131**, 6050–6051.
- 53 M. Grätzel, *Nat. Mater.*, 2014, **13**, 838–842.

- 54 R. J. Sutton, G. E. Eperon, L. Miranda, E. S. Parrott, B. A. Kamino, J. B. Patel, M. T. Hörlantner, M. B. Johnston, A. A. Haghighirad, D. T. Moore and H. J. Snaith, *Adv. Energy Mater.*, 2016, **6**, 1502458.
- 55 J. S. Han, Q. Van Le, J. Choi, K. Hong, C. W. Moon, T. L. Kim, H. Kim, S. Y. Kim and H. W. Jang, *Adv. Funct. Mater.*, 2018, **28**, 1705783.
- 56 Y. Wang, Z. Lv, Q. Liao, H. Shan, J. Chen, Y. Zhou, L. Zhou, X. Chen, V. A. L. Roy, Z. Wang, Z. Xu, Y.-J. Zeng and S.-T. Han, *Adv. Mater.*, 2018, **30**, 1800327.
- 57 J.-Y. Seo, J. Choi, H.-S. Kim, J. Kim, J.-M. Yang, C. Cuhadar, J. S. Han, S.-J. Kim, D. Lee, H. W. Jang and N.-G. Park, *Nanoscale*, 2017, **9**, 15278–15285.
- 58 K. Jung, H. Seo, Y. Kim, H. Im, J. Hong, J.-W. Park and J.-K. Lee, *Appl. Phys. Lett.*, 2007, **90**, 52104.
- 59 W. Zhu, T. P. Chen, Y. Liu and S. Fung, *J. Appl. Phys.*, 2012, **112**, 63706.
- 60 B. Hwang and J.-S. Lee, *Nanoscale*, 2018, **10**, 8578–8584.
- 61 S. Chatterjee and A. J. Pal, *J. Mater. Chem. A*, 2018, **6**, 3793–3823.
- 62 J. Qian, B. Xu and W. Tian, *Org. Electron.*, 2016, **37**, 61–73.
- 63 Y. M. Lee, J. Park, B. D. Yu, S. Hong, M.-C. Jung and M. Nakamura, *J. Phys. Chem. Lett.*, 2018, **9**, 2293–2297.
- 64 P.-P. Sun, Q.-S. Li, L.-N. Yang and Z.-S. Li, *Nanoscale*, 2016, **8**, 1503–1512.
- 65 F. Giustino and H. J. Snaith, *ACS Energy Lett.*, 2016, **1**, 1233–1240.

- 66 G. Volonakis, M. R. Filip, A. A. Haghighirad, N. Sakai, B. Wenger, H. J. Snaith and F. Giustino, *J. Phys. Chem. Lett.*, 2016, **7**, 1254–1259.
- 67 P. Cheng, T. Wu, J. Zhang, Y. Li, J. Liu, L. Jiang, X. Mao, R.-F. Lu, W.-Q. Deng and K. Han, *J. Phys. Chem. Lett.*, 2017, **8**, 4402–4406.
- 68 O. Nazarenko, M. R. Kotyrba, M. Wörle, E. Cuervo-Reyes, S. Yakunin and M. V. Kovalenko, *Inorg. Chem.*, 2017, **56**, 11552–11564.
- 69 I. Neogi, A. Bruno, D. Bahulayan, T. W. Goh, B. Ghosh, R. Ganguly, D. Cortecchia, T. C. Sum, C. Soci, N. Mathews and S. G. Mhaisalkar, *ChemSusChem*, 2017, **10**, 3765–3772.
- 70 M. Saliba, T. Matsui, K. Domanski, J.-Y. Seo, A. Ummadisingu, S. M. Zakeeruddin, J.-P. Correa-Baena, W. R. Tress, A. Abate, A. Hagfeldt and M. Gratzel, *Science (80-.)*, 2016, **354**, 206–209.

Chapter 3

Resistive Switching Devices based on Quasi-2D Halide Perovskites for High ON/OFF Ratios

3. 1. Introduction

Photovoltaic devices are recognized as prospective energy sources¹⁻⁸. As light absorbers, halide perovskites have had significant impact on solar cell research owing to their remarkable photovoltaic properties, such as long charge diffusion length and low exciton binding energies⁹⁻¹⁶. In particular, the current-voltage ($I-V$) hysteresis of halide perovskites broadens their applications to electronic devices beyond photovoltaics, such as field-effect transistors, resistive-switching memory, and artificial synapses¹⁷⁻¹⁹. The defects that cause sweep-dependent hysteresis migrate in the halide perovskite layer, causing a switch in the current direction upon application of a weak electric field²⁰.

Generally, halide perovskites, which are 3D structured compounds with the chemical formula ABX_3 , consist of monovalent cations in the A-site and divalent cations in the B-site, and halide anions in the X-site²¹. 3D halide perovskites such as $MAPbI_3$ ($MA = CH_3NH_3$) or $CsPbI_3$ have been mostly studied for ReRAM devices, having ON/OFF ratios of the order of 10^6 orders with multi-level resistive switching behavior and low operating voltage^{22,23}.

ReRAM devices based on halide perovskites have recently received attention as a potential research topic; however, some issues need to be resolved. Compared with conventional ReRAM devices based on metal oxides²⁴⁻²⁶, 3D halide perovskite memory devices display low stability in humid and ambient atmosphere, leading to degradation of the switching characteristics of the memory devices. More importantly, the ON/OFF ratio should be higher than 10^{10} to be commercialized,

because the resistances of bit and selector lines are considered in terms of high density layer of the memory array.

To address these issues, quasi-2D halide perovskites have been considered as a means of improving the ON/OFF ratio and preventing device degradation in air^{27,28}. Quasi-2D halide perovskites have the general formula: $(RNH_3)_2A_{n-1}B_nX_{3n+1}$ ($n = 1, 2, 3, \dots$), where RNH_3 is a large organic cation such as a large aliphatic or aromatic alkylammonium cation²⁹⁻³². Thus, as the n values decreases, the dimensionality of halide perovskites changes from 3D to quasi-2D and 2D structures. Quasi-2D halide perovskites, which are formed by introducing large organic cations into 3D perovskites, have a wider bandgap³³⁻³⁵, which makes the Schottky barrier at the interface top electrode much higher. This in turn lowers the high resistance state (HRS) current, which results in an increase in the ON/OFF ratio. Further, the large organic cation between the quasi-2D perovskite layers prevents the device from breaking down because of the hydrophobicity of the alkyl amines³⁶⁻³⁹. Recently, ReRAM devices were reported with ON/OFF ratios ranging from 10^5-10^7 , still too low to show commercial promise^{40,41}.

In this study, $(PEA)_2Cs_3Pb_4I_{13}$ (PEA = Phenethylammonium) and $CsPbI_3$ are employed as the resistive switching elements in a ReRAM device to compare the dependence of the switching behavior on the 3D and quasi-2D halide perovskites. We successfully fabricate a $(PEA)_2Cs_3Pb_4I_{13}$ ReRAM device with the $Ag/(PEA)_2Cs_3Pb_4I_{13}/Pt(\text{platinum})/Ti/SiO_2/Si$ structure, where the perovskite resistive switching layer is synthesized on a Pt-coated silicon substrate by solution

processing at low temperature. The devices exhibit bipolar resistive switching behavior and ultralow operating voltages. Furthermore, the ON/OFF ratios ($> 10^9$) of the $(\text{PEA})_2\text{Cs}_3\text{Pb}_4\text{I}_{13}$ ReRAM devices are noticeably higher than those of the CsPbI_3 device, with long-term stability under ambient conditions. This study provides an opportunity to investigate the effect of the dimensionality of halide perovskites on resistive switching of devices for use in next-generation high-performance nonvolatile memory.

3. 2. Experimental Section

Materials

Lead(II) iodide (99.9985%) and hydroiodic acid (57% in aqueous solution, stabilized with 1.5% hydrophosphorous acid) were provided by Alfa Aesar. Phenylethyl amine (>99%), cesium iodide (99.99%), poly(methyl methacrylate), chlorobenzene (anhydrous, 99.8%), and *N,N*-dimethylformamide (anhydrous, 99.8%) were purchased from Sigma Aldrich. All the materials were used without any further purification.

Synthesis of PEAI

Phenylethylamine (80 mmol) was dissolved in 10 mL of ethanol and placed in an ice bath. HI (20 mL) was then slowly added to the flask and kept for 20 min under vigorous stirring. The white powder (PEAI) was collected using a rotary evaporator and washed thrice with diethyl ether. Finally, the product was dried under vacuum at 50 °C for 1 day before use.

Fabrication of memory

Different dimensional perovskite ($\text{PEA}_2\text{Cs}_{n-1}\text{PbI}_{3n+1}$) precursors were prepared by mixing a stoichiometric quantity of PEAI, CsI, and PbI_2 in DMF with a concentration

of 40 wt%, followed by heating for 12 h. A small amount of HI was added to the solution to increase the solubility of PEAI. A uniform film was obtained by spin-coating the precursor on Pt/Ti/SiO₂/Si substrates at a speed of 4000 rpm, and heating at 150 °C for 5 min. The PMMA solution (5 mg mL⁻¹) was spin-coated to protect the perovskite film from moisture. After deposition of PMMA, the films were further heated at 100 °C for 5 min. To complete the devices, Ag electrodes (50 μm × 50 μm) were deposited by e-beam evaporation under 1 × 10⁻⁶ Torr at room temperature through a shadow mask.

Characterization

The surface and cross-section of the perovskite films were imaged using a field-emission scanning electron microscope (ZEISS MERLIN COMPACT). The morphology of the perovskite films was analyzed using atomic force microscopy (Park System XE100). The X-ray diffraction patterns were recorded using an X-ray diffractometer (BRUKER MILLER Co., D8-Advance) with Cu- α radiation. The electrical properties of the memory units were characterized by using an Agilent 4156C semiconductor analyzer in the direct current voltage sweeping mode and alternating voltage pulse mode in a vacuum chamber (6 × 10⁻² Torr).

3. 3. Results and Discussion

Figure 3. 1 presents a schematic illustration of the device structure and the resistive switching materials, CsPbI₃ and (PEA)₂Cs₃Pb₄I₁₃. Vertical-stacks of the Ag top electrode/CsPbI₃ or (PEA)₂Cs₃Pb₄I₁₃/Pt bottom electrode/Ti/SiO₂/Si structures were fabricated, respectively. For the low-temperature all-solution process, CsPbI₃ and (PEA)₂Cs₃Pb₄I₁₃ films were successfully synthesized by the spin-coating method and by the thermal evaporation method using a dot-patterned shadow mask; the Ag top electrodes were formed on the switching layers.

Compared to CsPbI₃, a 3D halide perovskite, the two organic PEA cation layers that are stacked between the inorganic layers can increase the bandgap. Although the organic PEA cations do not influence the electronic states around the band edge, the steric hindrance and other structural effects caused by the organic PEA cations bring about structural changes in the halide perovskite frameworks, which indirectly influences the increase in the bandgap. Notably, the bandgap increase has a significant influence on the switching performance⁴².

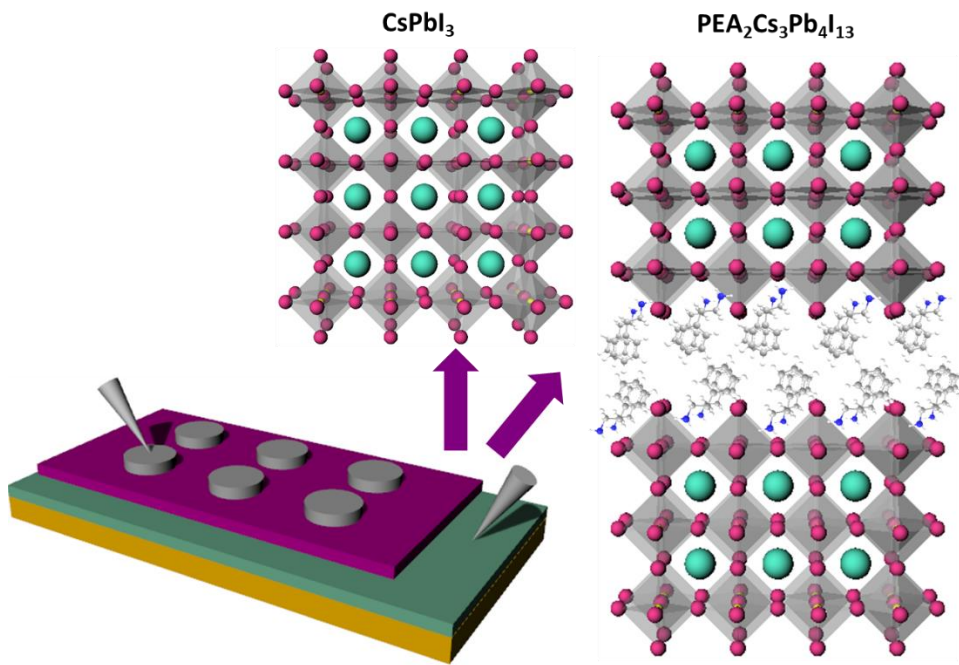


Figure 3. 1. Schematic illustration of resistive memory device structure and resistive switching materials, CsPbI_3 and $(\text{PEA})_2\text{Cs}_3\text{Pb}_4\text{I}_{13}$.

Figures 3. 2(a) and 3. 2(b) present the scanning electron microscopy (SEM) images of CsPbI₃ and (PEA)₂Cs₃Pb₄I₁₃ perovskite layers synthesized on the Pt-coated silicon substrates. For both samples, the thickness was about 300–350 nm, with good film quality and high film coverage. To achieve a smooth surface, the Pt-coated silicon substrates were subjected to UV ozone cleaning before coating with the perovskite films.

As shown in Figure 3. 2(c, d), the surface of both perovskite layers was evaluated by atomic force microscopy (AFM) with a scan size of 5 μm × 5 μm. Ultra-low roughness was obtained for the (PEA)₂Cs₃Pb₄I₁₃ film, with a root mean square (RMS) roughness of 3.0 nm, which is much lower than that of the CsPbI₃ film (15.0 nm). It is suspected that the addition of PEAI to the precursor solution impedes the growth of the perovskite crystal due to the strong hydrogen bond between the hydrogen atom of PEAI and the halide atom in PbI. Thus, PEAI addition to form (PEA)₂Cs₃Pb₄I₁₃, a quasi-2D halide perovskite, dramatically improved the film uniformity.^{43,44}

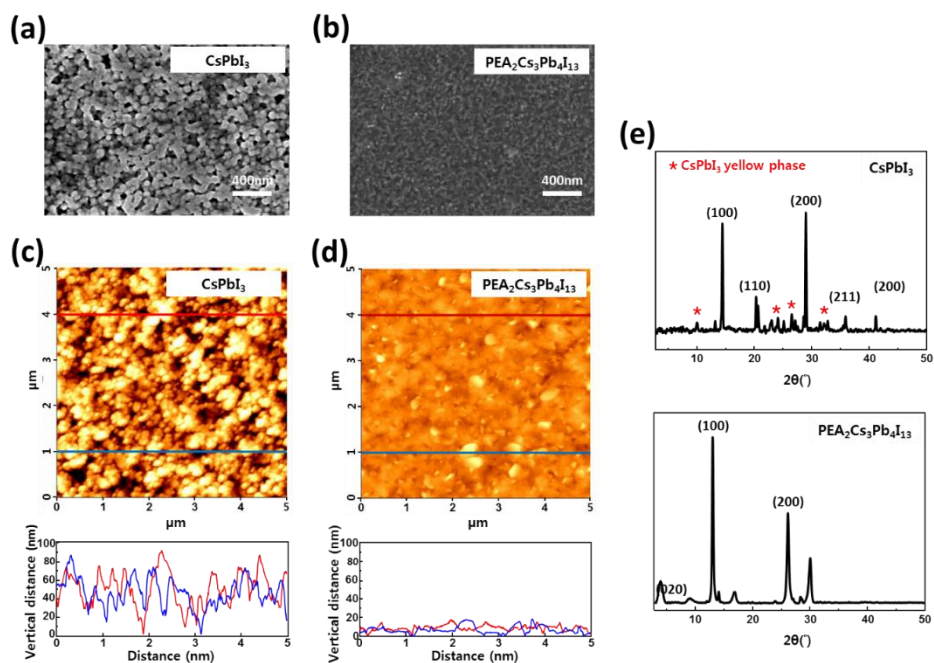


Figure 3. 2. Properties of halide perovskite films. (a, b) Top-view SEM images of the CsPbI₃ (a) and (PEA)₂Cs₃Pb₄I₁₃ (b) perovskite film. (c, d) AFM images of the CsPbI₃ (c) (RMS = 15.0 nm) and the (PEA)₂Cs₃Pb₄I₁₃ (d) perovskite film (RMS = 15.0 nm). The tips move 5 μm through the red and blue line to measure the roughness. (e) X-ray diffraction pattern of CsPbI₃ and (PEA)₂Cs₃Pb₄I₁₃ thin films on glass substrate.

X-ray diffraction (XRD) measurement was conducted to verify the accurate phase of the 3D perovskite (CsPbI_3 black phase) and quasi-2D perovskite ($(\text{PEA})_2\text{Cs}_3\text{Pb}_4\text{I}_{13}$). As shown in Figure 3. 2(e), the XRD pattern of the CsPbI_3 sample shows sharp peaks at (100) and (200), indicating that the obtained perovskite film is highly oriented. A shoulder appeared next to the (110) peak, providing evidence of strain in the crystal, which allows crystallization of CsPbI_3 in the cubic phase.⁴⁵ Nevertheless, peaks of the yellow phase were also observed due to the metastable nature of cubic CsPbI_3 . Upon incorporating PEAI into CsPbI_3 to obtain the quasi-2D perovskite, a low-angle diffraction peak appeared, which can be attributed to the typical reflections from the layer structure.⁴⁶ No XRD peaks related to yellow-phase CsPbI_3 were observed for the quasi-2D perovskite sample. This indicates that the addition of PEAI to CsPbI_3 not only improves the morphology, but also considerably boosts the stability of the perovskite film by inhibiting the transformation from the black to yellow phase of CsPbI_3 .

To compare the switching characteristics of the CsPbI_3 - and $(\text{PEA})_2\text{Cs}_3\text{Pb}_4\text{I}_{13}$ -based memory devices, the I - V characteristics of both devices were measured under direct current voltage sweep. Figure 3. 3 displays the typical current-voltage curves of the $\text{Ag}/\text{CsPbI}_3/\text{Pt}$ (a) and $\text{Ag}/(\text{PEA})_2\text{Cs}_3\text{Pb}_4\text{I}_{13}/\text{Pt}$ (b) devices, where the voltage was applied to the top Ag electrode and the Pt bottom electrode was grounded. Both devices displayed bipolar resistive switching, which indicates that ON/OFF switching occurred at opposite polarities.

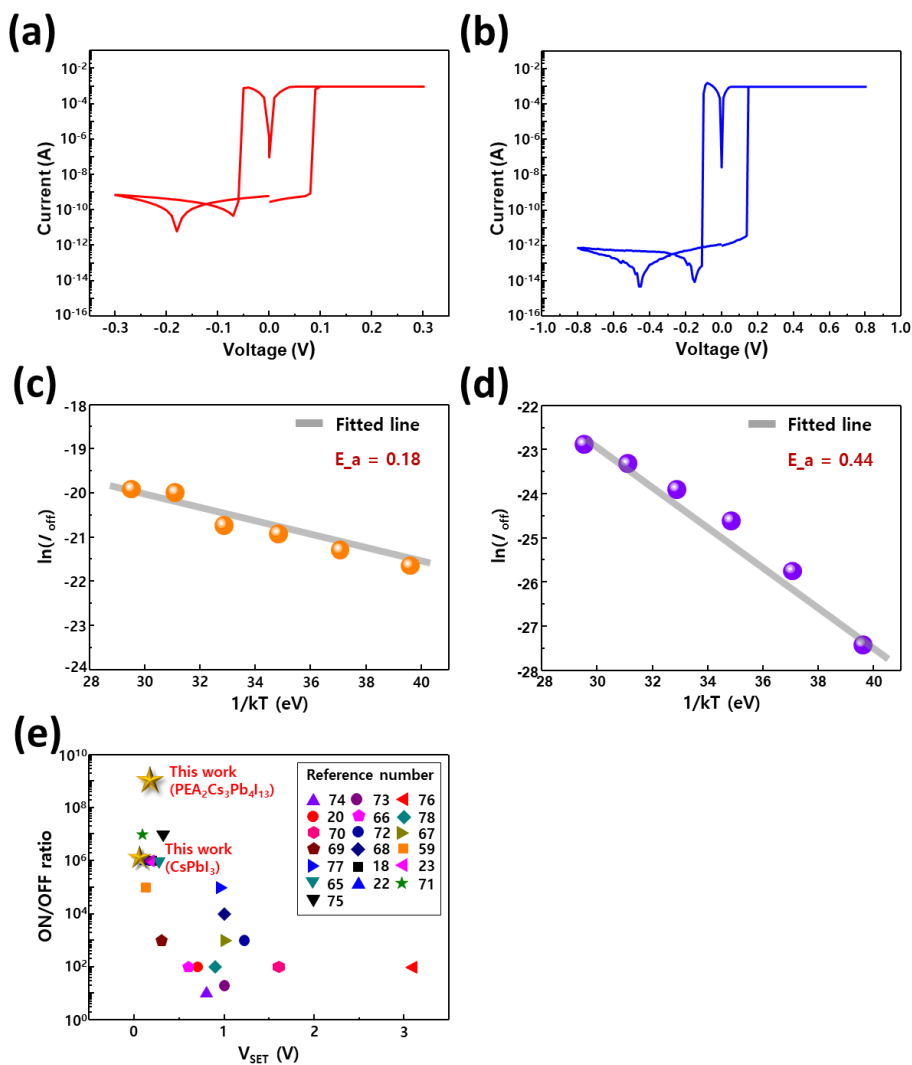


Figure 3. Typical current–voltage curves of Ag/CsPbI₃/Pt (a) and Ag/(PEA)₂Cs₃Pb₄I₁₃/Pt (b) devices. Temperature-dependent OFF currents of Ag/CsPbI₃/Pt (c) and Ag/(PEA)₂Cs₃Pb₄I₁₃/Pt (d) devices; Arrhenius equation was used to deduce E_a . (e) Comparison of the ON/OFF ratio with various halide perovskites-based ReRAM devices including the CsPbI₃ and ((PEA)₂Cs₃Pb₄I₁₃) based cells.

Given that the ON/OFF resistive switching operation is explained by the SET and RESET processes for these halide perovskite memory devices, the SET process, which refers to the switching from a high resistance state (HRS; OFF state) to a low resistance state (LRS; ON state) at a certain positive voltage, showed an abrupt increase. In these memory devices, the abrupt increase in the current during the SET process and the sustained LRS support the formation of conducting filaments with a compliance current (CC) of 10^{-3} A. Then, the LRS changed to a HRS when a negative voltage was applied to these devices, which indicates rupture of the conducting filaments with a CC of 10^{-2} A. Notably, the ON/OFF ratio for the $(\text{PEA})_2\text{Cs}_3\text{Pb}_4\text{I}_{13}$ -based devices was as high as a $\sim 10^9$, whereas that of the CsPbI_3 -based devices was much lower (by approximately 10^6). The high ON/OFF ratio of the $(\text{PEA})_2\text{Cs}_3\text{Pb}_4\text{I}_{13}$ -based devices can be explained by the Schottky barrier height.

By changing the dimensionality from 3D for CsPbI_3 to quasi-2D for $(\text{PEA})_2\text{Cs}_3\text{Pb}_4\text{I}_{13}$, the bandgap is widened.³³⁻³⁵ As the bandgap increases, the Schottky barrier height, which corresponds to the electron flow from the top electrode to the bottom electrode, increases at the interface between the halide perovskite switching layer and Ag top electrode. This means that the increased barrier height caused a reduction of the injected carrier density from the electrode to the perovskite switching layer. As a result, the HRS current decreased, leading to a high ON/OFF ratio.

The electrical thermal activation energy (E_a) may be another factor influencing the HRS current reduction. Figures 3. 3(c) and (d) present plots of the HRS current

versus the inverse temperature at 0.02 V; E_a for carrier migration in the switching layer in the HRS was deduced from the Arrhenius equation. From the linear fitting slope of each curve, the activation energy was estimated using the Arrhenius equation (presented as Equation (1)):

$$\ln I_{\text{off}}(T) = \ln I_0 - \frac{E_a}{kT} \quad (1),$$

where I_{off} is the current in the HRS, I_0 is a constant, E_a is the activation energy, k is the Boltzmann constant, and T is absolute temperature.⁴⁷ The distribution of E_a for the CsPbI₃ and (PEA)₂Cs₃Pb₄I₁₃ memory devices extracted from this Arrhenius plot was 0.18 and 0.44 eV, respectively.

When the conducting filament is broken in the HRS, a small current flows through trap states by hopping of thermally excited electrons.^{48,49} The trap state, which is a donor level in the conduction band, is associated with E_a . Compared with the 3D halide perovskite (CsPbI₃), the quasi-2D halide perovskite ((PEA)₂Cs₃Pb₄I₁₃) has a larger bandgap and higher conduction band minimum, leading to deeper trap states. The deep trap states cause the E_a to increase. Thus, the HRS current decreased.

Table 3. 1. Comparison of various halide perovskites -based ReRAM devices.

Device structure	SET voltage [V_{set}]	ON/OFF ratio	Ref.
Au/MAPbI _{3-x} Cl _x /FTO	0.8	10	65
Au/MAPbCl _x I _{3-x} /TiO ₂ /Ti	1	20	66
W/Oleic acid-MAPbI ₃ /FTO	3.1	10 ²	67
Au/MAPbI ₃ /ITO	0.7	10 ²	20
Al/CsPbBr ₃ /PEDOT:PSS/ITO	-0.6	10 ²	68
Au/ZnO/MAPbI ₃ /ITO	0.9	10 ²	69
Au/MA ₃ Bi ₂ I ₉ /ITO	1.6	10 ²	70
Ag/PMMA/MAPbI ₃ /PMMA/ITO	1.2	10 ³	71
Ag/PMMA/MAPbBr ₃ :PMMA/PMMA/ITO	1	10 ³	72
Au/Cs ₃ Bi ₂ I ₉ /ITO	0.3	10 ³	73
Au/MAPbI ₃ /Pt	1	10 ⁴	74
Ag/PMMA/CsSnI ₃ /Pt	0.13	10 ⁵	59
Ni/ZnO/CsPbBr ₃ /FTO	-0.95	10 ⁵	75
Ag/MAPbI ₃ /Pt	0.2	10 ⁶	18
Ag/PMMA/CsPbI ₃ /Pt	0.18	10 ⁶	23
Ag/PMMA/Rb _{0.52} MA _{0.48} PbI ₃ /Pt	0.25	10 ⁶	76
Ag/MAPbI ₃ /Pt	0.13	10 ⁶	22

Ag/CsPbI ₃ /Pt	0.1	10 ⁶	This work
Au/Rb ₃ Bi ₂ I ₉ (Cs ₃ Bi ₂ I ₉)/Pt	0.09(0.1)	10 ⁷	⁷⁷
Au/MAPbI ₃ /Au	0.32	10 ⁷	⁷⁸
Ag/PEA ₂ Cs ₃ Pb ₄ I ₁₃ /Pt	0.18	10 ⁹	This work

Therefore, the fact that the Schottky barrier height and the activation energy of quasi-2D $(\text{PEA})_2\text{Cs}_3\text{Pb}_4\text{I}_{13}$ are higher than those of 3D perovskites may account for the high ON/OFF ratio of the $(\text{PEA})_2\text{Cs}_3\text{Pb}_4\text{I}_{13}$ - based memory device, originating from the low HRS current.

To compare the superior resistive switching properties of the $(\text{PEA})_2\text{Cs}_3\text{Pb}_4\text{I}_{13}$ based memory device with representative research works on halide perovskites based ReRAMs, the values of the ON/OFF ratios with SET voltages are exhibited, as shown in Table 3. 1. Also, the ON/OFF ratios versus SET voltages are plotted in Figure 3. 3(e).

Figure 3. 4 shows the detailed resistive switching performance of the $(\text{PEA})_2\text{Cs}_3\text{Pb}_4\text{I}_{13}$ -based memory device. As shown in Figure 3. 4(a), a series of five sweeps was performed in DC sweep mode at $0\text{ V} \rightarrow +0.8\text{ V} \rightarrow 0\text{ V} \rightarrow -0.8\text{ V} \rightarrow 0\text{ V}$ with a semiconductor parameter analyzer to confirm hysteresis in the I - V profile of the device. In the initial DC sweep, an electroforming process referred as a kind of “soft breakdown” was needed to achieve stable resistive switching properties,⁵⁰ which is analogous to that of general resistive switching memory devices based on electrochemical metallization (ECM). In ECM, the active top electrode is dissolved by oxidation, after which the metal cations form a conducting filament passing through the switching layer.⁵¹

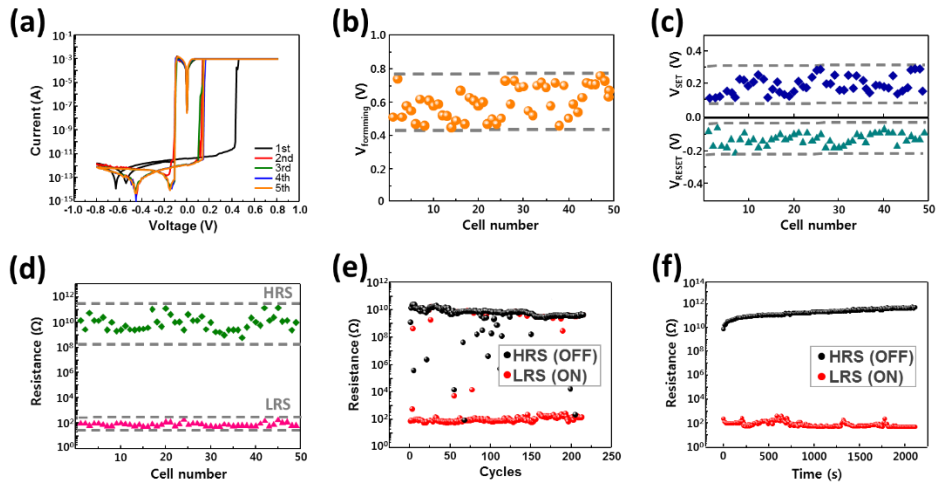


Figure 3. 4. Resistive switching performance of $(\text{PEA})_2\text{Cs}_3\text{Pb}_4\text{I}_{13}$ -based memory device. (a) Series I - V characteristics of the $\text{Ag}/(\text{PEA})_2\text{Cs}_3\text{Pb}_4\text{I}_{13}/\text{Pt}$ cells. (b, c) Statistically analyzed forming (b), SET, and RESET (c) voltage distributions of 50 different $\text{Ag}/(\text{PEA})_2\text{Cs}_3\text{Pb}_4\text{I}_{13}/\text{Pt}$ cells. (d) High- and low-resistance states of 50 different $\text{Ag}/(\text{PEA})_2\text{Cs}_3\text{Pb}_4\text{I}_{13}/\text{Pt}$ cells. (e) Endurance characteristics for $(\text{PEA})_2\text{Cs}_3\text{Pb}_4\text{I}_{13}$ memory device. (f) Retention property of the ON and OFF states.

In the $(\text{PEA})_2\text{Cs}_3\text{Pb}_4\text{I}_{13}$ -based memory device, electroforming occurred abruptly at a voltage of +0.40 V; the operating voltage required for the SET process was +0.18 V and that for the RESET process was -0.10 V. The SET process could proceed at a lower voltage than that of the electroforming process because of the already-formed filament, which makes it easier to pass the SET filament. Initially, the sustained low current state of the device (10^{-12} A) abruptly changed to the high current state of the device (10^{-3} A) when the applied voltage exceeded the SET voltage. Subsequently, the sustained high current state abruptly changed to the low current state when the applied bias at negative polarity exceeded the RESET voltage. From the series of five I - V sweeps, reliable and reproducible resistive switching of the $(\text{PEA})_2\text{Cs}_3\text{Pb}_4\text{I}_{13}$ -based ReRAM devices was confirmed.

Figures 3. 4(b) and (c) show the statistically analyzed forming, SET, and RESET voltage distributions of 50 different $\text{Ag}/(\text{PEA})_2\text{Cs}_3\text{Pb}_4\text{I}_{13}/\text{Pt}$ cells for evaluating the uniformity of the operational function of the $(\text{PEA})_2\text{Cs}_3\text{Pb}_4\text{I}_{13}$ memory devices. From these distributions, there was no significant deviation in the forming voltages of the different 50 cells, nor did the SET and RESET voltages show any meaningful deviation.

Figure 3. 4(d) shows the HRS and LRS values of 50 different $\text{Ag}/(\text{PEA})_2\text{Cs}_3\text{Pb}_4\text{I}_{13}/\text{Pt}$ cells under applied write/erase voltage pulses. The result confirms that the average ON/OFF ratio did not differ significantly for the devices, which means that the reproducibility of the cells in resistive switching memory devices is superior.

The switching endurance, which confirms the stability and the number of switching cycles, is also one of the key factors influencing the reliability of resistive switching memory devices. Figure 3. 4(e) shows the endurance characteristics of the $(\text{PEA})_2\text{Cs}_3\text{Pb}_4\text{I}_{13}$ memory device, measured by applying alternating current (AC) voltage pulses. Continuous write/erase voltage pulses of +0.8 V for the SET process and -0.8 V for the RESET process were applied to the memory devices, with a 640 μs pulse duration and a read voltage of +0.05 V. The $\text{Ag}/(\text{PEA})_2\text{Cs}_3\text{Pb}_4\text{I}_{13}/\text{Pt}$ device was functional for 230 endurance cycles, with ON/OFF ratios above 10^8 .

The typical data retention for the ON and OFF states was also evaluated for the $\text{Ag}/(\text{PEA})_2\text{Cs}_3\text{Pb}_4\text{I}_{13}/\text{Pt}$ cell to test the electrical reliability of the memory device, as shown in Figure 3. 4(f). A constant ON/OFF ratio of $\sim 10^9$ was maintained for over 2×10^3 s at the reading voltage of +0.02 V. In the HRS region, a very small current fluctuation was observed, but the HRS and LRS remained constant overall.

To elucidate the current transport mechanisms of the resistive switching behavior, the typical $I-V$ curves of the devices were plotted using a double-logarithmic scale for each resistance state, as shown in Figure 3. 5(a). The electrical conduction of the $\text{Ag}/(\text{PEA})_2\text{Cs}_3\text{Pb}_4\text{I}_{13}/\text{Pt}$ memory device differed in the HRS and LRS during the SET operation under a voltage sweep of $0 \text{ V} \rightarrow +0.8 \text{ V} \rightarrow 0 \text{ V}$. First, it was found that the Ohmic conduction plot had a slope of 0.99, with a linear relation of $\ln I$ vs. $\ln V$ in the LRS region after the abrupt current increase.^{23,52-54}

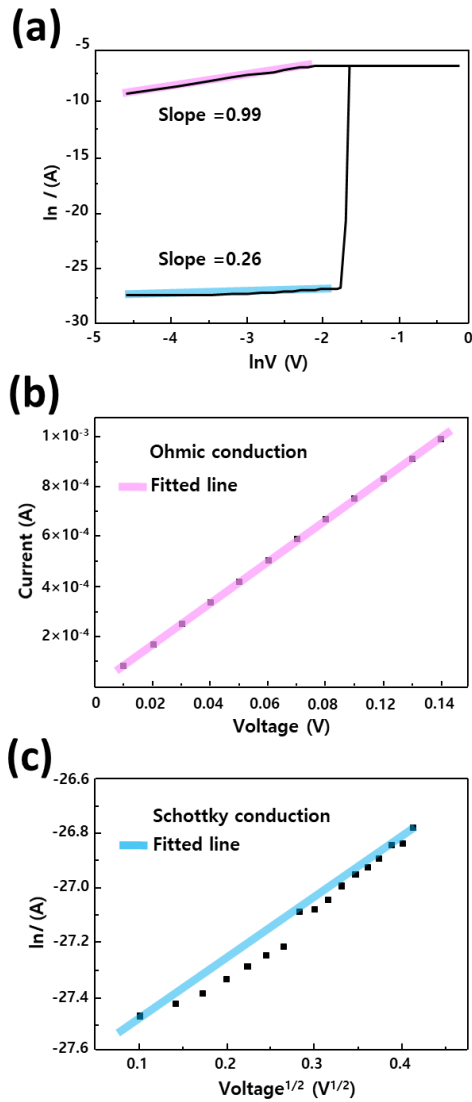


Figure 3. 5. Current transport mechanisms underlying resistive switching behavior. (a) Double-logarithmic scale of $I-V$ curve of the $\text{Ag}/(\text{PEA})_2\text{Cs}_3\text{Pb}_4\text{I}_{13}/\text{Pt}$ device. (b) Proportional relation of current density to voltage ($I \propto V$) for LRS. (c) Relation of current to square root of voltage ($\ln I \propto V^{1/2}$) for HRS.

In the HRS region, the relation of $\ln I$ vs. $\ln V$ was non-linear with a slope of 0.26, which verifies that Schottky emission is dominant.^{23,53,55}

In order to better understand the two types of electrical conduction mechanisms, i.e., Ohmic conduction in the LRS and Schottky emission in the HRS, the I - V curves of each resistance state were replotted with linear fitting lines. From Figure 3. 5(b), it is clear that the linear fitting conforms to Ohmic conduction in the LRS, as proven by the proportional relation of the current density to the voltage ($I \propto V$).⁵³ This indicates that Ohmic conduction governed the LRS after abrupt formation of the conducting filament by passing through the halide perovskite switching layer.

To further clarify whether Schottky emission is dominant in the HRS region during the SET operation, the nonlinear I - V curve of the HRS was replotted as $\ln I$ versus the square root of the applied voltage ($\ln I \propto V^{1/2}$), as illustrated in Figure 3. 5(c).

^{52,55,56}

The fitting result shows a linear relationship of $\ln I \propto V^{1/2}$, which can be taken as evidence that Schottky emission is dominant in the HRS region, according to the following equation:²³

$$\ln I \propto \sqrt{\frac{q^3}{4\pi\epsilon d} kT} \times \sqrt{V} \quad (2)$$

where I is the current, q is the electric charge, ε is the dielectric constant, d is the dielectric film thickness, and V is the applied voltage. The linearity of the replotted graph indicates that the metal cations are dissolved from the Ag top electrode by thermionic Schottky emission. In other words, in the HRS, Schottky contact is formed between the Ag top electrode and the halide perovskite layer, and ejected carriers from the top electrode can easily pass through the potential barrier. Furthermore, the results suggest that the limited current flow from the top electrode to the switching layer controls the HRS current level.

It is known that the current in the HRS is related to the Schottky barrier height; thus, we compared the linear replotted I - V curves for the HRS of the 3D CsPbI₃ and quasi-2D (PEA)₂Cs₃Pb₄I₁₃ memory devices. As shown in Figure 3. 6(a), the quasi-2D (PEA)₂Cs₃Pb₄I₁₃ memory device displayed lower current in the HRS, where the current density could be estimated according to the Richardson-Schottky law:

$$J = A \times T^2 \times \exp\left(\frac{q\sqrt{\frac{qE}{4\pi\varepsilon}}}{kT} - \frac{q\Phi_B}{kT}\right) \quad (3),$$

where A is the Richardson constant, E is the electric field, and Φ_B is the Schottky barrier height.^{57,58}

As expressed in Equation (3), the Schottky barrier height, Φ_B , corresponds to the current density in the HRS. The increased barrier height of quasi-2D $(\text{PEA})_2\text{Cs}_3\text{Pb}_4\text{I}_{13}$ limits the carrier flow from the Ag top electrode to the perovskite switching layer.

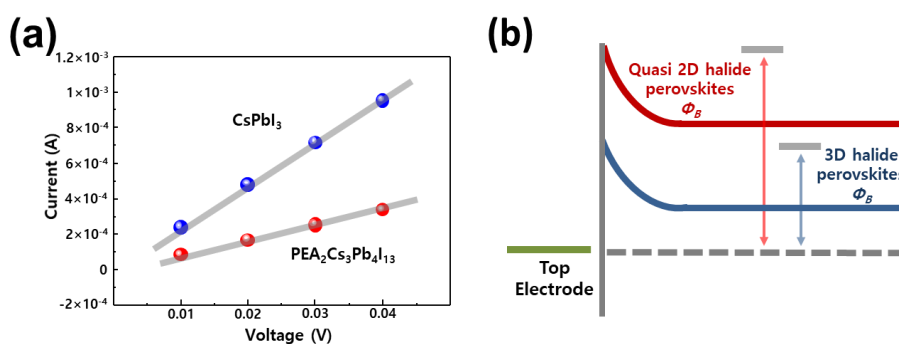


Figure 3. 6. (a) Comparison of linear replotted $I-V$ curves for HRS of CsPbI_3 and $(\text{PEA})_2\text{Cs}_3\text{Pb}_4\text{I}_{13}$ devices. (b) Schematic diagram of Schottky barrier heights for CsPbI_3 and $(\text{PEA})_2\text{Cs}_3\text{Pb}_4\text{I}_{13}$.

Figure 3. 6(b) shows a schematic representation of the Schottky barrier heights of these two perovskite materials, suggesting that band-bending induced by modifying the bandgap of the switching material controls the barrier height. Therefore, we can increase the HRS current to improve the ON/OFF ratio of the memory devices.

In the ECM mechanism, formation and rupture of the metal cation filament are caused by electrochemical reactions as well as thermal effects; therefore, the temperature-dependence of the memory devices should be investigated. To confirm the impact of temperature on the electrical characteristics of the device, I - V measurements were conducted over the temperature range of 293–393 K. Figure 3. 7(a) shows that the HRS current increased with increasing temperature. The increasing tendency of the current can be attributed to easy migration of the ejected metal cations into the switching layer after dissolution of the metal electrode.^{23,59}

Figures 3. 7(b), (c), and (d) display the decreasing and increasing trends for the forming, SET, and RESET voltages under DC voltage sweep when the temperature was elevated. In the forming and SET processes, the operating voltage is related to the rate of migration of the metal cations and the super-saturation of the metal. As the temperature increases, Ag metal cations easily move through a switching layer, then quickly reach super-saturation at the counter-electrode, even at a low voltage, thereby reducing the forming and SET voltages.^{59,60}

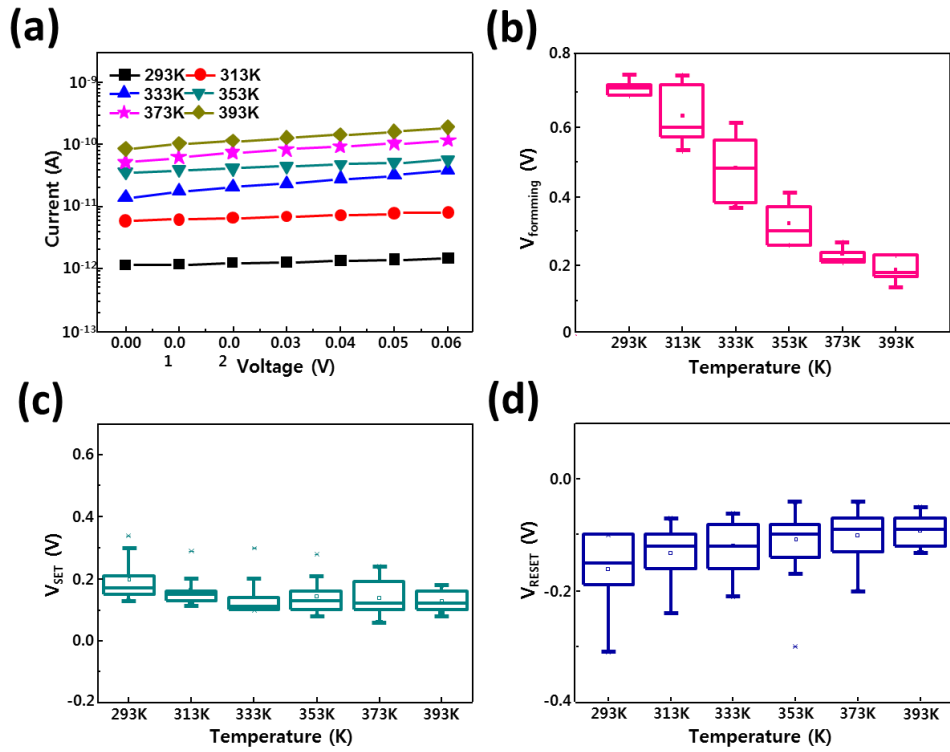


Figure 3. 7. (a) Temperature-dependence of HRS before SET process. (b, c, d) Tendency of forming (b), SET (c), and RESET (d) voltages under DC voltage sweep with increasing temperature.

In the RESET processes, rupture of the conducting filament at the counter-electrode occurs due to Joule heating-assisted dissolution.^{59–61} The narrow conducting filaments, which are thermally unstable, are easily broken at high temperature. For this reason, rupture of the Ag filament can easily take place at the counter-electrode as the temperature increases, even under a low-intensity electric field.

One of the issues for halide perovskite-based ReRAM devices is the stability. It is reported that the CsPbI₃ 3D halide perovskite is susceptible to humidity, resulting in rapid degradation when related devices are exposed to ambient conditions. Recently, to enhance the moisture resistance, some techniques have been introduced to maintain the stability, such as encapsulation or applying passivating polymer films to the devices. In our work, we found that the (PEA)₂Cs₃Pb₄I₁₃ quasi-2D halide perovskite was robust at room temperature under ambient conditions, compared to the CsPbI₃ 3D halide perovskites.

To confirm the superior stability of (PEA)₂Cs₃Pb₄I₁₃, the memory devices were kept under ambient atmosphere and the *I–V* characteristics were monitored. As illustrated in Figure 3. 8(a), the 3D perovskite memory device degraded after five days. However, from the *I–V* measurements for the quasi-2D perovskite memory devices in Figure 3. 8(b), it is clear that the stability was enhanced without appreciable decay after storage in air for two weeks.

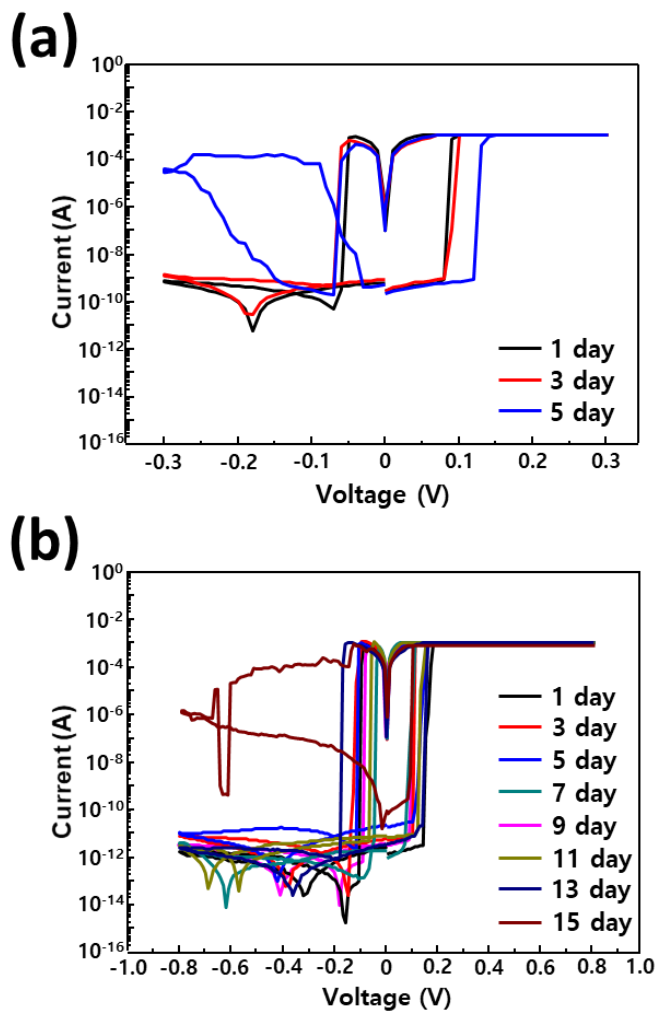


Figure 3. 8. Stability tests from I - V measurements of $\text{Ag}/\text{CsPbI}_3/\text{Pt}$ (a) and $\text{Ag}/(\text{PEA})_2\text{Cs}_3\text{Pb}_4\text{I}_{13}/\text{Pt}$ (b) devices.

The stable resistive switching behavior of this $(\text{PEA})_2\text{Cs}_3\text{Pb}_4\text{I}_{13}$ memory device is influenced by the multiple interaction forces in the quasi-2D structure, such as strong ionic bonds in the perovskite (inorganic) layer, weak van der Waals force between the PEA layers (mono ammonium cation layers), connections between organic and inorganic layers (the coordination bonds between ammonium group and Pb and the hydrogen bond between ammonium group and halogen).^{62,63}

Further, the hydrophobic PEA cation brings about steric hindrance, which affects the surface Pb–I to prevent the adsorption of water.⁶⁴ Additionally, the stacks of hydrophobic cation layers protect the inner perovskites from water molecules, thus minimizing water intake by the memory devices.

Thus, we confirmed that the PEA cations prevent destruction of the quasi-2D structure and provide moisture resistance, which counters degradation of the switching performance of the $(\text{PEA})_2\text{Cs}_3\text{Pb}_4\text{I}_{13}$ memory device.

3. 4. Conclusion

In summary, a large ionic radius cation (PEA) was introduced into CsPbI₃ in order to form a quasi-2D halide perovskite, (PEA)₂Cs₃Pb₄I₁₃, to achieve a high ON/OFF ratio in ReRAM devices. Uniform surface morphology was achieved by incorporating the PEA cation, and (PEA)₂Cs₃Pb₄I₁₃ effectively improved the resistive switching of the device.

The ReRAM device with the Ag/(PEA)₂Cs₃Pb₄I₁₃/Pt structure showed a high ON/OFF ratio of 10⁹, which is three orders higher than that of the CsPbI₃-based memory device. Owing to the wide bandgap of (PEA)₂Cs₃Pb₄I₁₃, a high Schottky barrier was formed and the activation energy increased, thereby leading to a reduction in the HRS current. A stability test verified the superior resistance of the device under ambient atmosphere at room temperature, which is another favorable property of quasi-2D perovskites. While the CsPbI₃ memory device was degraded after five days, the (PEA)₂Cs₃Pb₄I₁₃ devices were stable for two weeks, which is meaningful in terms of practical application of halide perovskite memory devices.

3. 5. Reference

- 1 M. A. Green, A. Ho-Baillie and H. J. Snaith, *Nat. Photonics*, 2014, **8**, 506–514.
- 2 H. Kim, G. Veerappan and J. H. Park, *Electrochim. Acta*, 2014, **137**, 164–168.
- 3 H. Kim, G. Veerappan, D. H. Wang and J. H. Park, *Electrochim. Acta*, 2016, **187**, 218–223.
- 4 N. Shibayama, H. Kanda, S. Yusa, S. Fukumoto, A. K. Baranwal, H. Segawa, T. Miyasaka and S. Ito, *Nano Converg.*, 2017, **4**, 18.
- 5 M. Patel, S. Park and J. Kim, 2018, **1800216**, 1–10.
- 6 H. Kim and J. Kim, *Data Br.*, 2017, **12**, 42–45.
- 7 H. Kim, D. B. Patel, H. Kim, M. Patel, K. R. Chauhan, W. Park and J. Kim, *Sol. Energy Mater. Sol. Cells*, 2017, **164**, 7–12.
- 8 M. Kumar, M. Patel, D. Y. Park, H. Kim, M. S. Jeong and J. Kim, 2019, **1800662**, 1–7.
- 9 Y. Dong, D. Parobek and D. H. Son, *J. Korean Ceram. Soc.*, 2018, **55**, 515–526.
- 10 J. W. Jo, Y. Yoo, T. Jeong, S. Ahn and M. J. Ko, *Electron. Mater. Lett.*, 2018, **14**, 657–668.
- 11 M. A. K. Sheikh, R. Abdur, S. Singh, J.-H. Kim, K.-S. Min, J. Kim and J. Lee, *Electron. Mater. Lett.*, 2018, **14**, 700–711.

- 12 M. A. A. Wadi, T. H. Chowdhury, I. M. Bedja, J.-J. Lee, N. Amin, M. Aktharuzzaman and A. Islam, *Electron. Mater. Lett.*, 2019, **15**, 525–546.
- 13 Y.-J. Jung, S.-Y. Cho, J.-W. Jung, S.-Y. Kim and J.-H. Lee, *Nano Converg.*, 2019, **6**, 26.
- 14 N.-G. Park, *Nano Converg.*, 2016, **3**, 15.
- 15 X. Ren and H. S. Jung, *J. Korean Ceram. Soc.*, 2018, **55**, 325–336.
- 16 B. Gil, A. J. Yun, Y. Lee, J. Kim, B. Lee and B. Park, *Electron. Mater. Lett.*, 2019, **15**, 505–524.
- 17 J. Choi, J. S. Han, K. Hong, S. Y. Kim and H. W. Jang, *Adv. Mater.*, 2018, **30**, 1704002.
- 18 J. Choi, Q. Van Le, K. Hong, C. W. Moon, J. S. Han, K. C. Kwon, P.-R. Cha, Y. Kwon, S. Y. Kim and H. W. Jang, *ACS Appl. Mater. Interfaces*, 2017, **9**, 30764–30771.
- 19 S. G. Kim, J. S. Han, H. Kim, S. Y. Kim and H. W. Jang, *Adv. Mater. Technol.*, 2018, **3**, 1800457.
- 20 C. Gu and J.-S. Lee, *ACS Nano*, 2016, **10**, 5413–5418.
- 21 H. Kim, J. S. Han, J. Choi, S. Y. Kim and H. W. Jang, *Small Methods*, 2018, **2**, 1700310.
- 22 J. Choi, S. Park, J. Lee, K. Hong, D.-H. Kim, C. W. Moon, G. Do Park, J. Suh, J. Hwang, S. Y. Kim, H. S. Jung, N.-G. Park, S. Han, K. T. Nam and H. W. Jang, *Adv. Mater.*, 2016, **28**, 6562–6567.

- 23 J. S. Han, Q. Van Le, J. Choi, K. Hong, C. W. Moon, T. L. Kim, H. Kim, S. Y. Kim and H. W. Jang, *Adv. Funct. Mater.*, 2018, **28**, 1705783.
- 24 W. Hu, N. Qin, G. Wu, Y. Lin, S. Li and D. Bao, *J. Am. Chem. Soc.*, 2012, **134**, 14658–14661.
- 25 I. Michelakaki, P. Bousoulas, S. Stathopoulos, N. Boukos and D. Tsoukalas, *J. Phys. D. Appl. Phys.*, 2017, **50**, 045103.
- 26 Y. Huang, Z. Shen, Y. Wu, X. Wang, S. Zhang, X. Shi and H. Zeng, *RSC Adv.*, 2016, **6**, 17867–17872.
- 27 Y. Wang, T. Zhang, M. Kan, Y. Li, T. Wang and Y. Zhao, *Joule*, 2018, **2**, 2065–2075.
- 28 G. Jia, Z.-J. Shi, Y.-D. Xia, Q. Wei, Y.-H. Chen, G.-C. Xing and W. Huang, *Opt. Express*, 2018, **26**, A66.
- 29 Y. Han, S. Park, C. Kim, M. Lee and I. Hwang, *Nanoscale*, 2019, **11**, 3546–3556.
- 30 F. Li, Y. Pei, F. Xiao, T. Zeng, Z. Yang, J. Xu, J. Sun, B. Peng and M. Liu, *Nanoscale*, 2018, **10**, 6318–6322.
- 31 J. Yan, W. Qiu, G. Wu, P. Heremans and H. Chen, *J. Mater. Chem. A*, 2018, **6**, 11063–11077.
- 32 J. Fan, Y. Ma, C. Zhang, C. Liu, W. Li, R. E. I. Schropp and Y. Mai, *Adv. Energy Mater.*, 2018, **8**, 1703421.

- 33 Y. F. Ng, S. A. Kulkarni, S. Parida, N. F. Jamaludin, N. Yantara, A. Bruno, C. Soci, S. Mhaisalkar and N. Mathews, *Chem. Commun.*, 2017, **53**, 12004–12007.
- 34 J. Gebhardt, Y. Kim and A. M. Rappe, *J. Phys. Chem. C*, 2017, **121**, 6569–6574.
- 35 S. Ma, M. Cai, T. Cheng, X. Ding, X. Shi, A. Alsaedi, T. Hayat, Y. Ding, Z. Tan and S. Dai, *Sci. China Mater.*, 2018, **61**, 1257–1277.
- 36 L. N. Quan, M. Yuan, R. Comin, O. Voznyy, E. M. Beauregard, S. Hoogland, A. Buin, A. R. Kirmani, K. Zhao, A. Amassian, D. H. Kim and E. H. Sargent, *J. Am. Chem. Soc.*, 2016, **138**, 2649–2655.
- 37 Y. Liao, H. Liu, W. Zhou, D. Yang, Y. Shang, Z. Shi, B. Li, X. Jiang, L. Zhang, L. N. Quan, R. Quintero-Bermudez, B. R. Sutherland, Q. Mi, E. H. Sargent and Z. Ning, *J. Am. Chem. Soc.*, 2017, **139**, 6693–6699.
- 38 Z. Wang, Q. Lin, F. P. Chmiel, N. Sakai, L. M. Herz and H. J. Snaith, *Nat. Energy*, 2017, **2**, 17135.
- 39 K. Hong, Q. Van Le, S. Y. Kim and H. W. Jang, *J. Mater. Chem. C*, 2018, **6**, 2189–2209.
- 40 J.-Y. Seo, J. Choi, H.-S. Kim, J. Kim, J.-M. Yang, C. Cuhadar, J. S. Han, S.-J. Kim, D. Lee, H. W. Jang and N.-G. Park, *Nanoscale*, 2017, **9**, 15278–15285.
- 41 H. Kim, K. A. Huynh, S. Y. Kim, Q. Van Le and H. W. Jang, *Phys. status solidi – Rapid Res. Lett.*, 2019, **3**, 1900435.

- 42 R. K. Misra, B.-E. Cohen, L. Iagher and L. Etgar, *ChemSusChem*, 2017, **10**, 3712–3721.
- 43 M. Ban, Y. Zou, J. P. H. Rivett, Y. Yang, T. H. Thomas, Y. Tan, T. Song, X. Gao, D. Credgington, F. Deschler, H. Sirringhaus and B. Sun, *Nat. Commun.*, 2018, **9**, 3892.
- 44 N. K. Kumawat, D. Gupta and D. Kabra, *Energy Technol.*, 2017, **5**, 1734–1749.
- 45 G. E. Eperon, G. M. Paternò, R. J. Sutton, A. Zampetti, A. A. Haghighirad, F. Cacialli and H. J. Snaith, *J. Mater. Chem. A*, 2015, **3**, 19688–19695.
- 46 Y. Jiang, J. Yuan, Y. Ni, J. Yang, Y. Wang, T. Jiu, M. Yuan and J. Chen, *Joule*, 2018, **2**, 1356–1368.
- 47 H.-W. Huang, C.-F. Kang, F.-I. Lai, J.-H. He, S.-J. Lin and Y.-L. Chueh, *Nanoscale Res. Lett.*, 2013, **8**, 483.
- 48 H. Kim, J. S. Han, S. G. Kim, S. Y. Kim and H. W. Jang, *J. Mater. Chem. C*, 2019, **7**, 5226–5234.
- 49 W. Zhu, T. P. Chen, Y. Liu and S. Fung, *J. Appl. Phys.*, 2012, **112**, 063706.
- 50 T. H. Park, S. J. Song, H. J. Kim, S. G. Kim, S. Chung, B. Y. Kim, K. J. Lee, K. M. Kim, B. J. Choi and C. S. Hwang, *Phys. status solidi - Rapid Res. Lett.*, 2015, **9**, 362–365.
- 51 R. Waser, R. Dittmann, G. Staikov and K. Szot, *Adv. Mater.*, 2009, **21**, 2632–2663.

- 52 A. M. Rana, T. Akbar, M. Ismail, E. Ahmad, F. Hussain, I. Talib, M. Imran, K. Mehmood, K. Iqbal and M. Y. Nadeem, *Sci. Rep.*, 2017, **7**, 39539.
- 53 E. Lim and R. Ismail, *Electronics*, 2015, **4**, 586–613.
- 54 L.-M. Lin, W.-L. Yang, Y.-H. Lin, Y.-P. Hsiao, F.-T. Chin and M.-F. Kao, *Phys. status solidi*, 2017, **214**, 1600595.
- 55 D. J. J. Loy, P. A. Dananjaya, X. L. Hong, D. P. Shum and W. S. Lew, *Sci. Rep.*, 2018, **8**, 14774.
- 56 C.-H. Wu, T.-C. Chang, T.-M. Tsai, K.-C. Chang, T.-J. Chu, C.-H. Pan, Y.-T. Su, P.-H. Chen, S.-K. Lin, S.-J. Hu and S. M. Sze, *Appl. Phys. Express*, 2017, **10**, 054101.
- 57 J. Park, K. P. Biju, S. Jung, W. Lee, J. Lee, S. Kim, S. Park, J. Shin and H. Hwang, *IEEE Electron Device Lett.*, 2011, **32**, 476–478.
- 58 S. C. Chen, J. C. Lou, C. H. Chien, P. T. Liu and T. C. Chang, *Thin Solid Films*, 2005, **488**, 167–172.
- 59 J. S. Han, Q. Van Le, J. Choi, H. Kim, S. G. Kim, K. Hong, C. W. Moon, T. L. Kim, S. Y. Kim and H. W. Jang, *ACS Appl. Mater. Interfaces*, 2019, **11**, 8155–8163.
- 60 T. Tsuruoka, K. Terabe, T. Hasegawa and M. Aono, *Nanotechnology*, 2011, **22**, 254013.
- 61 T. Tsuruoka, K. Terabe, T. Hasegawa and M. Aono, *Nanotechnology*, 2010, **21**, 425205.

- 62 F. Xu, T. Zhang, G. Li and Y. Zhao, *J. Mater. Chem. A*, 2017, **5**, 11450–11461.
- 63 X. Zhu, Z. Xu, S. Zuo, J. Feng, Z. Wang, X. Zhang, K. Zhao, J. Zhang, H. Liu, S. Priya, S. F. Liu and D. Yang, *Energy Environ. Sci.*, 2018, **11**, 3349–3357.
- 64 S. Yang, Y. Wang, P. Liu, Y.-B. Cheng, H. J. Zhao and H. G. Yang, *Nat. Energy*, 2016, **1**, 15016.
- 65 E. J. Yoo, M. Lyu, J.-H. Yun, C. J. Kang, Y. J. Choi and L. Wang, *Adv. Mater.*, 2015, **27**, 6170–6175.
- 66 K. Yan, B. Chen, H. Hu, S. Chen, B. Dong, X. Gao, X. Xiao, J. Zhou and D. Zou, *Adv. Electron. Mater.*, 2016, **2**, 1600160.
- 67 H. Cai, G. Ma, Y. He, C. Liu and H. Wang, *Org. Electron.*, 2018, **58**, 301–305.
- 68 D. Liu, Q. Lin, Z. Zang, M. Wang, P. Wangyang, X. Tang, M. Zhou and W. Hu, *ACS Appl. Mater. Interfaces*, 2017, **9**, 6171–6176.
- 69 B. Hwang and J.-S. Lee, *Sci. Rep.*, 2017, **7**, 673.
- 70 B. Hwang and J.-S. Lee, *Nanoscale*, 2018, **10**, 8578–8584.
- 71 Y. Liu, F. Li, Z. Chen, T. Guo, C. Wu and T. W. Kim, *Vacuum*, 2016, **130**, 109–112.
- 72 K. Yang, F. Li, C. P. Veeramalai and T. Guo, *Appl. Phys. Lett.*, 2017, **110**, 083102.

- 73 Y. Hu, S. Zhang, X. Miao, L. Su, F. Bai, T. Qiu, J. Liu and G. Yuan, *Adv. Mater. Interfaces*, 2017, **4**, 1700131.
- 74 B. Hwang and J.-S. Lee, *Adv. Mater.*, 2017, **29**, 1701048.
- 75 Y. Wu, Y. Wei, Y. Huang, F. Cao, D. Yu, X. Li and H. Zeng, *Nano Res.*, 2017, **10**, 1584–1594.
- 76 S. Lee, J. Choi, J. B. Jeon, B. J. Kim, J. S. Han, T. L. Kim, H. S. Jung and H. W. Jang, *Adv. Electron. Mater.*, 2019, **5**, 1800586.
- 77 C. Cuhadar, S.-G. Kim, J.-M. Yang, J.-Y. Seo, D. Lee and N.-G. Park, *ACS Appl. Mater. Interfaces*, 2018, **10**, 29741–29749.
- 78 X. Zhu, J. Lee and W. D. Lu, *Adv. Mater.*, 2017, **29**, 1700527.

Chapter 4

Tailored 2D/3D Halide Perovskite Heterointerface for Substantially Enhanced Endurance

4. 1. Introduction

Resistive random-access memory (ReRAM) is the most promising candidate for next-generation memory technology because of its low operation energy, high integration density, and high switching speed¹⁻⁷. Generally, the structure of ReRAM comprises a traditional metal/insulator/metal (MIM) in which the insulator provides a resistance state that is different from the low-resistance state (LRS) and high resistance state (HRS), which can be achieved by applying a voltage amplitude or bias polarity. Most research on insulators has focused on binary oxide materials such as TaO_x, HfO_x, TiO_x, and new functional materials such as perovskite oxides (Pr_xCa_{1-x}MnO₃, SrTiO₃, BaTiO₃, and BiFeO₃)⁸⁻¹⁴. However, oxide-based materials are not suitable for applications in flexible and low-power devices because these require a high temperature process and high-operation voltage.

Halide perovskites with an ABX₃ structure, where A is an organic (CH₃NH₃) or inorganic (Cs, Rb) cation, B is a metal cation (Pb, Sn), and X is a halide anion (I, Br, or Cl), have been reported to exhibit excellent material properties such as superior flexibility, tunable band structure, and excellent optoelectronic properties¹⁵⁻²². The development of halide perovskites-based resistive switching resistive switching memory devices has particularly seen rapid progress because of their low operation voltages, high ON/OFF ratios, and superior flexibility. Moreover, halide perovskites-based resistive switching memory devices are suitable to take artificial

synaptic devices by synergistic coupling of remarkable photonic, electronic, and ionic properties of halide perovskites^{23–26}.

However, the critical weaknesses of these devices such as short endurance and instability are a major obstruction for their entrance into the future resistive switching memory market. In particular, a conventional oxide-based resistive switching memory device exhibited long

endurance of more than 10^6 cycles, whereas halide perovskites-based resistive switching memory devices have a very short endurance of about 10^3 cycles^{22,27}. Several solutions have been investigated to address these issues such as externally encapsulating the halide perovskite film^{28–31}, uniform morphology/high crystallinity of halide perovskites films by solvent engineering and additives, and synthesizing a chemically more stable composition of halide perovskites films^{22,32–39}. However, despite many efforts, the deterioration of the halide perovskite films could not be resolved.

In our recent earlier study, we reported the resistive switching property of switchable methylammonium lead iodide (MAPbI_3) and non-switchable rubidium lead iodide (RbPbI_3) mixtures. The non-switchable RbPbI_3 was observed to enhance the endurance of the halide perovskite film by restraining the growth of the Ag filament. Thus, we observed that long endurance of halide perovskite-based devices can be achieved by mainly controlling the growth of the Ag filament³³.

In this study, we fabricated halide perovskite-based resistive switching memory devices in two-dimensional (2D) perovskite (phenethylammonium lead iodide, PEA₂PbI₄)/three-dimensional (3D) perovskite (MAPbI₃) heterojunction structures via a low-temperature all-solution process and investigated their properties. The 2D/3D perovskite, which was used as an active layer, significantly enhanced the endurance from 300 cycles to more than 2700 cycles with a high ON/OFF ratio of >10⁶, an operation speed of 640 μs, and long-term stability for 28 days. Furthermore, to understand the growth behavior of the Ag filament, we measured the *I*–*V* characteristics of the halide perovskite-based resistive switching devices at various temperatures and calculated their hopping activation energy. In addition, the distribution of the Ag ions in the halide perovskite films was observed by secondary ion mass spectroscopy (SIMS) and 3D rendering. Furthermore, we simulated the filament rupture point that is caused by the difference in the thermal conductivities between 2D and 3D perovskite. Hence, we believe that this study could provide a new strategy to enhance the endurance of halide perovskite-based resistive switching memories for next generation nonvolatile computer storage.

4.2. Experimental Section

Materials

All materials were used without purification. PbI_2 (99.9985%) was purchased from Alfa Aesar (U.S.A.), PEAI was purchased from GreatCell Solar (Australia), and MAI from Xi'AnP-OLED Co. (China). Except of three materials were purchased from Sigma-Aldrich (USA).

Device Fabrication

Pt/Ti-coated Si wafer substrates were cleaned by an ultrasonic bath in acetone, ethanol, and deionized water for 15 min each. The 3D perovskite solution (55 wt.% MAI, PbI_2 and DMSO (Sigma-Aldrich, >99.9 %), was prepared at 1:1 molar ratio, in dimethylformamide (DMF) (Sigma-Aldrich, 99.8 %). The 3D perovskite precursor solution was coated on the Pt/Ti-coated Si wafer substrate by an adduct method reported by Park et al. Then, 8.5 μL of the dissolved solution was spin coated on the substrates at 4000 rpm for 20 s and 0.3 mL of diethyl ether (Sigma-Aldrich) was dropped for 10 s after starting the spin coating. The spin-coated 3D perovskite films were annealed at 70 °C for 1 min and then at 100 °C for 3 min. After cooling to room temperature, the 2D organic perovskite precursor was coated on the 3D perovskite/Pt/Ti-coated Si wafer substrate. The 2D organic perovskite precursor solution consisted of 10 mg, 20 mg and 30 mg PEAI in 1 mL of IPA (Sigma-Aldrich, 99.5%). The spin-coated 2D/3D perovskite films were annealed at 100 °C for 1 min and washed with 0.5 mL IPA. The washed 2D perovskite/3D perovskite films were

annealed at 100 °C for 1 min, cooled to room temperature, and subsequently, 20 μ L of poly(methyl methacrylate) (PMMA) solution was deposited by spin coating at 4000 rpm for 30 s; the PMMA solution consisted of 2 mg PMMA (Sigma-Aldrich) in 1 mL of chlorobenzene (Sigma-Aldrich, 99.8 %). Finally, 50 nm metallic Ag was thermally evaporated on top of the devices.

Device characterization

The surface and cross-sectional images were obtained by FESEM (JSM-7600F, JEOL). The crystal structures were detected by GI-XRD (D8 advance, Bruker) and XRD (SmartLab, RIGAJU) with Cu K α radiation ($\lambda = 1.54056 \text{ \AA}$). The XRD data were recorded in the 2θ range of 5° to 60° at scan speed of 6° min⁻¹. All electrical properties were detected using an Agilent 4156C semiconductor in a vacuum probe station under approximately 10⁻² torr. The *I-V* characteristics were measured in the direct current (DC) voltage sweeping mode at various temperatures (243, 273, 303, and 333 K) and various compliance currents (positive bias region 10⁻³, 10⁻⁴, 10⁻⁵, and 10⁻⁶ A; negative bias region 10⁻² A); resistive switching was measured by voltage pulses. To observe the conduction mechanism in the 2D/3D perovskite films, halide perovskite-based resistive switching devices were investigated using TOF.SIMS-5 (IONTOF, Germany). Their thermal conductivity and heat capacity were measured by the light flash technique (LFA467, Netzsch). To confirm the rupture mechanism, the 2D/3D perovskite film was simulated by COMSOL simulation (COMSOL Multiphysics, USA).

4. 3. Results and Discussion

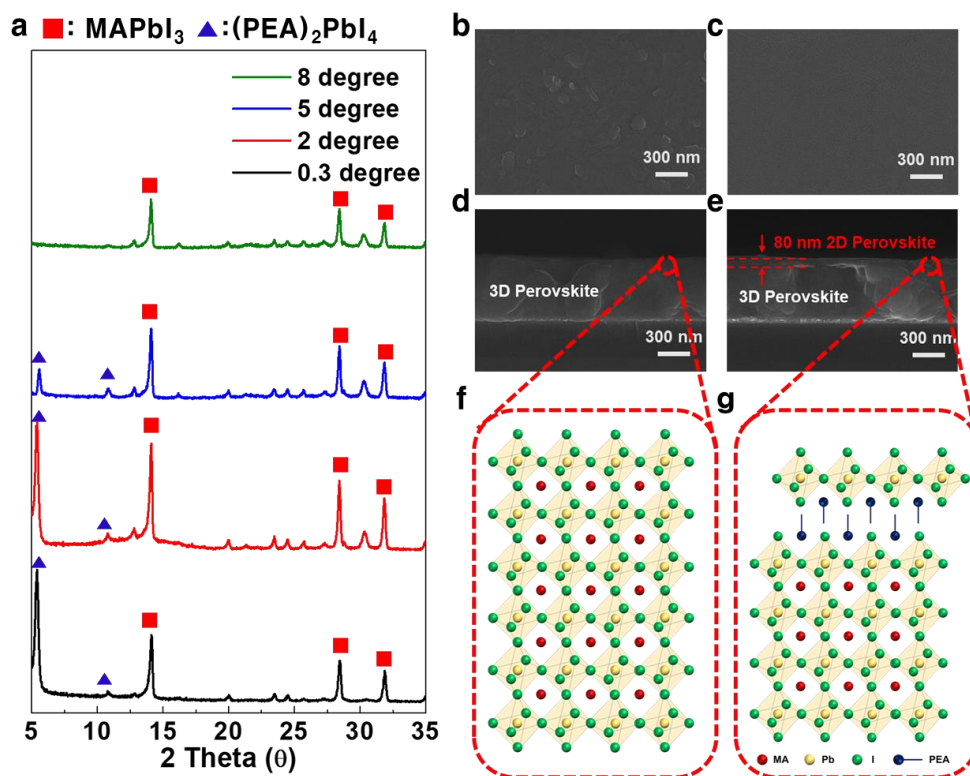


Figure 4. 1. (a) GIXRD patterns of the 2D/3D perovskite film at X-ray incident angles of 0.3°, 2°, 5°, and 8° (the filled triangles and squares denote the diffraction peaks corresponding to the 2D and 3D perovskite, respectively). The morphologies of the 3D perovskite and 2D/3D perovskite film; plane view scanning electron microscopy (SEM) images of: (b) 3D perovskite and (c) 2D/3D perovskite film. Cross-sectional SEM images of: (d) 3D perovskite and (e) 2D/3D perovskite film. Comparison of the crystalline structure of: (f) 3D perovskite and (g) 2D/3D perovskite film.

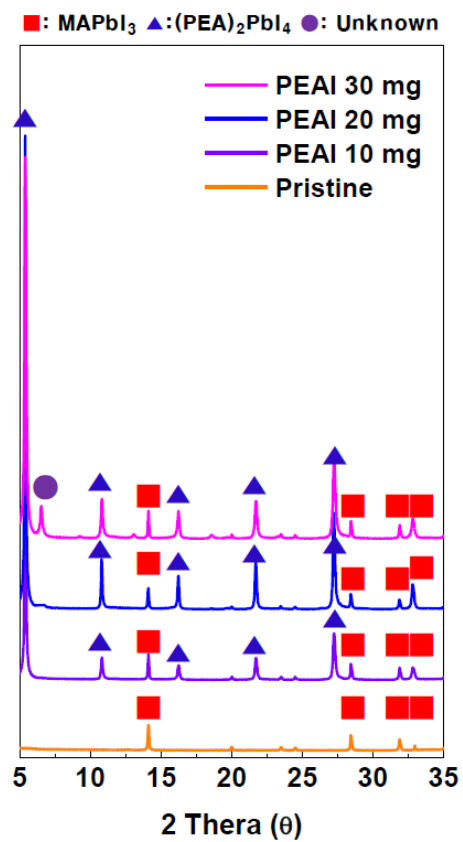


Figure 4. 2. XRD patterns of the 2D/3D perovskite films fabricated using different concentrations of PEAI solution.

Figure 4. 1a shows the grazing-incidence X-ray diffraction (GIXRD) patterns of the 2D/3D perovskite films at different incident angles. The main peaks obtained using MAPbI₃ as the 3D perovskite film are observed at 14.12, 28.46, and 31.88°, which are well matched with the tetragonal structure of the (110), (220), and (310) planes^{17,19,20}, respectively. The 2D perovskite layer was spin-coated on the 3D perovskite film.

Figure 4. 2 shows the XRD patterns of the 2D/3D perovskite films with increasing phenylethylammonium iodide (PEAI) concentrations. The peaks obtained for PEA₂PbI₄ as a 2D perovskite film are observed at 5.4 and 10.82° for the monoclinic structure assigned to the (002) and (004) planes, respectively⁴⁰⁻⁴². In the GI-XRD patterns, the PEA₂PbI₄ peak disappeared at high incident angles of more than 8°, indicating the formation of a thin 2D perovskite layer on the 3D perovskite film.

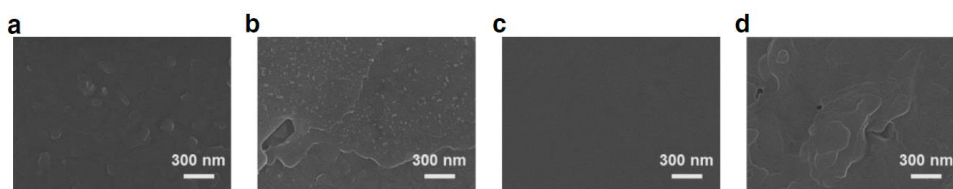


Figure 4. 3. Plane view scanning electron microscopy (SEM) images of: (a) pristine 3D perovskite, (b) 10 mg PEA₂PbI₄, (c) 20 mg PEA₂PbI₄, and (d) 30 mg PEA₂PbI₄.

To confirm the uniformity of this layer, we observed the 2D perovskite surfaces with increased PEAI concentrations, as shown in Figures 4. 1b-e and Figure 4. 3.

The thickness of the 3D perovskite film is approximately 500 nm, and its grain size is 100 nm. At low PEAI concentrations, the grain of 3D perovskite was exposed on the surface of the 2D/3D perovskite film. On the other hand, a high PEAI concentration can create the unknown phase and non-uniform layer on the 3D perovskite film, as shown in Figures 4. 2 and 4. 3.

Specifically, we observed that a 2D perovskite layer with an approximately 80 nm thickness is well covered on the 3D perovskite film when a 20 mg mL⁻¹ PEA solution is used. Figure 4. 1f and g shows the schematic of the crystal structure of the 3D perovskite and 2D/3D perovskite films, respectively. We observed that the structure of the 3D perovskite layer with MAPbI₃ contains the methylammonium cation (MA⁺) surrounded by PbI₆ octahedra. The structure of the 2D perovskite is represented as PEA_{n+1}Pb_nI_{3n+1}, known as the Ruddlesden–Popper phase, where n is the number of the layers of octahedra in the perovskite-like stack. Hence, the 2D perovskite PEA₂PbI₄ layer is stacked on top of 3D perovskite MAPbI₃. This 2D/3D perovskite structure was designed to improve the endurance and stability of halide perovskite-based resistive switching devices.

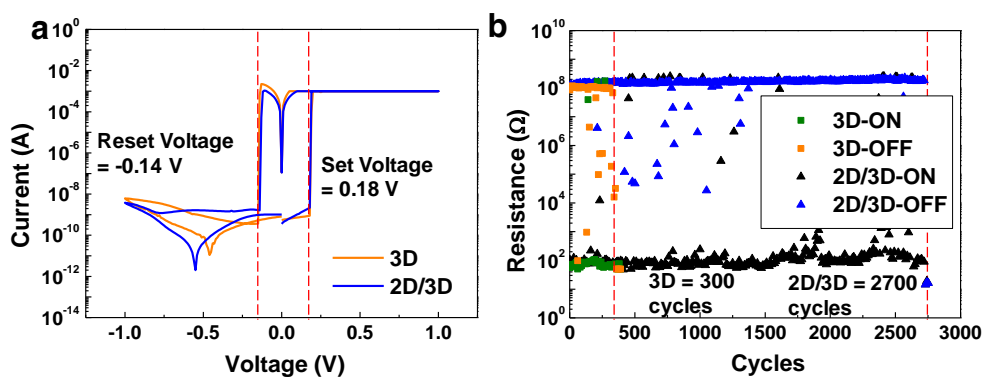


Figure 4. 4. (a) Typical current–voltage (I - V) characteristics of halide perovskite-based resistive switching devices. (2D/3D- PEAI 20 mg) (b) Resistive switching behavior measured with the DC pulses. Pulse duration is fixed at 640 μ s.

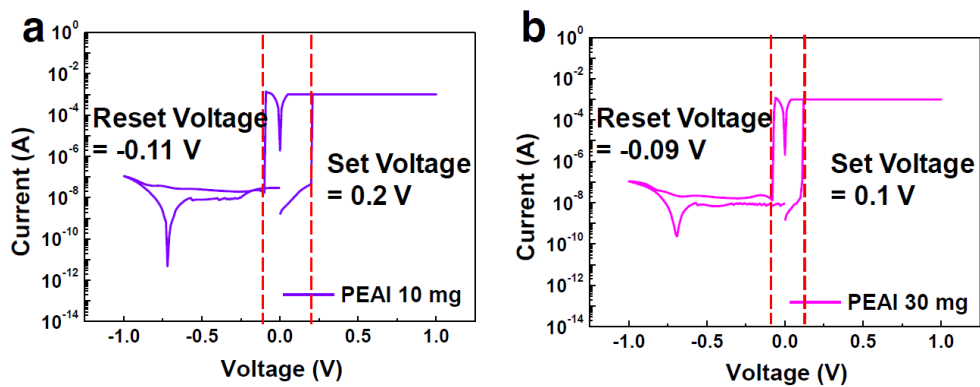


Figure 4. 5. Typical current-voltage (I - V) characteristics of halide perovskite-based resistive switching devices. (a) PEAI 10 mg (b) PEAI 30 mg.

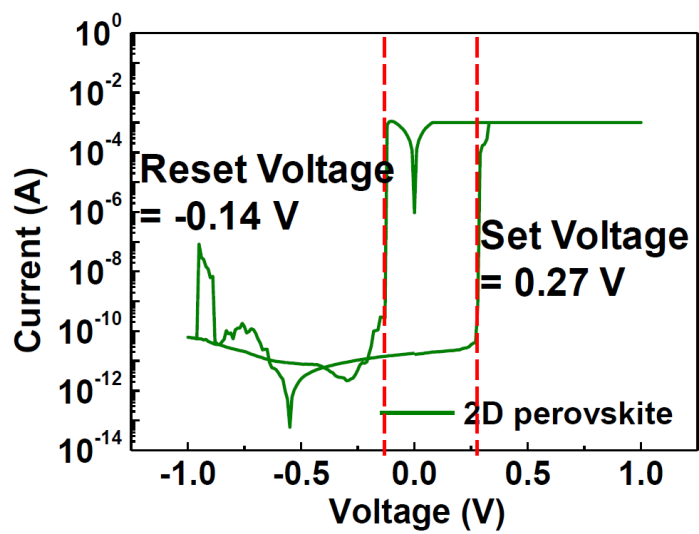


Figure 4. 6. Typical I - V characteristics of 2D halide perovskite-based resistive switching devices.

Figures 4a, 5, and 6 show the typical I–V characteristics of the halide perovskite-based devices, measured under the DC sweeping mode with a voltage step of 0.01 V (0 V → +1 V → 0 V → -1 V → 0 V). The characteristics of the 2D/3D perovskite films are similar to those of the pristine 3D perovskite films in which both halide perovskite-based devices exhibit bipolar resistive switching at about ± 0.18 V without the electroforming process. The devices maintained an HRS at $\sim 10^{-10}$ A. Then, the current levels were sharply increased to the LRS at $\sim 10^{-3}$ A under the applied bias voltage, $+0.18 \pm 0.1$ V. However, after applying a negative bias voltage sweep of -0.11 ± 0.05 V, the current level dramatically changed to an HRS (Figure 4. 7).

In addition, multilevel resistive switching properties of both devices could exploit the high data storage density of the memory due to its high ON/OFF ratio, as shown in Figure 4. 8. When the compliance current was changed from 10^{-3} to 10^{-6} A for the positive bias sweep, reversible resistive switching was feasible without negligible fluctuations in the set voltage. On the other hand, reversible resistive switching at negative bias sweep exhibited slight fluctuations in the reset voltage.

Figure 4. 4b shows the endurance of a 2D/3D perovskite device with a pulse duration of 640 μ s, compared with that of a 3D perovskite device. The switching voltage for the set/reset process was the same for all devices. The endurance of the pristine 3D perovskite device was only about 350 cycles. However, the endurance of the 2D/3D perovskite device was considerably extended to ~ 2700 cycles at the PEAI concentration of 20 mg mL⁻¹.

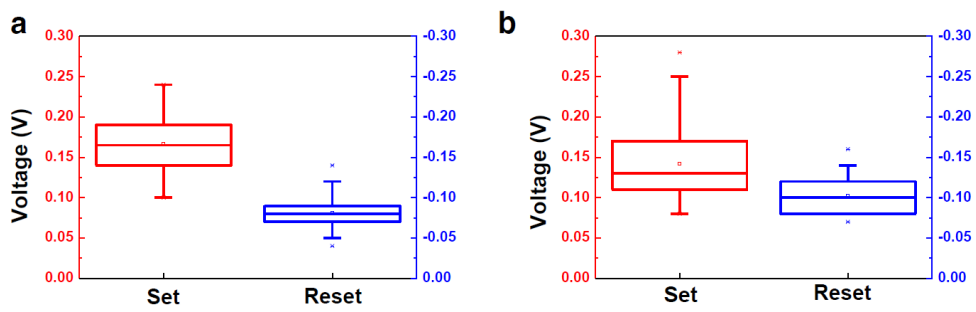


Figure 4. 7. Average of set and reset voltage. (a) 3D perovskite and (b) 2D/3D perovskite.

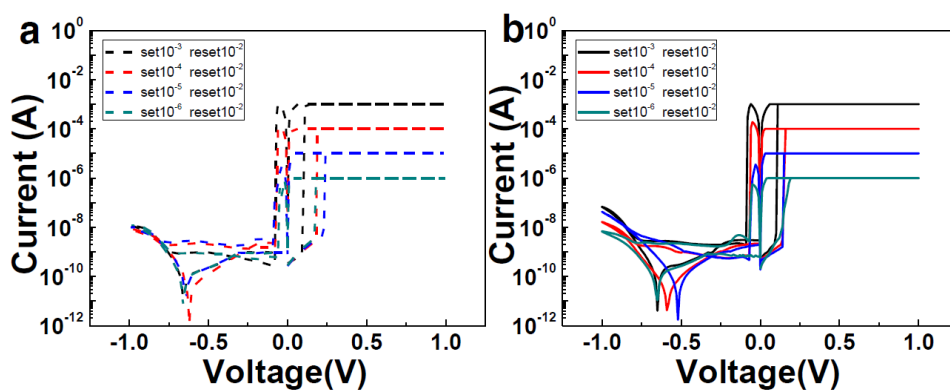


Figure 4. 8. I - V characteristics exhibiting the potential for multilevel switching (a) I - V characteristics of 3D perovskite and (b) I - V characteristics of 2D/3D perovskite (compliance current = 10^{-3} , 10^{-4} , 10^{-5} , and 10^{-6} A).

Figure 4. 9 shows the endurance of the fabricated 2D/3D perovskite device with different PEAI concentrations. A low PEAI concentration (10 mg mL^{-1}) has similar endurance cycles to those obtained using a pristine 3D perovskite device because of its many pinholes on top of the 3D perovskite film (see Figure 4. 3b).

In high PEAI concentrations (30 mg mL^{-1}), the endurance of 2D/3D perovskite is significantly decreased to ~ 150 cycles, compared to ~ 2700 cycles at the PEAI concentration of 20 mg mL^{-1} . It may be interrupted by a thick 2D layer. In addition, the pure 2D perovskite devices exhibited an endurance of only ~ 80 cycles, as shown in Figure 4. 10. This indicates that the coverage and thickness of the 2D layer on top of the 3D perovskite film are crucial for improving the endurance of the halide perovskite-based resistive switching memory devices.

Furthermore, we investigated the retention characteristics of the halide perovskite-based devices in the on state (write voltage, $+0.5 \text{ V}$; read voltage, $+0.02 \text{ V}$ for $10\ 000 \text{ s}$ with a pulse duration of $640 \mu\text{s}$).

In Figure 4. 11, the retention of the 3D perovskite device was up to 4100 s , while the 2D/3D perovskite device maintained an LRS for more than $10\ 000 \text{ s}$. This suggests that the 2D perovskite layer can enhance the durability and reproducibility of the halide perovskite-based resistive switching devices.

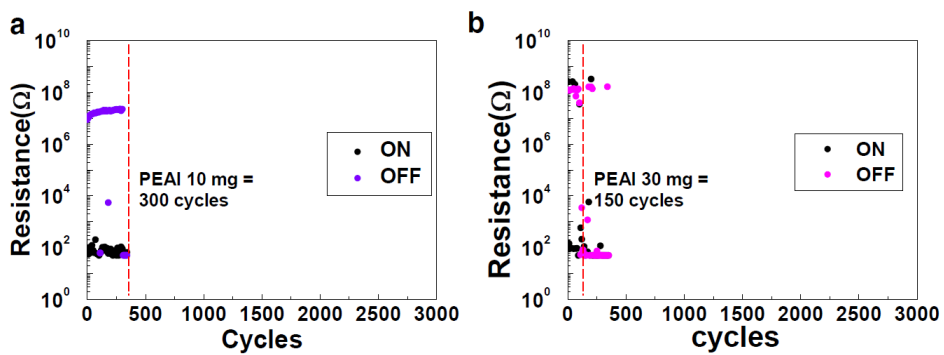


Figure 4. 9. Resistive switching behavior measured with the DC pulses. Pulse duration is fixed at $640 \mu\text{s}$. (a) PEAI 10 mg (b) PEAI 30 mg.

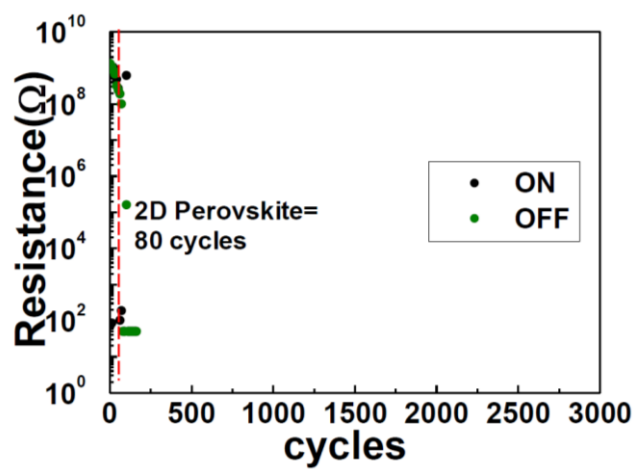


Figure 4. 10. 2D perovskite based resistive switching behavior measured with the DC pulses. Pulse duration is fixed at 640 μ s.

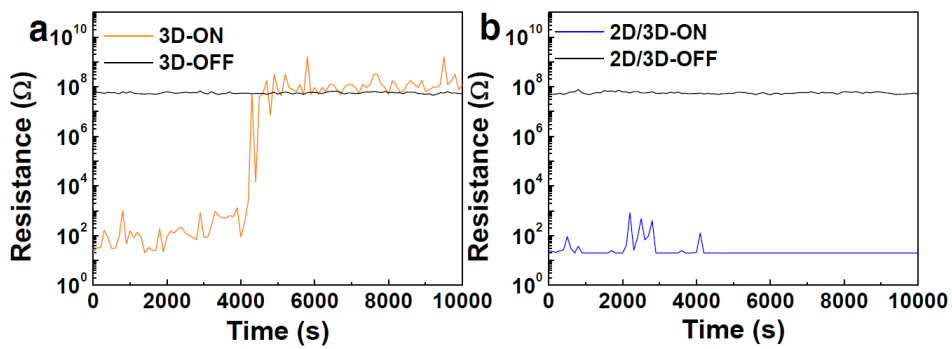


Figure 4. 11. Retention characteristics of the halide perovskite-based resistive switching devices: (a) 3D perovskite and (b) 2D/3D perovskite.

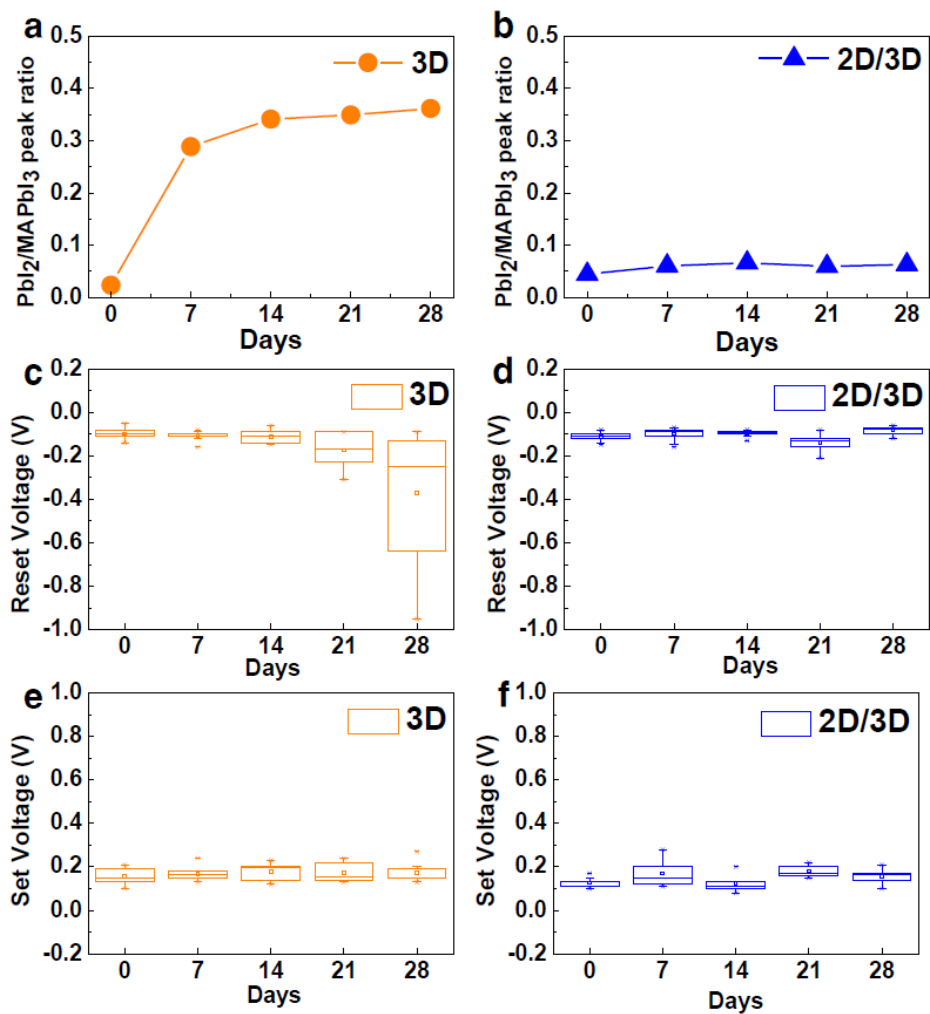


Figure 4. 12. Long-term stability of the halide perovskite-based resistive switching devices: (a,b) PbI₂/MAPbI₃ peak ratio of halide perovskite -based resistive switching devices. (c,d) Reset voltage deviation of halide perovskite-based resistive switching devices. (e,f) Set voltage deviation of halide perovskite-based resistive switching devices. (a,c,e) 3D perovskite and (b,d,f) 2D/3D perovskite.

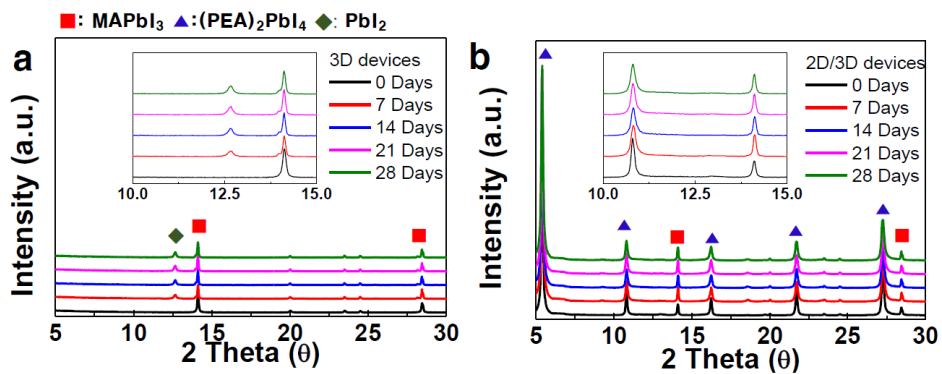


Figure 4. 13. XRD patterns of the halide perovskite-based resistive switching devices as a function of time: (a) 3D perovskite and (b) 2D/3D perovskite.

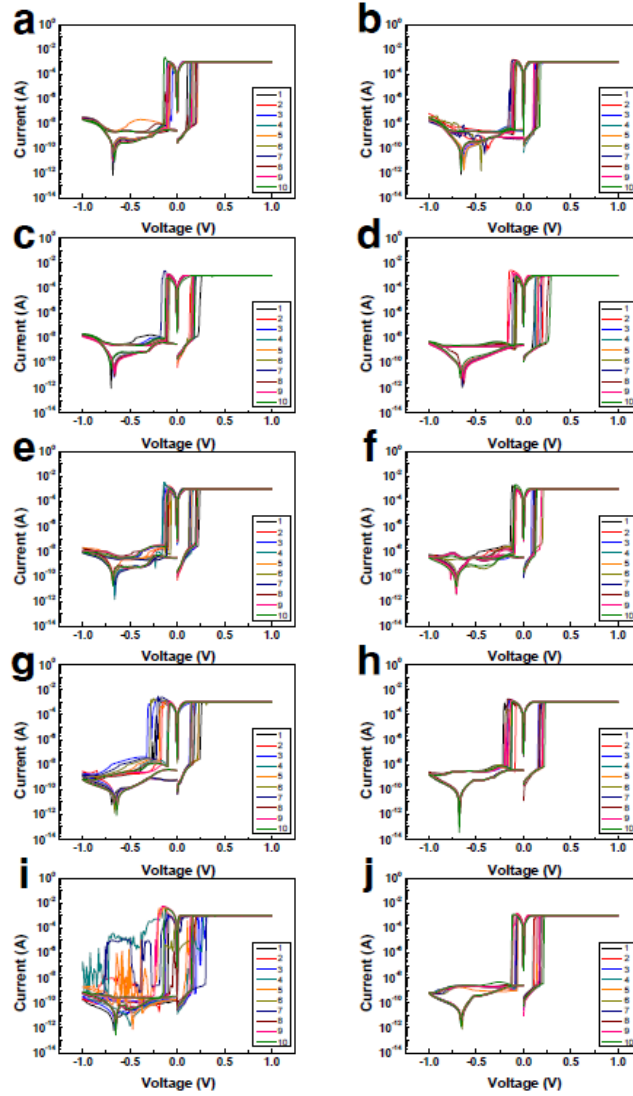


Figure 4. 14. I - V characteristics of halide perovskite-based resistive switching devices for long-term stability: (a) 0 days 3D perovskite, (b) 0 days 2D/3D perovskite, (c) 7 days 3D perovskite, (d) 7 days 2D/3D perovskite, (e) 14 days 3D perovskite, (f) 14 days 2D/3D perovskite, (g) 21 days 3D perovskite, (h) 21 days 2D/3D perovskite, (i) 28 days 3D perovskite, and (j) 28 days 2D/3D perovskite.

To confirm the long-term stability, we measured the I–V characteristics and X-ray diffraction (XRD) patterns of the halide perovskite based resistive switching devices under ambient conditions (relative humidity 40-60% at 25 °C) for a month. As a 2D perovskite layer that uses hydrophobic PEA⁺ cations for passivation can efficiently protect the 3D perovskite films from H₂O and O₂ under ambient conditions, the devices could maintain general bipolar resistive switching behavior without deviations for 28 days (Figures 4. 12 - 4. 14). On the other hand, the reset voltage deviation of the pristine 3D perovskite device is observed to increase because MAPbI₃ decomposes to MAI (g) and PbI₂(s) after only 7 days^{43,44}.

To understand the conduction mechanism of the 2D/3D perovskite device, we studied the *I-V* characteristics at various temperatures in the range of 243-333 K^{45,46}. The exponential plots of the I–V curves in Figure 4. 15a,b show that the pristine 3D and 2D/3D perovskite devices exhibited Ohmic contact behaviors with a linear slope of 1 in the LRS range at various temperatures. However, in the HRS range, the linear slopes gradually changed with an increase in temperature, indicating the hopping mechanism. We plotted the ion hopping activation energy^{34,47}, as shown in Figure 4. 15c. The thermally assisted ion hopping (TAH) is determined by the following

Expression;

$$J = \sigma_{TAH} E = n_c 2v_{TAH} a q_e \exp\left(\frac{\Delta H}{kT}\right) \sinh\left(\frac{q_e E a}{2kT}\right) \quad (1)$$

where n_c is the concentration of the majority carrier, q_e is the elementary charge, v is the frequency factor, and a is the ion hopping distance. We focused on the relationship between the ion hopping activation energy (ΔH) and temperature (T). In addition, this could follow an Ohm's law-type linear dependence of J for a low electric field, $E \ll kT/aq_e$, as below, as below;

$$J = \frac{n_c v T A H E}{kT} a^2 q_e^2 \exp\left(\frac{\Delta H}{kT}\right) \quad (2)$$

The ion-hopping activation energies were 0.135, and 0.150 eV for the pristine 3D perovskite and 2D/3D perovskite devices, respectively, as shown in Figure 4. 15c. This indicates that the 2D perovskite layer prevents the migration of the Ag ions as a conductive filament to the 3D perovskite film.

To further observe the Ag ion migration into the 3D perovskite film, we conducted time-of-flight secondary ion mass spectroscopy (TOF-SIMS) of the 3D and 2D/3D perovskite devices as the actual memory devices. Figure 4. 16 shows the ToF-SIMS 3D image of the Ag^- and PbI^- ion distributions on the halide perovskite-based devices for different endurance cycles. Small Ag ion distribution of the perovskite device is observed even at the fresh sample due to the instantaneous electric field by charged ions during the ion etching process⁴⁸.

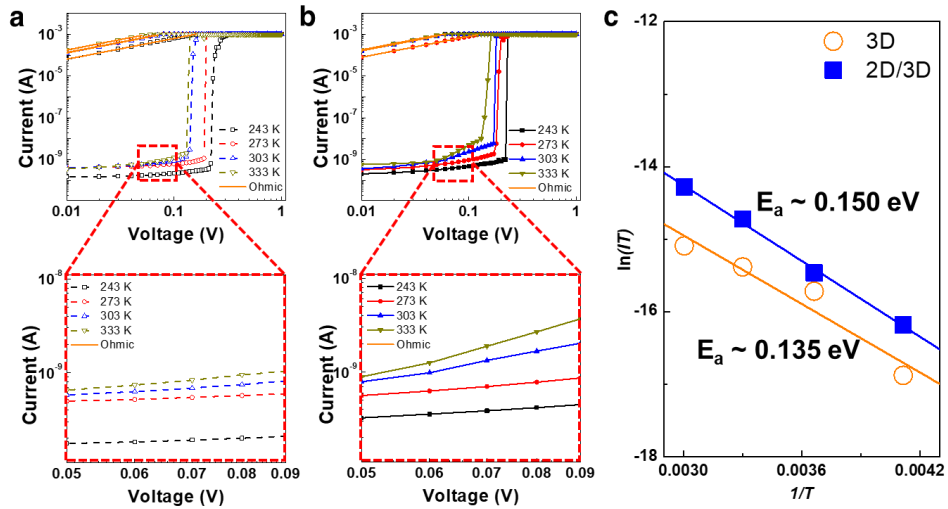


Figure 4.15. Conduction mechanism of halide perovskite -based resistive switching devices: (a,b) Logarithmic I - V characteristics of: (a) 3D perovskite and (b) 2D/3D perovskite films. (c) Thermally-assisted ion-hopping (TAH) activation energy is calculated at various temperatures.

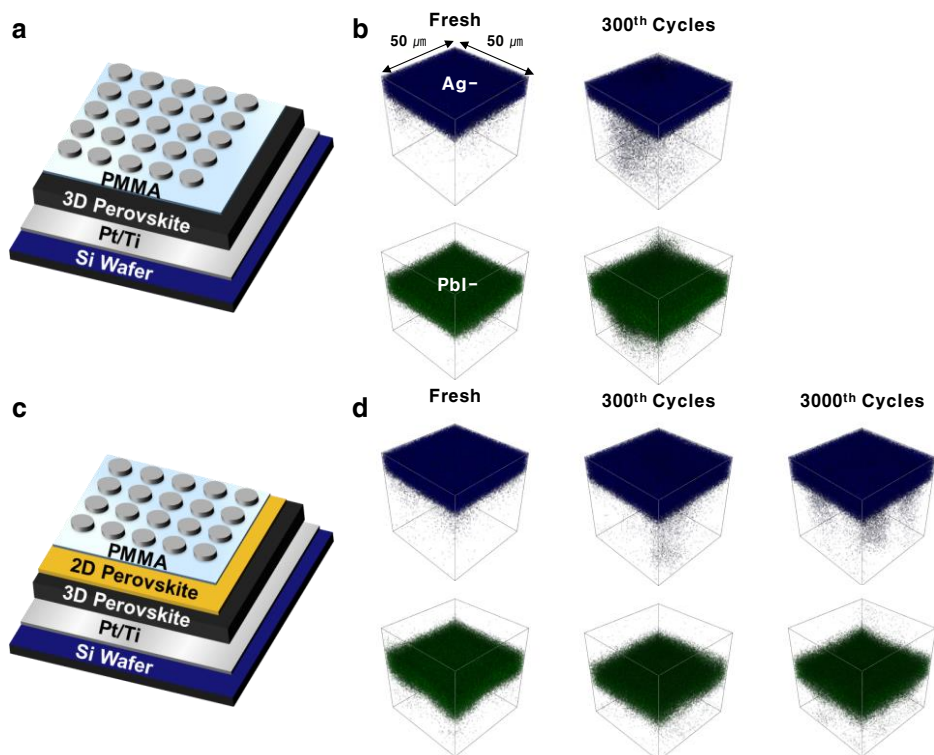


Figure 4. 16. (a,c) Schematic of halide perovskite -based resistive switching devices with: (a) 3D perovskite (c) 2D/3D perovskite. (b,d) ToF-SIMS 3D image results for halide perovskite-based resistive switching devices under different endurance cycles. Each 3D image is $50 \times 50 \times 0.5 \mu\text{m}$. (b) 3D perovskite (d) 2D/3D perovskite.

The Ag ion distribution of the 2D/3D perovskite device is observed to be much smaller/narrower than that of the pristine 3D perovskite device during the 300 cycles of endurance. The large Ag conductive filament lowers the endurance and causes instability because of its reaction with the halide perovskite films, such that the Ag filament would be stuck in an LRS⁴⁹. This is the reason why the 2D/3D perovskite device exhibits a long endurance of ~2700 cycles and long-term stability. Thus, the 2D perovskite layer can efficiently retard the Ag ion migration, which is consistent with the high ion hopping activation energy observed in Figure 4. 16. Furthermore, the migration of the Ag ions demonstrates that the resistive switching mechanism of the halide perovskite-based device is electrochemical metallization. However, the enhanced endurance of the 2D/3D perovskite devices cannot clearly be explained by only the filament size in the perovskite film. Recently, a few studies reported the improved endurance of oxide resistive switching devices by employing different thermally conductive materials^{32,50-52}. Therefore, we measured the thermal conductivity of the 3D perovskite and 2D perovskite films by the light flash technique, as shown in Figure 4. 17a. The 2D perovskite film exhibited a thermal conductivity of $1.18 \text{ W m}^{-1}\text{K}^{-1}$, which is 4 times higher than that of the 3D films ($0.28 \text{ W m}^{-1}\text{K}^{-1}$). To confirm this effect of the 2D perovskite film on the thermal conductivity, the rupture point was simulated using the COMSOL simulation on the 2D/3D perovskite films with 80 and 420 nm thicknesses, respectively⁵³⁻⁵⁵.

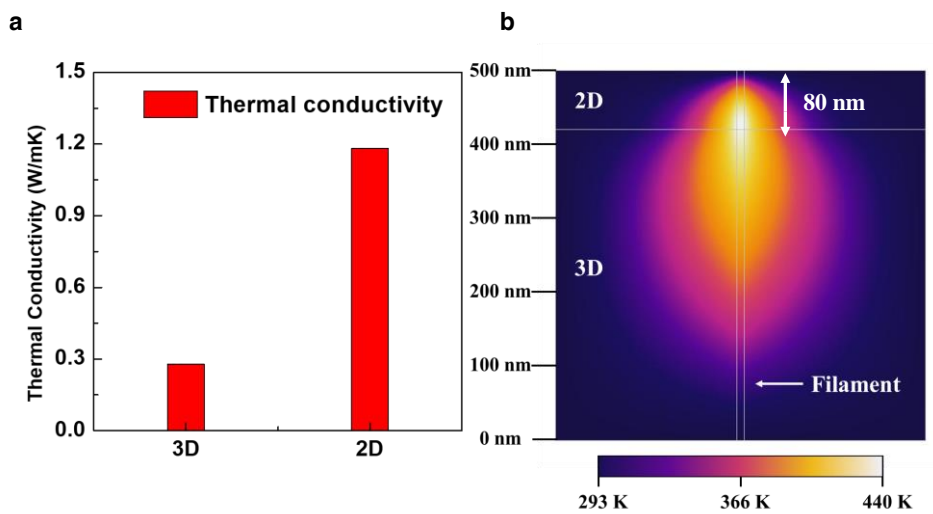


Figure 4. 17. (a) Thermal conductivity of 3D perovskite and 2D perovskite films. (b) COMSOL simulation result for the 2D/3D perovskite film.

The physical input parameters are summarized in Table 4. 1; the bias voltage is applied to the top electrode, while the bottom electrode is grounded. Thus, the current can only flow through the conductive filaments of the Ag ions on the perovskite film, resulting in inducing the local Joule heating at the filaments, as shown in Figure 4. 17b. The local Joule’s heating occurs around the 2D perovskite film due to its higher thermal conductivity than that of the 3D perovskite. Consequently, the high thermal energy accelerates the thermal diffusion of the Ag ions during the reset process at the 2D film. This indicates that the high thermal conductivity of the 2D perovskite film can help stabilize the rupture of the filament in the 2D/3D perovskite devices, which improves the endurance of the halide perovskite-based devices.

Table 4. 1. Physical input parameters used for the COMSOL simulation.

	Thermal Conductivity (w/mK)	Heat Capacity (J/kgK)	Density (g/cm ³)
Ag	406	233	10.5
3D Perovskite	0.28	333	4.16
2D Perovskite	1.18	559	1.58

4. 4. Conclusion

In summary, this report is the first on 2D/3D perovskite heterojunction films for resistive switching devices. The 2D/3D perovskite device exhibits an endurance of ~ 2700 cycles, which is about 9 times longer than that of the pristine 3D perovskite device. The comparatively high hopping activation energy of the 2D/3D perovskite device (0.150 vs 0.135 eV of 3D perovskite) checks the Ag ion migration into the 3D perovskite film, resulting in the formation of a narrow Ag conductive filament.

In addition, the 2D films exhibited a thermal conductivity of $1.18 \text{ W m}^{-1}\text{K}^{-1}$, which is about 4 times higher than that of the 3D films ($0.28 \text{ W m}^{-1}\text{K}^{-1}$); this could control the rupture of the Ag conductive filament during the reset process. Consequently, the 2D/3D perovskite was designed to significantly enhance the endurance and stability by controlling the Ag ion migration and filament rupture. Our results suggested that the 2D/3D perovskite film can improve the endurance of the halide perovskite-based resistive switching memory devices.

4. 5. Reference

- 1 S. Gao, F. Zeng, M. Wang, G. Wang, C. Song and F. Pan, *Sci. Rep.*, 2015, **5**, 15467.
- 2 J. J. Yang, M. D. Pickett, X. Li, D. A. A. Ohlberg, D. R. Stewart and R. S. Williams, *Nat. Nanotechnol.*, 2008, **3**, 429–433.
- 3 D. B. Strukov, G. S. Snider, D. R. Stewart and R. S. Williams, *Nature*, 2008, **453**, 80–83.
- 4 R. Waser and M. Aono, *Nat. Mater.*, 2007, **6**, 833–840.
- 5 F. Pan, S. Gao, C. Chen, C. Song and F. Zeng, *Mater. Sci. Eng. R Reports*, 2014, **83**, 1–59.
- 6 R. Waser, R. Dittmann, G. Staikov and K. Szot, *Adv. Mater.*, 2009, **21**, 2632–2663.
- 7 A. Sawa, *Mater. Today*, 2008, **11**, 28–36.
- 8 D.-H. Kwon, K. M. Kim, J. H. Jang, J. M. Jeon, M. H. Lee, G. H. Kim, X.-S. Li, G.-S. Park, B. Lee, S. Han, M. Kim and C. S. Hwang, *Nat. Nanotechnol.*, 2010, **5**, 148–153.

- 9 S. Yu, X. Guan and H.-S. P. Wong, *Appl. Phys. Lett.*, 2011, **99**, 063507.
- 10 M.-J. Lee, C. B. Lee, D. Lee, S. R. Lee, M. Chang, J. H. Hur, Y.-B. Kim, C.-J. Kim, D. H. Seo, S. Seo, U.-I. Chung, I.-K. Yoo and K. Kim, *Nat. Mater.*, 2011, **10**, 625–630.
- 11 Z. Yan, Y. Guo, G. Zhang and J.-M. Liu, *Adv. Mater.*, 2011, **23**, 1351–1355.
- 12 R. Yasuhara, T. Yamamoto, I. Ohkubo, H. Kumigashira and M. Oshima, *Appl. Phys. Lett.*, 2010, **97**, 132111.
- 13 A. Q. Jiang, C. Wang, K. J. Jin, X. B. Liu, J. F. Scott, C. S. Hwang, T. A. Tang, H. Bin Lu and G. Z. Yang, *Adv. Mater.*, 2011, **23**, 1277–1281.
- 14 M. Janousch, G. I. Meijer, U. Staub, B. Delley, S. E. Karg and B. P. Andreasson, *Adv. Mater.*, 2007, **19**, 2232–2235.
- 15 H. Kim, J. S. Han, J. Choi, S. Y. Kim and H. W. Jang, *Small Methods*, 2018, **2**, 1700310.

- 16 E. L. Unger, E. T. Hoke, C. D. Bailie, W. H. Nguyen, A. R. Bowring, T. Heumüller, M. G. Christoforo and M. D. McGehee, *Energy Environ. Sci.*, 2014, **7**, 3690–3698.
- 17 H.-S. Kim, C.-R. Lee, J.-H. Im, K.-B. Lee, T. Moehl, A. Marchioro, S.-J. Moon, R. Humphry-Baker, J.-H. Yum, J. E. Moser, M. Grätzel and N.-G. Park, *Sci. Rep.*, 2012, **2**, 591.
- 18 J. Choi, J. S. Han, K. Hong, S. Y. Kim and H. W. Jang, *Adv. Mater.*, 2018, **30**, 1704002.
- 19 J. Burschka, N. Pellet, S. J. Moon, R. Humphry-Baker, P. Gao, M. K. Nazeeruddin and M. Grätzel, *Nature*, 2013, **499**, 316–319.
- 20 N. J. Jeon, J. H. Noh, Y. C. Kim, W. S. Yang, S. Ryu and S. Il Seok, *Nat. Mater.*, 2014, **13**, 897–903.
- 21 H. Kim, J. S. Han, S. G. Kim, S. Y. Kim and H. W. Jang, *J. Mater. Chem. C*, 2019, **7**, 5226–5234.
- 22 J. Choi, S. Park, J. Lee, K. Hong, D.-H. Kim, C. W. Moon, G. Do Park, J. Suh, J. Hwang, S. Y. Kim, H. S. Jung, N.-G. Park, S. Han, K. T. Nam and H. W. Jang, *Adv. Mater.*, 2016, **28**, 6562–6567.

- 23 X. Guan, W. Hu, M. A. Haque, N. Wei, Z. Liu, A. Chen and T. Wu, *Adv. Funct. Mater.*, 2018, **28**, 1–11.
- 24 X. Zhao, H. Xu, Z. Wang, Y. Lin and Y. Liu, *InfoMat*, 2019, 183–210.
- 25 X. Zhu and W. D. Lu, *ACS Nano*, 2018, **12**, 1242–1249.
- 26 Y. Shan, Z. Lyu, X. Guan, A. Younis, G. Yuan, J. Wang, S. Li and T. Wu, *Phys. Chem. Chem. Phys.*, 2018, **20**, 23837–23846.
- 27 C. Wang, H. Wu, B. Gao, T. Zhang, Y. Yang and H. Qian, *Microelectron. Eng.*, 2018, **187–188**, 121–133.
- 28 S. Lee, J. H. Park, B. R. Lee, E. D. Jung, J. C. Yu, D. Di Nuzzo, R. H. Friend and M. H. Song, *J. Phys. Chem. Lett.*, 2017, **8**, 1784–1792.
- 29 B. Hwang and J. S. Lee, *Sci. Rep.*, 2017, **7**, 1–7.
- 30 G. E. Eperon, S. N. Habisreutinger, T. Leijtens, B. J. Bruijnaers, J. J. Van Franeker, D. W. Dequilettes, S. Pathak, R. J. Sutton, G. Grancini, D. S. Ginger, R. A. J. Janssen, A. Petrozza and H. J. Snaith, *ACS Nano*, 2015, **9**, 9380–9393.

- 31 J. You, L. Meng, T. Bin Song, T. F. Guo, W. H. Chang, Z. Hong, H. Chen, H. Zhou, Q. Chen, Y. Liu, N. De Marco and Y. Yang, *Nat. Nanotechnol.*, 2016, **11**, 75–81.
- 32 J. S. Han, Q. Van Le, J. Choi, K. Hong, C. W. Moon, T. L. Kim, H. Kim, S. Y. Kim and H. W. Jang, *Adv. Funct. Mater.*, 2018, **28**, 1705783.
- 33 S. Lee, J. Choi, J. B. Jeon, B. J. Kim, J. S. Han, T. L. Kim, H. S. Jung and H. W. Jang, *Adv. Electron. Mater.*, 2019, **5**, 1800586.
- 34 J. Choi, Q. Van Le, K. Hong, C. W. Moon, J. S. Han, K. C. Kwon, P.-R. Cha, Y. Kwon, S. Y. Kim and H. W. Jang, *ACS Appl. Mater. Interfaces*, 2017, **9**, 30764–30771.
- 35 C. Gu and J.-S. Lee, *ACS Nano*, 2016, **10**, 5413–5418.
- 36 J. S. Han, Q. Van Le, J. Choi, H. Kim, S. G. Kim, K. Hong, C. W. Moon, T. L. Kim, S. Y. Kim and H. W. Jang, *ACS Appl. Mater. Interfaces*, 2019, **11**, 8155–8163.
- 37 E. J. Yoo, M. Lyu, J.-H. Yun, C. J. Kang, Y. J. Choi and L. Wang, *Adv. Mater.*, 2015, **27**, 6170–6175.

- 38 Y. Hu, S. Zhang, X. Miao, L. Su, F. Bai, T. Qiu, J. Liu and G. Yuan, *Adv. Mater. Interfaces*, 2017, **4**, 1700131.
- 39 J.-Y. Seo, J. Choi, H.-S. Kim, J. Kim, J.-M. Yang, C. Cuhadar, J. S. Han, S.-J. Kim, D. Lee, H. W. Jang and N.-G. Park, *Nanoscale*, 2017, **9**, 15278–15285.
- 40 Y. Bai, S. Xiao, C. Hu, T. Zhang, X. Meng, H. Lin, Y. Yang and S. Yang, *Adv. Energy Mater.*, 2017, **7**, 1701038.
- 41 M.-H. Li, H.-H. Yeh, Y.-H. Chiang, U.-S. Jeng, C.-J. Su, H.-W. Shiu, Y.-J. Hsu, N. Kosugi, T. Ohgashi, Y.-A. Chen, P.-S. Shen, P. Chen and T.-F. Guo, *Adv. Mater.*, 2018, **30**, 1801401.
- 42 P. Chen, Y. Bai, S. Wang, M. Lyu, J.-H. Yun and L. Wang, *Adv. Funct. Mater.*, 2018, **28**, 1706923.
- 43 D. Li, S. A. Bretschneider, V. W. Bergmann, I. M. Hermes, J. Mars, A. Klasen, H. Lu, W. Tremel, M. Mezger, H.-J. Butt, S. A. L. Weber and R. Berger, *J. Phys. Chem. C*, 2016, **120**, 6363–6368.
- 44 A. M. Askar, G. M. Bernard, B. Wiltshire, K. Shankar and V. K. Michaelis, *J. Phys. Chem. C*, 2017, **121**, 1013–1024.

- 45 S. Menzel, S. Tappertzhofen, R. Waser and I. Valov, *Phys. Chem. Chem. Phys.*, 2013, **15**, 6945.
- 46 S. Menzel, P. Kaupmann and R. Waser, *Nanoscale*, 2015, **7**, 12673–12681.
- 47 T. Tsuruoka, K. Terabe, T. Hasegawa and M. Aono, *Nanotechnology*, 2011, **22**, 254013.
- 48 J. L. S. Lee, I. S. Gilmore, I. W. Fletcher and M. P. Seah, *Appl. Surf. Sci.*, 2008, **255**, 1560–1563.
- 49 M. Arita, A. Takahashi, Y. Ohno, A. Nakane, A. Tsurumaki-Fukuchi and Y. Takahashi, *Sci. Rep.*, 2015, **5**, 17103.
- 50 M. Barci, L. Perniola, G. Molas, C. Cagli, E. Vianello, M. Bernard, A. Roule, A. Toffoli, J. Cluzel and B. De Salvo, *IEEE J. Electron Devices Soc.*, 2016, **4**, 314–320.
- 51 D. Kumar, R. Aluguri, U. Chand and T.-Y. Tseng, *Appl. Phys. Lett.*, 2017, **110**, 203102.
- 52 K.-J. Gan, P.-T. Liu, Y.-C. Chiu, D.-B. Ruan, T.-C. Chien and S. M. Sze, *Surf. Coatings Technol.*, 2018, **354**, 169–174.

- 53 K. M. Kim, T. H. Park and C. S. Hwang, *Sci. Rep.*, 2015, **5**, 7844.
- 54 S. Dirkmann and T. Mussenbrock, *AIP Adv.*, 2017, **7**, 065006.
- 55 C.-C. Hsieh, A. Roy, Y.-F. Chang, D. Shahrjerdi and S. K. Banerjee,
Appl. Phys. Lett., 2016, **109**, 223501.

Chapter 5

MAPbBr₃ Halide Perovskite based Resistive Switching Devices using Electron Transport Layer for Long Endurance Cycles and Retention Times

5. 1. Introduction

Resistive random-access memories (ReRAMs) have been recognized as the most prospective non-volatile memory device for the next-generation because of their various advantages - low power consumption, high switching speed, high integration density, simple architecture, and low cost¹⁻⁷. Generally, ReRAM comprises a metal-insulator-metal (MIM) vertical structure, which is a two-terminal device. The insulator, resistive switching layer, provides a resistance state. Resistive switching phenomenon has been observed in several materials, for example, chalcogenides⁸, metal oxides⁹⁻¹⁴, organics¹⁵, and others¹⁶⁻¹⁹. However, there have been limitations for low-power and flexible devices because these require high-operation voltage and a high-temperature process.

Recently, halide perovskites have attracted significant attention since solar cells have been targeted as a prospective energy source²⁰⁻²³ due to their large light absorption coefficient, long carrier diffusion length, high carrier mobility, and so on²⁴⁻²⁷. Among these excellent properties, *I-V* hysteresis caused by ion migration is particularly thought to be the characteristic of memristive materials in ReRAM devices²⁸. Halide perovskites, which are ABX_3 structured compounds, consist of monovalent cations (CH_3NH_3 (MA), Cs,) in the A-site and divalent metal cations (Pb, Sn) in the B-site, and halide anions (I, Br, or Cl) in the X-site^{29,30}. Previously, $MAPbI_3$, $MAPbBr_3$, or $CsPbI_3$ based ReRAM devices have been studied³¹⁻³³. However, some critical issues need to be resolved even though the halide perovskites based ReRAM devices have been recognized as a potential research topic.

The general resistive switching of ReRAM occurred through the formation and rupture of conducting filaments, which accompanied a complex redox reaction. When the high initial resistance state (HRS) switches to a low resistance state (LRS) at the particular voltage (reset voltage), the formation of conducting filaments occurs, which means that the device is ON states^{34,35}. Following this process, LRS is changed to HRS at the opposite voltage (set voltage), indicating an OFF state^{35,36}. However, by repeatedly applying a bias polarity or voltage amplitude, conducting filaments are randomly formed and ruptured³⁷⁻³⁹. Eventually, resistive switching parameters, such as set and reset voltages or ON/OFF ratio distribution, display large fluctuation, which results in the degradation of switching uniformity and device performances.

To address these issues, 2,2',2''-(1,3,5-benzinetriyl)-tris(1-phenyl-1-H-benzimidazole), TPBI on the halide perovskite layer has been considered as a means of enhancing the endurance by controlling the conducting filament growth. Generally, TPBI is used as an electron transport layer (ETL) in halide perovskites based light-emitting diodes (LEDs)^{40,41}. By stacking a TPBI layer between the resistive switching layer and top electrode, it is thought that electrons are effectively injected into the halide perovskites switching layer.

In this work, we fabricated MAPbBr₃ based resistive switching memory devices by solution processing at low temperatures. The pure chloroform (CF) was applied as an anti-solvent, which increases the film's uniformity by reducing solvent evaporation time^{42,43}. To compare the TPBI layer 's dependence, TPBI was dissolved

in pure chloroform when the crystallization process of MAPbBr₃ was conducted. Both MAPbBr₃ based memory devices exhibited a high ON/OFF ratio of >10⁷ under an operation speed of 640 μs and low voltage operation. Furthermore, The MAPbBr₃ perovskite synthesized with TPBI in pure chloroform significantly enhanced the endurance from 90 cycles to more than 300 cycles.

5.2. Experimental section

Materials

1,3,5-tris(2-N-phenylbenzimidazolyl) benzene (TPBi) was purchased from OSM, and methylammonium bromide (MABr) was purchased from Greatcell Solar. Lead (II) bromide (PbBr_2) (99.999%), dimethyl sulfoxide (DMSO) (99.8%, anhydrous), chloroform (CF) (99%, anhydrous) were purchased from Sigma-Aldrich. All chemicals were used as received.

Fabrication of the memory devices

The 35 wt% of MAPbBr_3 precursor solution was prepared by mixing stoichiometric quantities of MABr and PbBr_2 in a molar ratio of 1.06:1 (MABr: PbBr_2) in DMSO, followed by stirring overnight. A uniform film was obtained by spin-coating the MAPbBr_3 precursor on various substrates (Pt, Si, SiO_2 , Si) with a speed of 3000 rpm, followed by the nanocrystal pinning method to induce the rapid crystallization and uniform morphology by dropping chloroform (CF) during the spin-coating process. For the additive-induced nanocrystal pinning method, 0.1 wt% of TPBi dissolved in CF solution was used instead.

After the spin-coating process, MAPbBr_3 film was annealed at 90 °C for 10 min. To complete the devices, Ag electrodes ($50 \mu\text{m} \times 50 \mu\text{m}$) were deposited by e-beam evaporation under 1×10^{-6} Torr at room temperature through a shadow mask.

Characterization

The surfaces and cross-sections of the MAPbBr₃ perovskite films were imaged using a field-emission scanning electron microscope (FE-SEM) (SUPRA 55VP, Carl Zeiss). The morphology of the perovskite films was analyzed using atomic force microscopy (AFM) (Park System XE100). Crystal structure of the perovskite film was analyzed by using x-ray photoelectron spectroscopy (XPS) (Korea Basic Science Institute, photon source: monochromatic Al-Kα at 1486.6 eV) and x-ray diffraction (XRD) (Rigaku, D/MAX-2500) measurement. Time-of-flight secondary ion mass spectroscopy (ToF-SIMS) experiments were performed with a ToF-SIMS 5 (ION-TOF GmbH, Münster, Germany) by using a pulsed 30 keV Bi⁺ primary beam with a current 0.64 pA. The electrical properties of the memory units were characterized by using an Agilent 4156C semiconductor analyzer in the direct current–voltage sweeping mode and alternating voltage pulse mode in a vacuum chamber (6×10^{-2} Torr).

5. 3. Results and Discussion

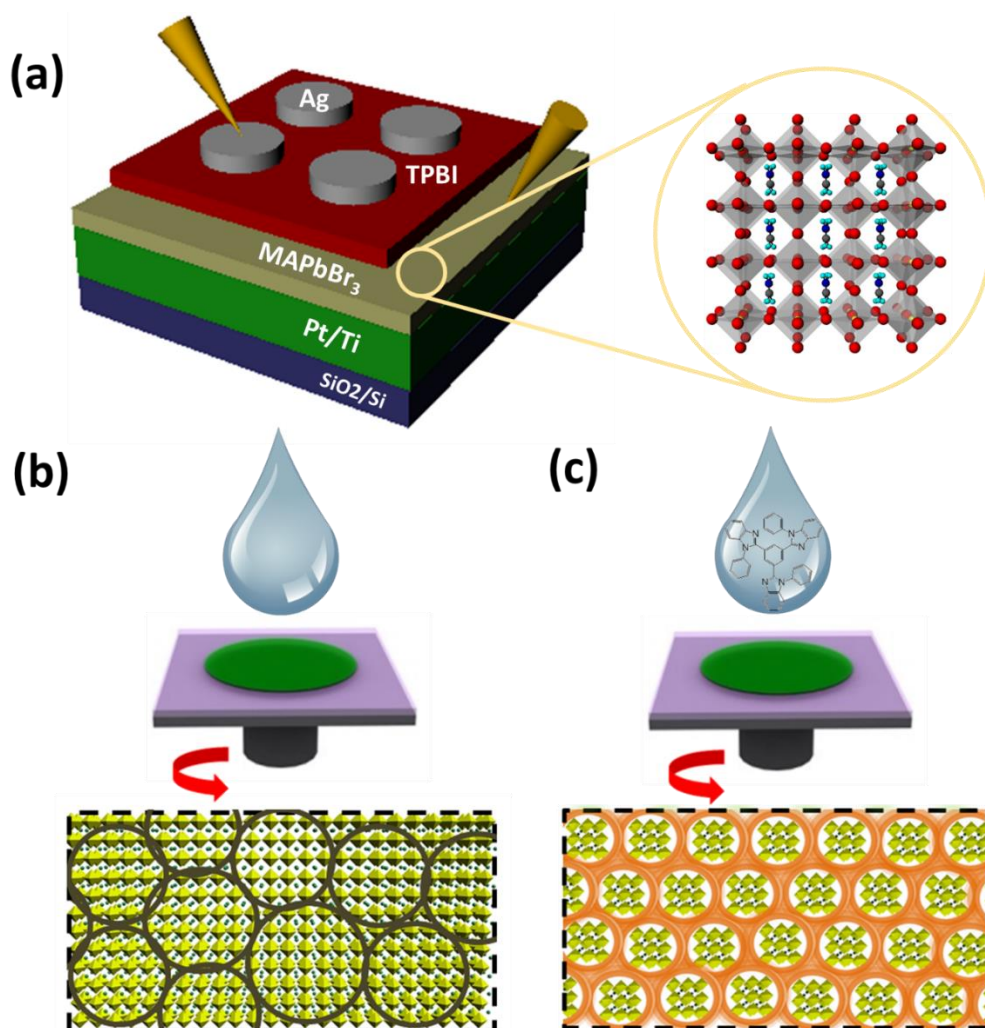


Figure 5. 1. Schematic illustration of the resistive memory device structure and resistive switching materials MAPbBr_3 (a). Synthesis processes of MAPbBr_3 by chloroform (b) and MAPbBr_3 by TPBI dissolved in chloroform (c).

Figure 5. 1(a) illustrates the vertical stack structure of the Ag top electrode/TPBI/MAPbBr₃/Pt bottom electrode/Ti/SiO₂/Si device and the schematic of the crystal structure of resistive switching material, MAPbBr₃. MA metal cations strongly interact with Br anions, making fast and easy crystallization of MAPbBr₃ during spin-coating. Thus, as shown in Figure 5. 1(b) and (c), MAPbBr₃ films were successfully synthesized under the low-temperature and all solution process by the spin-coating method. First, the precursor solution of MAPbBr₃ is dropped and spread over the Pt bottom electrode. Second, CF, a highly volatile nonpolar solvent, was fully covered and spin-coated to induce fast evaporation and crystallization of the MAPbBr₃ perovskite film. (Figure 5. 1(b)).⁴³ Also, to confirm the effect of electron-transporting material, TPBI dissolved in CF was dripped, as depicted in Figure 5. 1(c). Subsequently, Ag top electrodes were deposited by an electron beam evaporator on the switching layer through a dot-patterned shadow mask to define the device area.

To confirm the uniformity of these layers, we observed the perovskite surfaces. Figure 5. 2(a) and (b) shows scanning electron microscopy (SEM) images of the MAPbBr₃ by CF (MAPbBr₃:CF) and MAPbBr₃ by TPBI dissolved in CF (MAPbBr₃:TPBI) synthesized on Pt-coated silicon substrates. The extremely thin TPBI layer slightly covers the MAPbBr₃ surface and its grain boundary areas.

For both samples, the thicknesses were about 280 nm, as shown in Figure 5. 2(c) and (d). The average grain size of MAPbBr₃:TPBI film is approximately 102.38nm with perfect surface coverage, whereas that of MAPbBr₃:CF film is about 184.09 nm.

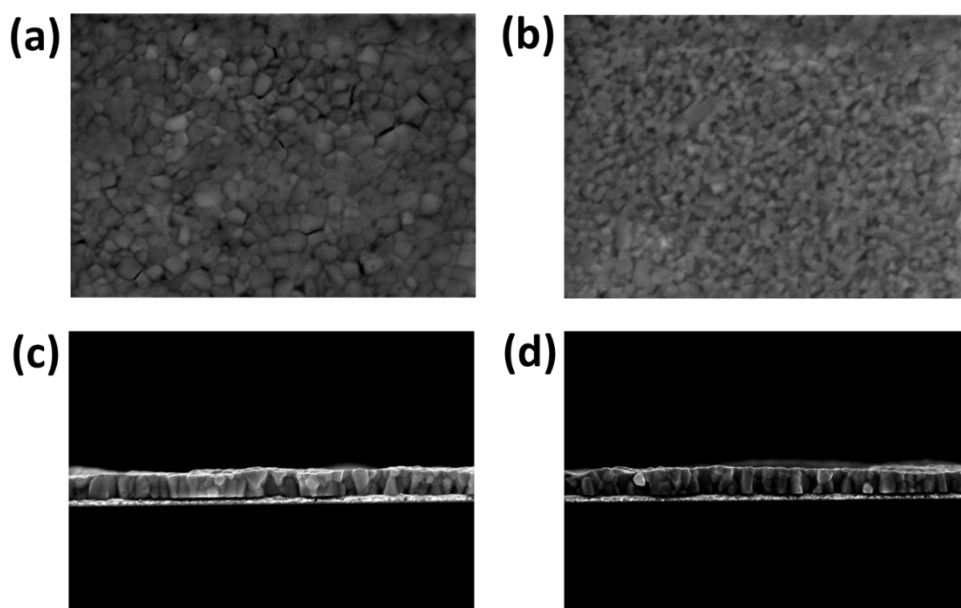


Figure 5. 2. Planar-view SEM images of the MAPbBr₃:CF (a) and MAPbBr₃:TPBI(b). Cross-sectional SEM images of the MAPbBr₃:CF (c) and MAPbBr₃:TPBI(d).

As shown in Figure 5. 3(a) and (b), the grain size distribution of MAPbBr₃: TPBI is concentrated at around 50-300 nm, whereas that of MAPbBr₃:CF showed a broader range from 50 nm to 450 nm. It is suspected that TPBI impeded crystal growth during the nanocrystal pinning process. The TPBI molecules positioned at grain boundaries effectively hinder the bonding interaction between MAPbBr₃ grains during continuous crystallization, which results in the reduction of grain size.^{43,44}

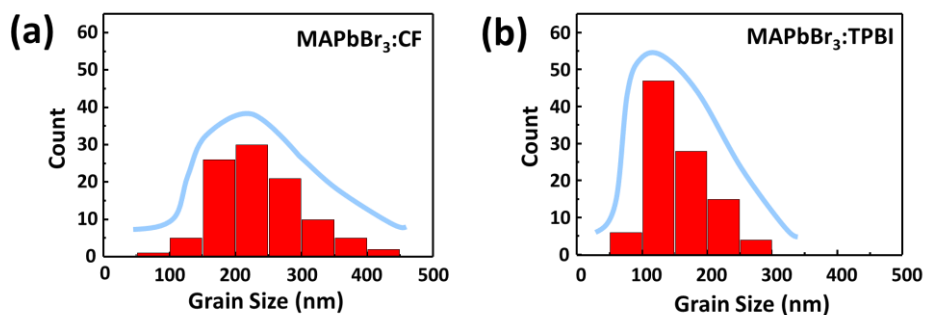


Figure 5. 3. Grain size distribution of MAPbBr₃:CF (a) and MAPbBr₃:TPBI (b) films.

X-ray diffraction (XRD) patterns were measured to analyze crystal structures of MAPbBr_3 for $\text{MAPbBr}_3:\text{CF}$ and $\text{MAPbBr}_3:\text{TPBI}$ samples. As shown in Figure 5. 4(a), the XRD pattern of the $\text{MAPbBr}_3:\text{CF}$ sample monitored in the 2θ range of $10-60^\circ$, showing sharp peaks of (100), (110), (200), (210), (211), (220), and (300) planes at 15.02° , 21.3° , 30.28° , 33.92° , 37.24° , 43.28° , and 46.00° , respectively. It indicates that these patterns are consistent with cubic perovskite phases.^{45,46} Also, peak positions of $\text{MAPbBr}_3:\text{TPBI}$ film are the same as those of $\text{MAPbBr}_3:\text{CF}$ with no additional and changed peaks, in Figure 5. 4(b). This stability in peak positions indicates the addition of TPBI does not influence the crystal structures of MAPbBr_3 during continuous crystallization.

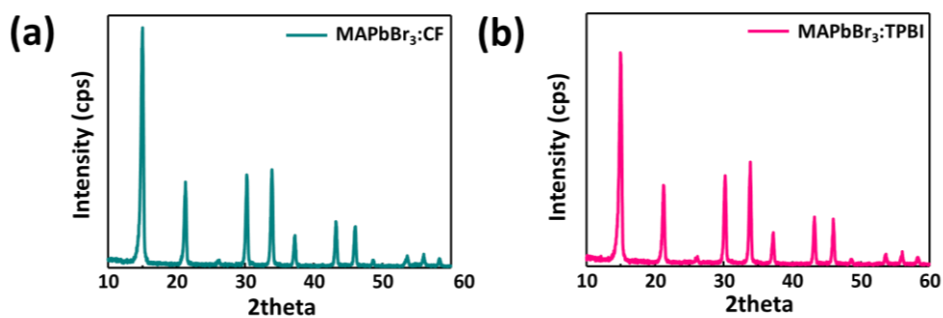


Figure 5. 4. XRD pattern in the 2θ range of $10-60^\circ$ of $\text{MAPbBr}_3:\text{CF}$ (a) and $\text{MAPbBr}_3:\text{TPBI}$ (b) films.

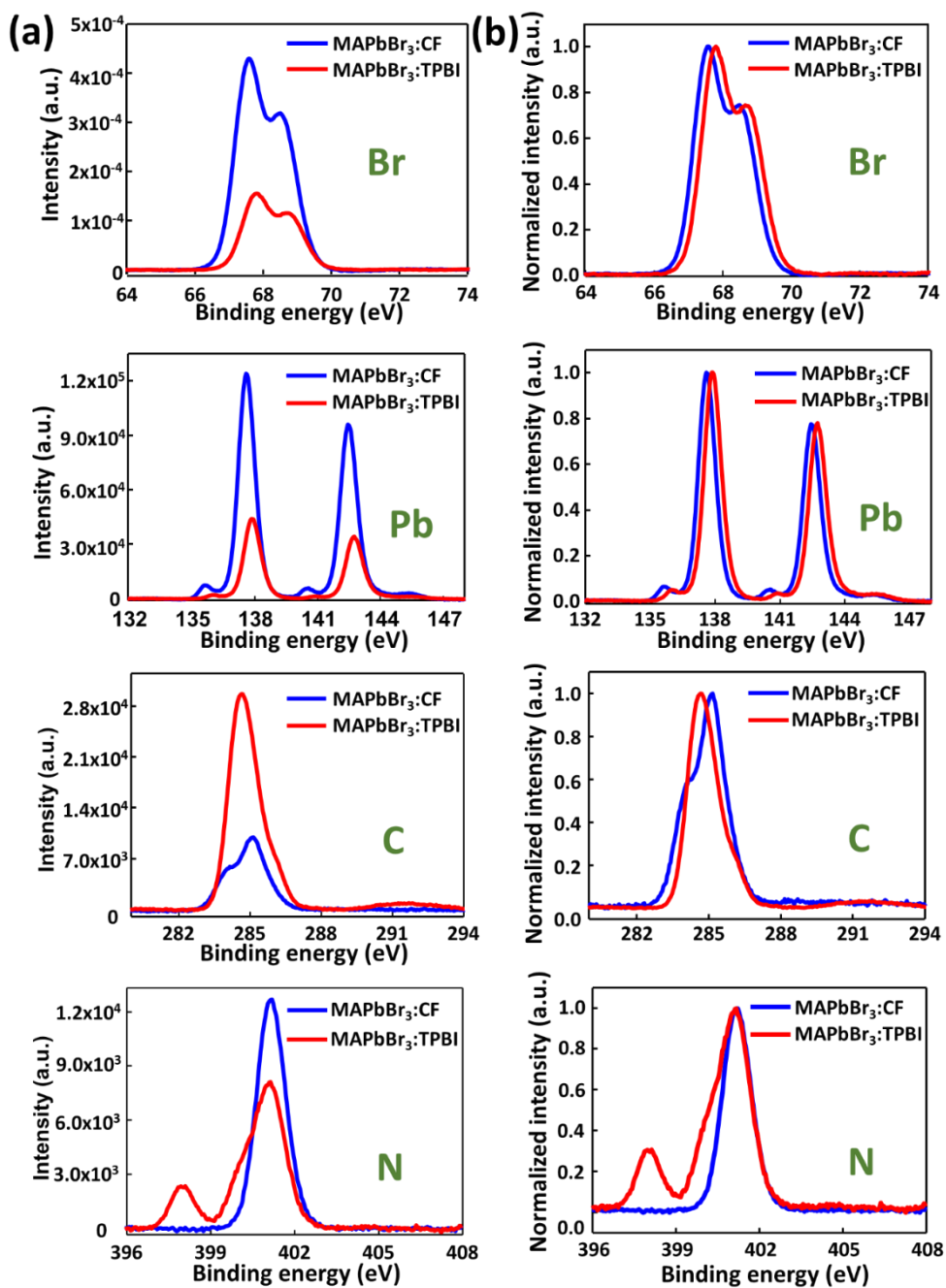


Figure 5. XPS spectra to exhibit core level peaks of the elemental compositions (a) and their normalized data (b).

In Figure 5. 5(a) and (b), X- ray photoelectron spectroscopy (XPS) spectra exhibit core level peaks of the elemental compositions of the MAPbBr₃:CF and MAPbBr₃:TPBI films. Compared with peak intensities including Br, Pb, and N (except the C core level) of MAPbBr₃:CF sample, those of MAPbBr₃:TPBI were relatively lower, which demonstrates that the TPBI part located between grains was detected. Furthermore, both films similarly show strong peaks of Br (~68 eV), Pb (~138 and 143 eV), and C (~285 eV) without additional peaks. However, the binding energy peaks of N (~401 eV) composition has the shoulder peak detected by TPBI, as observed in XPS of N. Because both MAPbBr₃ and TPBI are consisted N composition in common, binding energy peaks of N were co-detected by MAPbBr₃ and TPBI parts, resulting in broader and additional peaks.

Therefore, the crystal structures of MAPbBr₃ are not affected by TPBI treatment even though relative intensities decrease and the additional binding energy peak is observed in XPS spectra.

To further understand the distribution of TPBI into the MAPbBr₃ perovskite layer, we observed time-of-flight secondary ion mass spectroscopy (TOF-SIMS) measurement of the MAPbBr₃:CF and MAPbBr₃:TPBI film. TOF-SIMS depth profiles of each TPBI, Pb, and Br are shown in Figure 5. 6(a) and (b) to examine relative TPBI concentration within the MAPbBr₃ layer.

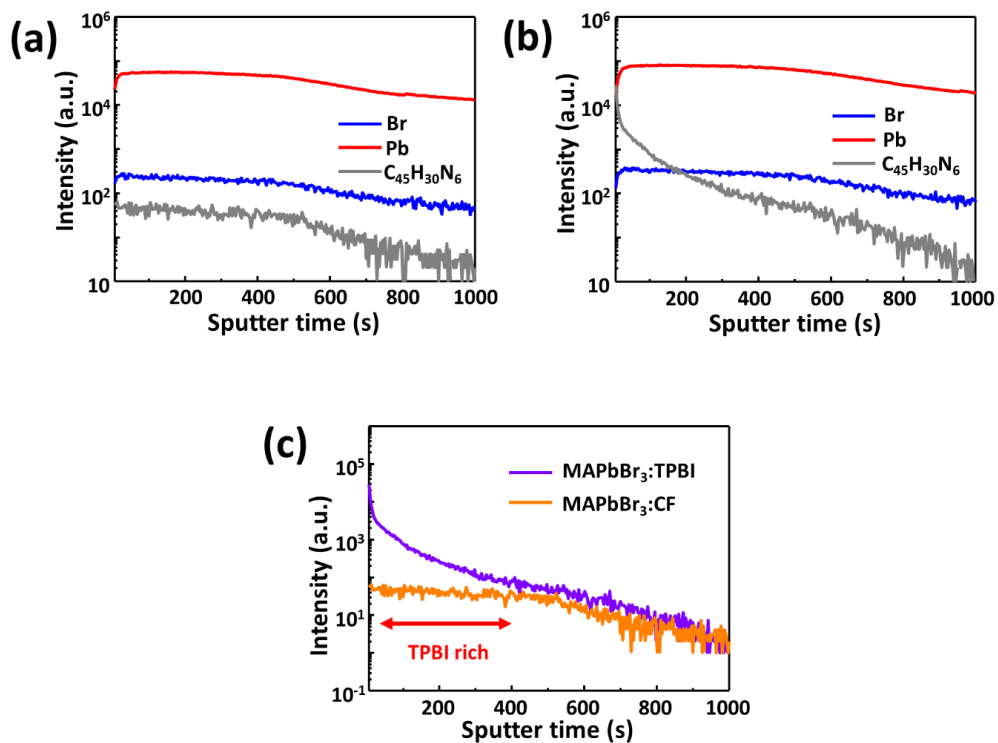


Figure 5. 6. TOF-SIMS measurement of the MAPbBr₃:CF (a) and MAPbBr₃:TPBI (b) film. (c) Comparison of the TPBI distribution profiles in MAPbBr₃:CF and MAPbBr₃:TPBI film.

In the MAPbBr₃:CF and MAPbBr₃:TPBI film, the distribution of TPBI is significantly different at the surface of MAPbBr₃ perovskite layers. Compared with the MAPbBr₃:CF sample, TPBI was predominately distributed on the MAPbBr₃:TPBI surface. Then, it was diffused toward the grain boundaries and gradually decreased in the depth direction. Figure 5. 6(c) shows the comparison of the TPBI distribution profiles in MAPbBr₃:CF and MAPbBr₃:TPBI film. This result suggests that the TPBI layer was spread at the surface of the area, directly influencing the resistive switching behavior of the MAPbBr₃ based memory devices.

To confirm the programmable switching behaviors of the MAPbBr₃:CF- and MAPbBr₃:TPBI -based memory devices, the *I*–*V* measurement of both devices were conducted under direct current (DC) voltage bias sweep.

Figure 5. 7 shows the typical current-voltage sweeps of the Ag/MAPbBr₃/Pt (MAPbBr₃:CF) (a) and Ag/TPBI/MAPbBr₃/Pt (MAPbBr₃:TPBI)(b) devices. The voltage was applied to the top electrode (Ag), and the bottom electrode (Pt) was grounded. In these devices, the electrochemical metallization (ECM) mechanism was observed. The ECM mechanism means that the dissolved metal cation by oxidation of the active top electrode forms a conducting filament passing through the resistive switching layers.⁴⁶ Both devices also show bipolar resistive switching with a set and a reset, which means that ON/OFF behavior happened at opposite polarities.^{3,17} The ON/OFF resistive switching operation for these halide perovskite memory devices is defined by the SET and RESET processes. The SET process

occurs when a high resistance state (HRS) abruptly changes to a low resistance state (LRS) at a certain voltage, which refers to the "ON state". Following the SET process, LRS abruptly decreases to HRS when the opposite voltage is applied to the device for the RESET process, which is called the "OFF state".⁴⁷

In these MAPbBr₃ based memory devices, as seen in Figure 5. 7(a) and (b), ON state was dramatically occurred by changing the 10⁻¹⁰ A of low current state to the 10⁻³ A of the high current state at a SET operating voltage of +0.50 V. As a result, conducting filaments are formed. The abruptly increased current, which means LRS, can be sustained during ON state by a compliance current (CC) of 10⁻³ A. The current is generally limited through (CC) during the set process to avoid device damages.

Subsequently, the 10⁻³ A of the high current state was decreased to the 10⁻¹⁰ A of the low current state, changing the resistance of the perovskite layer. This RESET process happened at -0.20 V. The current changes to HRS can be sustained during the OFF state by rupture of the conducting filaments.

Thus, the ON/OFF ratio for these MAPbBr₃ based memory devices was as high as a~10⁷. However, we confirmed that MAPbBr₃:CF devices show unstable switching behaviors (Figure 5. 7(a)) during the RESET process, compared that MAPbBr₃:TPBI devices smoothly operated(Figure 5. 7(b)).

The resistive switching phenomena can be attributed to the application of TPBI used as an electron transport material. When a negative voltage is applied to the device,

the rupture of Ag conducting filaments is induced by Joule-heating-assisted oxidation.^{33,48–50} Figure 5. 7(a) shows that the I - V curves in the RESET show irregular shapes, which indicates the residual filaments remain in the switching layer after the current decrease. By stacking a TPBI to MAPbBr₃, electrons are effectively injected into the switching layer, which results in the oxidation of Ag conducting filaments can be easily occurred. Therefore, as shown in Figure 5. 7(b), it reveals that the RESET process of MAPbBr₃:TPBI device is stably operated.

We also confirmed the reliability of these resistive switching memory devices by assessing the switching endurance defined by the stability of the number of switching cycles.

Figure 5. 7(c) and (d) show the endurance characteristics to test cycle-to-cycle reproducibility and stability of MAPbBr₃:CF and MAPbBr₃:TPBI memory device through the alternating current (AC) voltage pulses. The resistance values were measured by continuous write/erase pulses of +1.0 V for the ON state and -3.0 V for the OFF state under with and a read voltage of +0.05 V with a 640 μ s pulse duration. For the MAPbBr₃:CF device in Figure 5. 7(c), only 90 cycles of HRS and LRS were sustained, and after that, obvious fail of HRS was observed. This degradation can be thought to be due to the random and incomplete reset at the MAPbBr₃ interface. However, as shown in Figure 5. 7(d), the endurance of the MAPbBr₃:TPBI memory device was extended to ~300 cycles, maintaining ON/OFF ratios above 10^7 . During the RESET process, TPBI between the MAPbBr₃ switching

layer and top electrode could play a key role in inciting conductive filament rupture due to effective injection of electrons for the oxidation of Ag filaments edges.

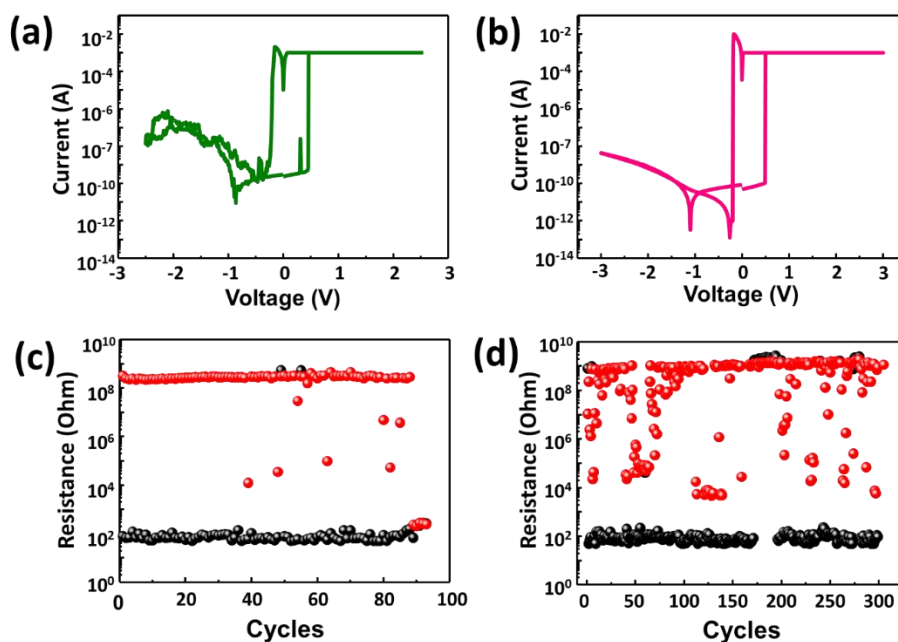


Figure 5. 7. Typical current-voltage sweeps of the Ag/MAPbBr₃/Pt (MAPbBr₃:CF) (a) and Ag/TPBI/MAPbBr₃/Pt (MAPbBr₃:TPBI) (b) devices. Endurance characteristics of the Ag/MAPbBr₃/Pt (MAPbBr₃:CF) (c) and Ag/TPBI/MAPbBr₃/Pt (MAPbBr₃:TPBI) (d) devices.

To better understand the TPBI roles to MAPbBr₃ layers, proposed ON and OFF mechanisms for the Ag conducting filaments behavior of the devices are shown in Figure 5. 8 (a) and (b). The enhanced resistive switching behavior of the MAPbBr₃:TPBI device compared with the MAPbBr₃:CF device can be well explained by the existence of TPBI, which is modulated by the effective injection of electrons from the Ag/MAPbBr₃ interface.

According to the electrochemical metallization theory, conducting filaments are formed by the three steps: 1) oxidation of the electrochemically Ag top electrode, 2) the injection of the Ag cation to switching layer, and 3) reduction of the Ag cation and growth of Ag conducting filaments. In this process, TPBI increases electron transport capacity, which induces nucleation of Ag atoms and the growth of conducting filaments at the interface of MAPbBr₃.⁵¹⁻⁵⁴ Also, Ag conducting filaments are ruptured by negative bias, and Ag cations migrate away from the remaining filaments. In this process, TPBI accelerates the filament rupture at the interface of MAPbBr₃ by withdrawing the electrons by negative bias from the top electrode.

Figure 5. 9 shows the resistive switching performance of the MAPbBr₃:TPBI device in detail. As shown in Figure 5. 9(a), an electroforming behavior referred to as a soft breakdown in the MAPbBr₃ layer was observed at the initial sweep, which can accomplish stable switching properties.⁵⁵⁻⁵⁷

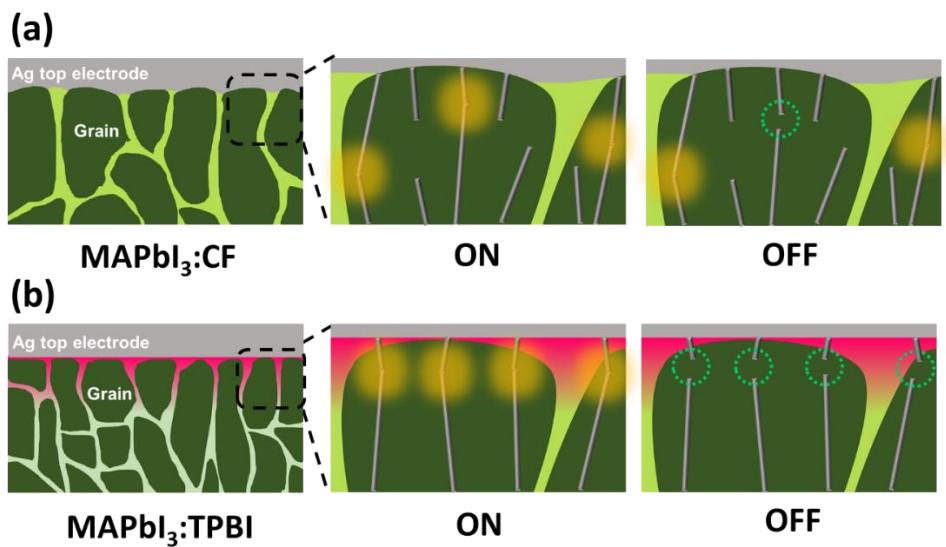


Figure 5. 8. ON and OFF mechanisms for the Ag conducting filaments behavior of the Ag/MAPbBr₃/Pt (MAPbBr₃:CF) (a) and Ag/TPBI/MAPbBr₃/Pt (MAPbBr₃:TPBI) (b) devices.

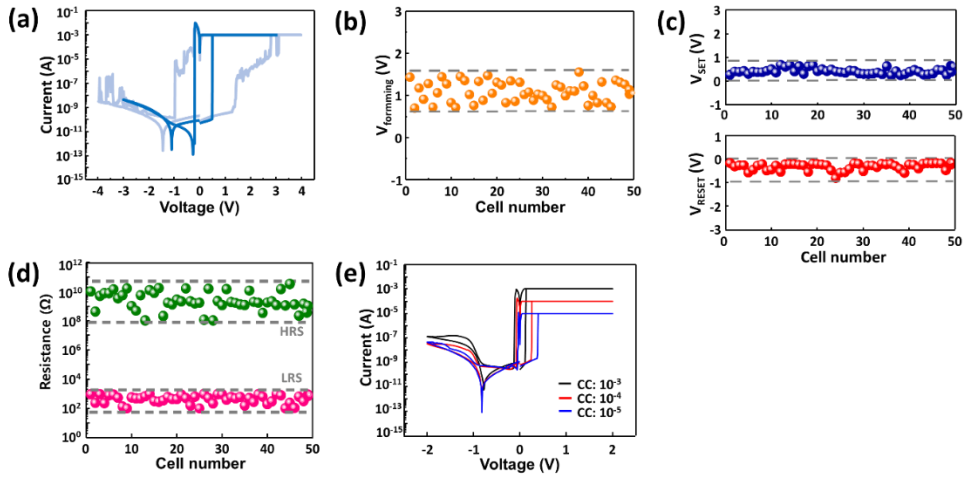


Figure 5. 9. (a) Electroforming behavior of Ag/TPBI/MAPbBr₃/Pt devices. (b) Forming voltage distribution of Ag/TPBI/MAPbBr₃/Pt devices. (c) SET and RESET voltage distributions of Ag/TPBI/MAPbBr₃/Pt devices. (d) HRS and LRS values for 50 Ag/TPBI/MAPbBr₃/Pt devices. (e) Multilevel resistive switching behavior Ag/TPBI/MAPbBr₃/Pt device.

In the memory device, electroforming gradually occurred after +1.50 V, then conducting filament bridge was completely formed at +3.0 V. Followed by this one cycle, the SET process could operate at a lower voltage than that of the electroforming. The phenomenon can be explained by the already-formed filament path during electroforming behavior, making Ag metal cations efficiently easier to pass through the switching layer during SET operation, even at a low voltage.^{46,58,59}

To evaluate the operational uniformity of the MAPbBr₃:TPBI device, forming, SET, and RESET voltage distributions are statistically analyzed for Ag/TPBI/MAPbBr₃/Pt cells. In Figures 5. 9(b) and (c), it is certainly seen that the no significant and meaningful deviation in the forming the SET and RESET voltage distributions for the different 50 cells. As displayed in Figure 5. 9(d), the HRS and LRS values for 50 different cells were measured. From the distributions, we could confirm that ON/OFF values are similar without absolute changes, which indicates that Ag/TPBI/MAPbBr₃/Pt device is superior to reproducibility.

In addition, multilevel resistive switching behavior was tested to explore the ability of the high data storage density for MAPbBr₃:TPBI based memory device. In Figure 5. 9(e), when the CC was applied from 1 mA to 10 μ A, three distinct LRS levels are observed. As the CC decreased, the resistance value of the LRS increased, while there was no change of HRS level by different CC. Thus, MAPbBr₃:TPBI device can store multi-data levels in one cell, which can fulfill the memory capacity increases.

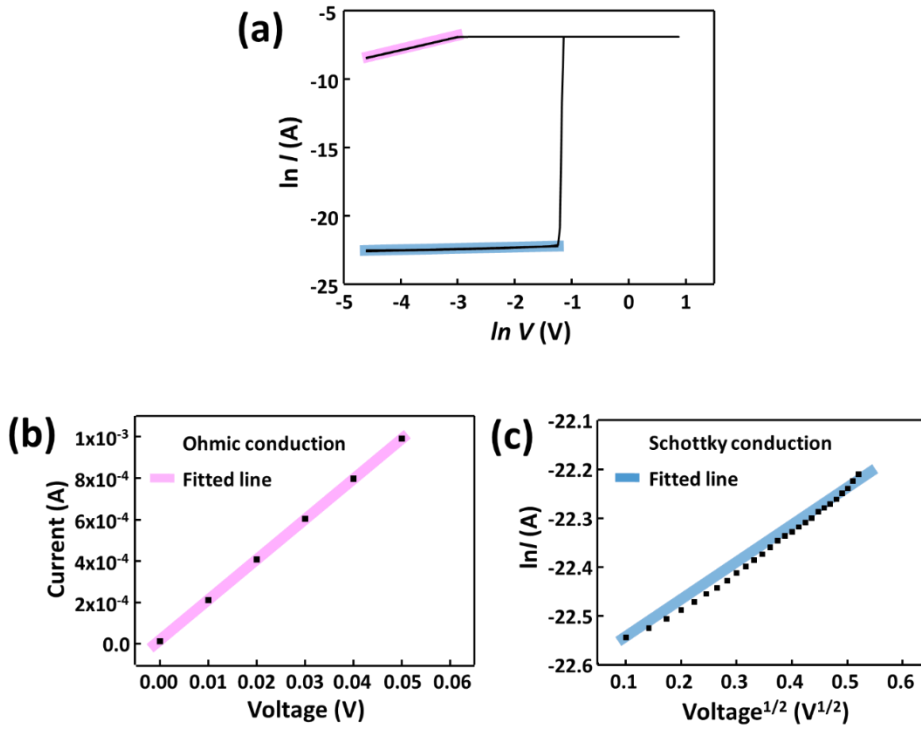


Figure 5. 10. (a) Typical I – V curves were plotted by double-logarithmic scales ($\ln I$ vs. $\ln V$). Ohmic conduction in the LRS verified by the linear fitting of the proportional relation of current to the voltage. (c) HRS region replotted with $\ln I \propto V^{1/2}$ to verify whether Schottky emission.

In order to elucidate the switching mechanism of the MAPbBr₃:TPBI device, the current transport mechanisms were analyzed. In Figure 5. 10 (a), the typical $I-V$ curves were plotted by double-logarithmic scales ($\ln I$ vs. $\ln V$). In the LRS range, the MAPbBr₃:TPBI device exhibited Ohmic conduction with a linear slope of 0.96 after the abrupt current increase.⁶⁰⁻⁶⁴ However, it was found that the non-linear slope of 0.12 means that the Schottky emission is dominant In the HRS range.^{33,65}

To further understand the Ohmic conduction and Schottky emission, $I-V$ curves of the LRS and HRS were respectively replotted with linear fitting lines. As shown in Figure 5. 10 (b), Ohmic conduction in the LRS was verified by the linear fitting of the proportional relation of current to the voltage ($I \propto V$).⁶³ It explains that the conduction mechanisms in the LRS region are governed by Ohmic conduction governed the LRS, indicating that Ag conducting filament passes through the MAPbBr₃ switching layer after abrupt formation of the filaments. Also, the $I-V$ curve in the HRS region was replotted with $\ln I \propto V^{1/2}$ to verify whether Schottky emission is dominant. In Figure 5. 10 (c), a linear relationship of $\ln I \propto V^{1/2}$ plot demonstrates that Schottky emission is dominant, determined by the following expression.⁶⁵

$$\ln I \propto \sqrt{\frac{q^3}{4\pi\epsilon d} kT} \times \sqrt{V} \quad (1),$$

Here, I is the current density, q is the electric charge, ϵ is the dielectric constant, d is the film thickness, K is the Boltzmann constant, T is the absolute temperature, and V is the applied voltage. The linearity of the replotted graph explains that the Ag metal cations can overcome the energy barrier, which results in the dissolution of them from the Ag top electrode.^{66,67}

5. 4. Conclusion

In summary, TPBI, an electron transfer material in LEDs, was introduced into MAPbBr₃ to achieve long-endurance cycles and retention time in ReRAM devices. Resistive switching properties in the ReRAM device with the Ag/TPBI/MAPbBr₃/Pt are induced by Ag filaments' formation and rupture in the MAPbBr₃ layer. The MAPbBr₃:TPBI device showed longer endurance cycles of 300, which is four orders of magnitude higher than that of the MAPbBr₃:CF memory device. Because TPBI makes electrons effectively inject into the switching layer, the oxidation of Ag conducting filaments can occur more efficiently, which is beneficial to the rupture of Ag filaments. In addition, the retention time for the ON and OFF states was evaluated to test the electrical reliability of the MAPbBr₃ memory device. Hence, this work has its value in terms of an alternate strategy for upgrading the switching property of halide perovskite memory devices.

5. 5. Reference

- 1 Z. S. Su, M. K. Fung, C. S. Lee, W. L. Li and S. T. Lee, *Appl. Phys. Lett.*, 2008, **93**, 083301.
- 2 J. Joshua Yang, F. Miao, M. D. Pickett, D. A. A. Ohlberg, D. R. Stewart, C. N. Lau and R. S. Williams, *Nanotechnology*, 2009, **20**, 215201.
- 3 A. Prakash, D. Jana and S. Maikap, *Nanoscale Res. Lett.*, 2013, **8**, 418.
- 4 D.-H. Kwon, K. M. Kim, J. H. Jang, J. M. Jeon, M. H. Lee, G. H. Kim, X.-S. Li, G.-S. Park, B. Lee, S. Han, M. Kim and C. S. Hwang, *Nat. Nanotechnol.*, 2010, **5**, 148–153.
- 5 M.-J. Lee, C. B. Lee, D. Lee, S. R. Lee, M. Chang, J. H. Hur, Y.-B. Kim, C.-J. Kim, D. H. Seo, S. Seo, U.-I. Chung, I.-K. Yoo and K. Kim, *Nat. Mater.*, 2011, **10**, 625–630.
- 6 R. Yasuhara, T. Yamamoto, I. Ohkubo, H. Kumigashira and M. Oshima, *Appl. Phys. Lett.*, 2010, **97**, 132111.
- 7 A. Q. Jiang, C. Wang, K. J. Jin, X. B. Liu, J. F. Scott, C. S. Hwang, T. A. Tang, H. Bin Lu and G. Z. Yang, *Adv. Mater.*, 2011, **23**, 1277–1281.
- 8 J. van den Hurk, I. Valov and R. Waser, *Thin Solid Films*, 2013, **527**, 299–302.

- 9 D. Panda, C.-Y. Huang and T.-Y. Tseng, *Appl. Phys. Lett.*, 2012, **100**, 112901.
- 10 H.-W. Yun, H. K. Woo, S. J. Oh and S.-H. Hong, *Curr. Appl. Phys.*, 2020, **20**, 288–292.
- 11 R. Yang and X. Li, *Phys. status solidi*, 2011, **208**, 1041–1046.
- 12 D. Ielmini, F. Nardi and C. Cagli, *Nanotechnology*, 2011, **22**, 254022.
- 13 Y. Tao, W. Ding, Z. Wang, H. Xu, X. Zhao, X. Li, W. Liu, J. Ma and Y. Liu, *Appl. Surf. Sci.*, 2018, **440**, 107–112.
- 14 Y. Huang, Z. Shen, Y. Wu, X. Wang, S. Zhang, X. Shi and H. Zeng, *RSC Adv.*, 2016, **6**, 17867–17872.
- 15 S. Song, B. Cho, T.-W. Kim, Y. Ji, M. Jo, G. Wang, M. Choe, Y. H. Kahng, H. Hwang and T. Lee, *Adv. Mater.*, 2010, **22**, 5048–5052.
- 16 J. Choi, J. S. Han, K. Hong, S. Y. Kim and H. W. Jang, *Adv. Mater.*, 2018, **30**, 1704002.
- 17 J. Choi, Q. Van Le, K. Hong, C. W. Moon, J. S. Han, K. C. Kwon, P.-R. Cha, Y. Kwon, S. Y. Kim and H. W. Jang, *ACS Appl. Mater. Interfaces*, 2017, **9**, 30764–30771.
- 18 X. Zhao, H. Xu, Z. Wang, L. Zhang, J. Ma and Y. Liu, *Carbon N. Y.*, 2015, **91**, 38–44.

- 19 K.-H. Kim, S. Hyun Jo, S. Gaba and W. Lu, *Appl. Phys. Lett.*, 2010, **96**, 053106.
- 20 M. A. Green, A. Ho-Baillie and H. J. Snaith, *Nat. Photonics*, 2014, **8**, 506–514.
- 21 H. Kim, G. Veerappan and J. H. Park, *Electrochim. Acta*, 2014, **137**, 164–168.
- 22 H. Kim, G. Veerappan, D. H. Wang and J. H. Park, *Electrochim. Acta*, 2016, **187**, 218–223.
- 23 J. W. Jo, Y. Yoo, T. Jeong, S. Ahn and M. J. Ko, *Electron. Mater. Lett.*, 2018, **14**, 657–668.
- 24 Q. Chen, N. De Marco, Y. (Michael) Yang, T.-B. Song, C.-C. Chen, H. Zhao, Z. Hong, H. Zhou and Y. Yang, *Nano Today*, 2015, **10**, 355–396.
- 25 D. B. Mitzi, *J. Chem. Soc. Dalt. Trans.*, 2001, 1–12.
- 26 L. N. Quan, M. Yuan, R. Comin, O. Voznyy, D. H. Kim and E. H. Sargent, *SPIE Newsroom*, , DOI:10.1117/2.1201608.006639.
- 27 G. Kieslich, S. Sun and A. K. Cheetham, *Chem. Sci.*, 2014, **5**, 4712–4715.
- 28 C. Gu and J.-S. Lee, *ACS Nano*, 2016, **10**, 5413–5418.

- 29 H. Kim, J. S. Han, J. Choi, S. Y. Kim and H. W. Jang, *Small Methods*, 2018, **2**, 1700310.
- 30 H. Kim, K. A. Huynh, S. Y. Kim, Q. Van Le and H. W. Jang, *Phys. status solidi – Rapid Res. Lett.*, 2019, **3**, 1900435.
- 31 J. Choi, S. Park, J. Lee, K. Hong, D.-H. Kim, C. W. Moon, G. Do Park, J. Suh, J. Hwang, S. Y. Kim, H. S. Jung, N.-G. Park, S. Han, K. T. Nam and H. W. Jang, *Adv. Mater.*, 2016, **28**, 6562–6567.
- 32 B. Hwang, C. Gu, D. Lee and J.-S. Lee, *Sci. Rep.*, 2017, **7**, 43794.
- 33 J. S. Han, Q. Van Le, J. Choi, K. Hong, C. W. Moon, T. L. Kim, H. Kim, S. Y. Kim and H. W. Jang, *Adv. Funct. Mater.*, 2018, **28**, 1705783.
- 34 F. Pan, S. Gao, C. Chen, C. Song and F. Zeng, *Mater. Sci. Eng. R Reports*, 2014, **83**, 1–59.
- 35 H. Kim, J. S. Han, S. G. Kim, S. Y. Kim and H. W. Jang, *J. Mater. Chem. C*, 2019, **7**, 5226–5234.
- 36 J.-C. Wang, Y.-R. Ye, C.-S. Lai, C.-T. Lin, H.-C. Lu, C.-I. Wu and P.-S. Wang, *Appl. Surf. Sci.*, 2013, **276**, 497–501.
- 37 S. R. Nandakumar, M. Minvielle, S. Nagar, C. Dubourdieu and B. Rajendran, *Nano Lett.*, 2016, **16**, 1602–1608.

- 38 Q. Liu, S. Long, H. Lv, W. Wang, J. Niu, Z. Huo, J. Chen and M. Liu, *ACS Nano*, 2010, **4**, 6162–6168.
- 39 T. Ninomiya, Z. Wei, S. Muraoka, R. Yasuhara, K. Katayama and T. Takagi, *IEEE Trans. Electron Devices*, 2013, **60**, 1384–1389.
- 40 X. Yang, Y. Divayana, D. Zhao, K. Swee Leck, F. Lu, S. Tiam Tan, A. Putu Abiyasa, Y. Zhao, H. Volkan Demir and X. Wei Sun, *Appl. Phys. Lett.*, 2012, **101**, 233110.
- 41 A. Perumal, S. Shendre, M. Li, Y. K. E. Tay, V. K. Sharma, S. Chen, Z. Wei, Q. Liu, Y. Gao, P. J. S. Buenconsejo, S. T. Tan, C. L. Gan, Q. Xiong, T. C. Sum and H. V. Demir, *Sci. Rep.*, 2016, **6**, 36733.
- 42 C. Wu, Y. Zou, T. Wu, M. Ban, V. Pecunia, Y. Han, Q. Liu, T. Song, S. Duhm and B. Sun, *Adv. Funct. Mater.*, 2017, **27**, 1700338.
- 43 H. Cho, S.-H. Jeong, M.-H. Park, Y.-H. Kim, C. Wolf, C.-L. Lee, J. H. Heo, A. Sadhanala, N. Myoung, S. Yoo, S. H. Im, R. H. Friend and T.-W. Lee, *Science (80-.)*, 2015, **350**, 1222–1225.
- 44 M.-H. Park, S.-H. Jeong, H.-K. Seo, C. Wolf, Y.-H. Kim, H. Kim, J. Byun, J. S. Kim, H. Cho and T.-W. Lee, *Nano Energy*, 2017, **42**, 157–165.
- 45 J. Yu, N. Wang, Y. Zang and Y. Jiang, *Sol. Energy Mater. Sol. Cells*, 2011, **95**, 664–668.

- 46 R. Waser, R. Dittmann, G. Staikov and K. Szot, *Adv. Mater.*, 2009, **21**, 2632–2663.
- 47 A. Sawa, *Mater. Today*, 2008, **11**, 28–36.
- 48 J. S. Han, Q. Van Le, J. Choi, H. Kim, S. G. Kim, K. Hong, C. W. Moon, T. L. Kim, S. Y. Kim and H. W. Jang, *ACS Appl. Mater. Interfaces*, 2019, **11**, 8155–8163.
- 49 T. Tsuruoka, K. Terabe, T. Hasegawa and M. Aono, *Nanotechnology*, 2010, **21**, 425205.
- 50 S. G. Kim, Q. Van Le, J. S. Han, H. Kim, M. Choi, S. A. Lee, T. L. Kim, S. B. Kim, S. Y. Kim and H. W. Jang, *Adv. Funct. Mater.*, 2019, **29**, 1906686.
- 51 C.-F. Chang, J.-Y. Chen, G.-M. Huang, T.-Y. Lin, K.-L. Tai, C.-Y. Huang, P.-H. Yeh and W.-W. Wu, *Nano Energy*, 2018, **53**, 871–879.
- 52 X. Lian, X. Shen, M. Zhang, J. Xu, F. Gao, X. Wan, E. Hu, Y. Guo, J. Zhao and Y. Tong, *Appl. Phys. Lett.*, 2019, **115**, 063501.
- 53 H. Wang and X. Yan, *Phys. status solidi – Rapid Res. Lett.*, 2019, **13**, 1900073.
- 54 S. Ding, Z. Wu, X. Qu, H. Tang, K. Wang, B. Xu and X. W. Sun, *Appl. Phys. Lett.*, 2020, **117**, 093501.

- 55 E. Ambrosi, A. Bricalli, M. Laudato and D. Ielmini, *Faraday Discuss.*, 2019, **213**, 87–98.
- 56 S. Zhang, S. Long, W. Guan, Q. Liu, Q. Wang and M. Liu, *J. Phys. D. Appl. Phys.*, 2009, **42**, 055112.
- 57 T. H. Park, S. J. Song, H. J. Kim, S. G. Kim, S. Chung, B. Y. Kim, K. J. Lee, K. M. Kim, B. J. Choi and C. S. Hwang, *Phys. status solidi - Rapid Res. Lett.*, 2015, **9**, 362–365.
- 58 S. J. Song, J. Y. Seok, J. H. Yoon, K. M. Kim, G. H. Kim, M. H. Lee and C. S. Hwang, *Sci. Rep.*, 2013, **3**, 3443.
- 59 S. G. Kim, J. S. Han, H. Kim, S. Y. Kim and H. W. Jang, *Adv. Mater. Technol.*, 2018, **3**, 1800457.
- 60 Q. Hu, T. S. Kang, H. Abbas, T. S. Lee, N. J. Lee, M. R. Park, T.-S. Yoon and C. J. Kang, *Microelectron. Eng.*, 2018, **189**, 28–32.
- 61 A. M. Rana, T. Akbar, M. Ismail, E. Ahmad, F. Hussain, I. Talib, M. Imran, K. Mehmood, K. Iqbal and M. Y. Nadeem, *Sci. Rep.*, 2017, **7**, 39539.
- 62 S. Lee, H. Kim, D. H. Kim, W. Bin Kim, J. M. Lee, J. Choi, H. Shin, G. S. Han, H. W. Jang and H. S. Jung, *ACS Appl. Mater. Interfaces*, 2020, **12**, 17039–17045.
- 63 E. Lim and R. Ismail, *Electronics*, 2015, **4**, 586–613.

- 64 L.-M. Lin, W.-L. Yang, Y.-H. Lin, Y.-P. Hsiao, F.-T. Chin and M.-F. Kao, *Phys. status solidi*, 2017, **214**, 1600595.
- 65 H. Kim, M.-J. Choi, J. M. Suh, J. S. Han, S. G. Kim, Q. Van Le, S. Y. Kim and H. W. Jang, *NPG Asia Mater.*, 2020, **12**, 21.
- 66 Y.-T. Chen, T.-C. Chang, H.-K. Peng, H.-C. Tseng, J.-J. Huang, J.-B. Yang, A.-K. Chu, T.-F. Young and S. M. Sze, *Appl. Phys. Lett.*, 2013, **102**, 252902.
- 67 T. Tsuruoka, K. Terabe, T. Hasegawa and M. Aono, *Nanotechnology*, 2011, **22**, 254013.

Chapter 6

<h3>Summary</h3>

The thesis covers the characterization of halide perovskite materials and the operating mechanism of halide perovskite-based resistive switching memories in detail. Moreover, 3D, quasi-2D, and 2D halide perovskites based resistive switching memories with various device structures are studied to enhance resistive switching performance, such as high ON/OFF ratios, long-endurance, and long retention time.

Through the first chapter, a background of the halide perovskites is introduced.

The halide perovskite materials have attracted technological and scientific interest due to their excellent optical and electronic properties with the advantages of low-cost fabrication and solution processability. The halide perovskite has the general formula ABX_3 . A and B are cations in this structure, where A is larger than B, and X represents the halide anion. The ABX_3 perovskite shows a 3D structure corresponding to a corner-sharing octahedral network.

With this unit formula of ABX_3 , halide perovskites composed of trihalides have been used extensively for photovoltaics as rapid active materials, owing to their useful electrical properties, such as the superior charge carrier mobility, extraordinarily long diffusion length of electrons, wide range of absorption, excellent charge carrier mobility, and high absorption coefficient. The exceptional electrical properties render halide perovskite materials competitive for next-generation devices, including solar cells, light-emitting diodes (LEDs), resistive switching memories, X-ray detectors, lithium-ion batteries, and more.

Through the second chapter, the operating mechanism within ReRAM devices are explained. And halide perovskites based ReRAM devices are introduced.

The memory elements consist of upper and lower electrodes and an insulating switching layer between the two electrodes. Following the electroforming process, when the opposite threshold voltage is applied, the low resistance state is switched to the high-resistance state at the particular voltage (RESET process). Then, the "SET process," which refers to the switching from an HRS to an LRS, occurs at opposite bias.

The switching mechanism can be classified as a filamentary-type and interface-type depending on the conducting path. The difference between filamentary and interface resistive switching depends on the area. In filamentary switching, the current conduction is narrowly confined to a narrow part of the device area. In contrast, in interface switching, the resistance change occurs by field-induced modification over the entire electrode area.

In this chapter, we introduce the advanced studies on ReRAM devices based on classified halide perovskite materials such as organic-inorganic hybrid, all inorganic, layered structure, and lead-free and new composition.

Through the third chapter, resistive switching memory devices based on $(\text{PEA})_2\text{Cs}_3\text{Pb}_4\text{I}_{13}$ halide perovskites are introduced for a high ON/OFF ratio and long-term stability.

Three-dimensional (3D) halide perovskites have been the most investigated materials for resistive switching memory devices. However, 3D-based memory devices display ON/OFF ratios comparable to those of oxide or chalcogenide ReRAM devices. In addition, perovskite materials are susceptible to exposure to air. In this chapter, a large ionic radius cation (PEA) was introduced into CsPbI₃ to form a quasi-2D halide perovskite, (PEA)₂Cs₃Pb₄I₁₃, to achieve a high ON/OFF ratio in ReRAM devices. Uniform surface morphology was achieved by incorporating the PEA cation and (PEA)₂Cs₃Pb₄I₁₃ effectively improved the resistive switching of the device. Astonishingly, the ON/OFF ratio of the (PEA)₂Cs₃Pb₄I₁₃-based memory devices (10⁹) is three orders of magnitude higher than that of the CsPbI₃ device. Owing to the wide bandgap of (PEA)₂Cs₃Pb₄I₁₃, a high Schottky barrier was formed, and the activation energy increased, thereby leading to a reduction in the HRS current.

A stability test verified the superior resistance of the device under ambient atmosphere at room temperature, which is another favorable property of quasi-2D perovskites. This device retained a high ON/OFF current ratio for two weeks under ambient conditions, whereas the CsPbI₃ device degraded rapidly and showed unreliable memory properties after five days. These results strongly suggest that quasi-2D halide perovskites have potential in resistive switching memory based on their desirable ON/OFF ratio and long-term stability.

Through the fourth chapter, the 2D (PEA₂PbI₄)/3D (MAPbI₃) perovskite heterojunction films for resistive switching devices is introduced.

The 2D/3D perovskite device exhibits an endurance of ~ 2700 cycles, which is about nine times longer than that of the pristine 3D perovskite device. The calculated thermally-assisted ion-hopping activation energy and the results of the time-of-flight secondary ion mass spectroscopy demonstrated that the 2D perovskite layer could efficiently prevent the Ag ion migration into the 3D perovskite film. The comparatively high hopping activation energy of the 2D/3D perovskite device (0.150 vs 0.135 eV of 3D perovskite) checks the Ag ion migration into the 3D perovskite film, resulting in the formation of a narrow Ag conductive filament.

In addition, the 2D films exhibited a thermal conductivity of $1.18 \text{ W m}^{-1}\text{K}^{-1}$, which is about four times higher than that of the 3D films ($0.28 \text{ W m}^{-1}\text{K}^{-1}$); this could control the rupture of the Ag conductive filament during the reset process. Consequently, the 2D/3D perovskite was designed to significantly enhance the endurance and stability by controlling the Ag ion migration and filament rupture. These results suggested that the 2D/3D perovskite film can improve the endurance of the halide perovskite-based resistive switching memory devices.

Through the fifth chapter, MAPbBr₃ with an electron transfer material (TPBI), is introduced to achieve long-endurance cycles and retention time in ReRAM devices.

Resistive switching properties in the ReRAM device with the Ag/TPBI/MAPbBr₃/Pt are induced by Ag filaments' formation and rupture in the MAPbBr₃ layer. The MAPbBr₃:TPBI device showed longer endurance cycles of 300, which is four orders of magnitude higher than that of the MAPbBr₃:CF memory device. Because TPBI makes electrons effectively inject into the switching layer, the oxidation of Ag conducting filaments can occur more efficiently, which is beneficial to the rupture of Ag filaments.

In addition, the retention time for the ON and OFF states was evaluated to test the electrical reliability of the MAPbBr₃ memory device. Hence, this work has its value in terms of an alternate strategy for upgrading the switching property of halide perovskite memory devices.

The thesis suggested halide perovskites based non-volatile memory devices for practical applications as a promising material strategy. Although formal research on halide-perovskite-based ReRAM devices has only just started, it will be a highly influential device with tremendous advances in the future market and serve as a stepping stone for developing a resistive switching memory field. It is believed the thesis will encourage researchers to investigate halide-perovskite-based ReRAM devices with useful insights, overcome its challenges, and give a direction to offer promising opportunities.

Abstract (in Korean)

2D 그리고 quasi-2D 할라이드 페로브스카이트를 기반으로 한 저항

변화 메모리 소자

정보화 시대의 발전에 따라, 많은 양의 데이터를 처리하기 위한 고성능 저장 매체의 필요성이 제기되어 왔으며, ReRAM은 기존 메모리 장치의 차세대 대안으로 각광 받고 있다. 기존 ReRAM 소자에는 금속 산화물이 주로 이용되어 왔으며, 이에 대한 연구가 활발히 진행되어 왔지만, 이 물질을 절연층으로 한 저항변화 메모리 소자는 기계적 유연성이 낮고, 고온 공정과 진공 장비 사용으로 인해 제작비용이 높으며, 전기적 특성 제어가 어렵다는 한계를 보여왔다. 따라서, 이러한 단점을 극복하기 위한 새로운 절연층 탐색이 필요하며, 최근 할라이드 페로브스카이트 소재를 적용한 저항변화 메모리 소자에 관한 연구가 활발히 진행되고 있다. 할라이드 페로브스카이트 기반의 ReRAM 소자는 높은 온오프 저항비, 낮은 구동 전압, 그리고 우수한 기계적 특성을 보이며 차세대 메모리 소자로서 주목 받고 있다.

본 학위논문에서는 할라이드 페로브스카이트 소재의 전기적 특성과 ReRAM 소자의 구동 메커니즘에 대해 서술되어 있다. 또한, 온오프 저항비, 엔듀런스 그리고 리텐션 등과 같은 저항변화 스위칭 성능 향상 시키기 위한 세 가지 연구 주제를 소개한다.

첫 번째 연구 주제에서는 할라이드 페로브스카이트 소재에 대한 전반적인 내용을 소개한다.

일반적으로 할라이드 페로브스카이트 ABX_3 구조를 가지고 있으며, A 위치에는 메틸암모늄이나 세슘과 같은 양이온, B 위치에는 납과 같은 금속 양이온, 그리고 X 할로겐화 음이온이 위치한다.

이 소재는 밴드갭 조절이 가능하고, 다수 운반자 제어가 용이하며, 높은 이온 이동성과 같은 고유한 특성을 가지고 있다. 따라서, 이 소재는 태양전지, LED, 그리고 X-선 검출기 등과 같은 다양한 영역에서 광범위하게 적용되고 있다.

이 할라이드 페로브스카이트 박막은 스펀코팅과 같은 용액공정 또는 진공 공정으로 제작이 가능하며, 본 학위논문에서 실린 연구에서는 소자의 구현에 있어서 모두 스펀코팅 방법을 도입하였다.

두 번째 챕터에서는 저항변화 메모리 소자의 구동 메커니즘과 할라이드 페로브스카이트를 이용한 메모리 소자의 선행 연구에 대해 소개하고 있다. 스위칭 메커니즘은 필라멘트의 전도성 경로에 따라 filamentary 타입과 interface 타입으로 구분하며 각각의 저항 변화 특징에 대해 설명하였다. 또한, 할라이드 페로브스카이트의 조성에 따라 1) 유기-무기 하이브리드, 2) 무기-무기, 3) 층상 구조, 4) 무연 및 새로운 구성의 할라이드 페로브스카이트로 분류하며, 이를 기반으로 한 선행 연구들에 대해서 소개하였다.

세 번째 챕터에서는 quasi-2D 할라이드 페로브스카이트인 $(\text{PEA})_2\text{Cs}_3\text{Pb}_4\text{I}_{13}$ 를 박막의 저항변화 특성 연구를 소개한다. 기존의 3차원 구조를 갖는 CsPbI_3 소자는 낮은 온오프 저항비를 가지며 수분안정성이 낮다는 단점을 가지고 있다. 이를 극복하기 위해, 페닐에틸암모늄 양이온을 이용하여 quasi-2D 물질인 $(\text{PEA})_2\text{Cs}_3\text{Pb}_4\text{I}_{13}$ 을 합성하였으며, 이를 메모리 소자에 적용하였다.

CsPbI₃ 기반 소자는 10³의 온오프 저항비를 보인 것에 비해, (PEA)₂Cs₃Pb₄I₁₃ 기반 소자는 10⁹으로 온오프 저항비가 증가하였다. 이것은 밴드갭의 증가함에 따라 쇼트키베리어 하이트가 증가하고, 이로 인해 고저항상태의 커런트가 감소하여 온오프 저항비가 증가한 것으로 보인다. 또한, 소수성을 띄는 페닐에틸암모늄으로 인해, 수분으로부터 저항변화층이 보호되어 수분 안정성이 증가함을 확인하였다.

네번째 챕터에서는 2D 페로브스카이트인 PEA₂PbI₄와 3D 페로브스카이트인 MAPbI₃를 서로 적층하여 스위칭 물질로 사용하고 이를 저항변화 메모리 소자에 적용한 연구내용을 담고 있다. MAPbI₃(3D)를 기반으로 한 소자는 300 회 정도의 엔듀런스 사이클을 보인 것에 비해, PEA₂PbI₄와 MAPbI₃(2D/3D)를 적층한 소자 2700 회의 엔듀런스 사이클이 기록되며 연속반복구동 수명이 증가함을 확인하였다. 이것은 Ion hopping activation energy가 큰 PEA₂PbI₄로 인해 Ag 이온이 MAPbI₃층으로 이동하는 것을

효율적으로 방지하고, 또한 thermal conductivity 가 다른 PEA_2PbI_4 와 MAPbI_3 에 의해 필라멘트의 럽쳐가 국소적으로 일어남에 기인한다.

다섯번째 챕터에서는 전자전달물질로 사용된 TPBI 를 MAPbBr_3 층 위에 도입하여 메모리 소자를 구현한 연구내용에 대해 소개한다. TPBI 는 전자의 이동을 용이하게 하여 RESET 과정에서 필라멘트의 럽쳐를 효과적으로 발생하게 한다. 따라서 TPBI 가 적용된 MAPbBr_3 기반 소자는 TPBI 가 적용되지 않은 소자에 비해, 3 배 이상의 엔듀런스 사이클이 증가함을 확인하였다.

본 박사학위 논문에서는 할라이드 페로브스카이트 소재와 저항변화 메모리 소자에 대해 소개하고, 이 소자의 스위칭 성능을 향상 시키기 위한 세가지 연구주제에 대해 설명하며 소자의 전기적 특성 및 메커니즘을 분석하였다. 이 연구 결과들은 향후 할라이드 페로브스카이트 기반의 ReRAM이 차세대 메모리 소자로 크게 발전하여, 상용화에 기여할 것으로 기대되는 바이다.

주요어:

저항변화 메모리 소자, 저항변화 스위칭 메커니즘, 용액공정, 3D 구조의
할라이드 페로브스카이트, quasi-2D 구조의 할라이드 페로브스카이트,
3D/2D 이종 접합 할라이드페로브스카이트, TPBI

학번: 2017-36719

김 효 정